PONTIFICIA UNIVERSIDAD CATÓLICA DEL PERÚ

ESCUELA DE POSGRADO

PROPAGATING REACTION FRONTS IN MOVING FLUIDS

Tesis para optar el grado de Doctor en Física que presenta

PABLO MARTIN VILELA PROAÑO

Asesor

DESIDERIO A. VASQUEZ RODRIGUEZ

Jurado

MARIA ELENA LOPEZ HERRERA

DESIDERIO A. VASQUEZ RODRIGUEZ

HERNAN A. CASTILLO EGOAVIL

JOSEPH W. WILDER

JOEL JONES PEREZ

Lima, 2015

PROPAGATING REACTION FRONTS IN MOVING FLUIDS

Pablo Martín Vilela Proaño

Presented Towards a Doctor's Degree in Physics

2015

Abstract

The coupling between molecular diffusion and chemical reaction give rise to chemical fronts. For example, when we start an autocatalytic reaction in a liquid, we observe a moving interface separating reactants and products as the reaction proceeds. This interface is called chemical front or propagating front. Our goal is to study reaction fronts described by the Kuramoto-Sivashinsky equation under different types of fluid motion: an external Poiseuille flow which is contrasted with an external Couette flow, and convective flow due to the Rayleigh-Taylor instability. In the first case, the fronts propagate with or against a steady two-dimensional flow between two parallel plates, known as Poiseuille flow. In narrow slabs, we found steady front profiles that can be flat, axisymmetric, or nonaxisymmetric, depending on the slab width and the average flow speed. We find that stable steady axisymmetric fronts propagating against an axisymmetric Poiseuille flow become nonaxisymmetric when the average speed of this adverse Poiseuille flow is increased. In the case of Couette flow, two parallel plates moving in opposite directions generate a linear fluid velocity field. We find that the shape of the steady fronts and their stability depend on the slab width and on the relative velocity between the plates. These parameters have the potential to modify unstable fronts into stable fronts. When the denser fluid is on top of less dense fluid, the front instabilities are caused by the density difference across the front in a gravitational field. These instabilities are known as Rayleigh-Taylor instabilities. In this last case, the front describes the thin interface between two fluids of different densities inside a two-dimensional vertical slab, while convection caused by buoyancy forces across an interface determines the flow due to the Rayleigh-Taylor instability. We obtain different spatial fronts profiles, depending on the slab width, the density gradient, and fluid viscosity. First we obtained fronts regardless of the stability, and then we carry out a linear stability analysis to determine the stability of the

fronts in each case. We show regions of bistability where stable nonaxisymmetric and axisymmetric fronts can coexist for each type of flow.

Keywords: Reaction fronts; Kuramoto-Sivashinsky equation; Rayleigh-Taylor instabilities; Couette flow; Poiseuille flow

PROPAGATING REACTION FRONTS IN MOVING FLUIDS

Pablo Martín Vilela Proaño

Propuesto para el Grado de Doctor en Física

2015

Resumen

Los frentes químicos se obtienen experimentalmente como resultado del acoplamiento entre difusión molecular y reacción química. Por ejemplo, cuando se inicia una reacción autocatalítica en un líquido, se observa una interfaz que separa reactantes y productos mientras se produce la reacción. A esta interfaz se le denomina frente químico. Nuestro objetivo es estudiar frentes químicos modelados mediante la ecuación de Kuramoto-Sivashinsky sujetos a diferentes tipos de movimiento de fluido: flujo externo de Poiseuille, el cual es contrastado con el flujo externo de Couette, y flujo convectivo debido a la inestabilidad de Rayleigh-Taylor. En el primer caso, los frentes se propagan a favor o en contra de un flujo estacionario bidimensional entre dos placas paralelas que se conoce como flujo de Poiseuille. Para pequeñas distancias entre las placas, encontramos frentes estacionarios que pueden ser planos, simétricos o asimétricos, dependiendo de la separación de las placas y de la velocidad promedio del fluido externo. Mostraremos que los frentes simétricos estables que se propagan en sentido opuesto al flujo simétrico externo se vuelven asimétricos al incrementar la rapidez del flujo externo. En el caso del flujo de Couette, el flujo es producido por el movimiento de dos placas paralelas en sentidos opuestos. Encontramos que la estabilidad y la forma de los frentes estacionarios dependen de la velocidad relativa entre las placas y de su separación. Estos parámetros pueden convertir frentes inestables en estables. Las inestabilidades en el frente producidas cuando el fluido más denso se encuentra encima del fluido menos denso, se conocen como inestabilidades de Rayleigh-Taylor y son causadas por la diferencia de densidades a través del frente bajo la acción de la gravedad. En este último caso, el frente describe la interfaz delgada entre dos fluidos de diferente densidad dentro de dos placas paralelas verticales, mientras que la convección causada por las fuerzas de flotación a través de una interfaz determina el flujo debido a la inestabilidad de

Rayleigh-Taylor. Primero obtendremos los frentes y luego realizaremos un análisis de estabilidad lineal para determinar la estabilidad de los frentes en cada uno de los casos. Mostraremos regiones de bi-estabilidad donde frentes estables simétricos y asimétricos pueden coexistir para cada tipo de flujo.

Palabras claves: Frentes de reacción; ecuación de Kuramoto-Sivashinsky; inestabilidad de Rayleigh-Taylor; flujo de Couette; flujo de Poiseuille

To my wife Natalia and my son Juan Pablo

Acknowledgments

I would like to thank my teachers and classmates for their valuable questions and comments given in the seminar courses over the past three years. Their suggestions made a substantial contribution to this work. I thank all of you.

I would like to give special thanks to my advisor Ph.D. Desiderio Vasquez, who taught me how to conduct scientific research on non-linear dynamics and write a scientific paper. He is an excellent mentor, teacher and person. Thank you very much.

I appreciate the unconditional support given by my parents, siblings, my nephew Alberto and close relatives.

This work was supported by a grant from the Dirección de Gestión de la Investigación (DGI 2013-0028) of the Pontificia Universidad Católica del Perú (PUCP) and a Huiracocha grant from the Graduate School of the PUCP.

Publications and presentations related to this thesis

Journal articles

P. M. Vilela and Desiderio A. Vasquez, “Stability of fronts in the Kuramoto-Sivashinsky equation advected by a Poiseuille flow”, Phys. Rev. E **86**, 066102 (2012)

P. M. Vilela and Desiderio A. Vasquez, “Rayleigh-Taylor instability of steady fronts described by the Kuramoto-Sivashinsky equation”, Chaos: An Interdisciplinary Journal of Nonlinear Science **24**, 023135 (2014)

P. M. Vilela and Desiderio A. Vasquez, “Stability of Kuramoto-Sivashinsky fronts in moving fluid”, Eur. Phys. J. Special Topics **223**, 3001 (2014)

Presentations

“Estabilidad de frentes químicos con flujo de Poiseuille”.
XX Simposio Peruano de Física. I Seminario Internacional de Física.
IV Congreso Peruano de Física Médica.
Universidad Nacional Jorge Basadre Grohmann.
Del 26 de setiembre al 01 de octubre de 2011, Tacna – Perú.

“Propagación de frentes Químicos con flujo de Poiseuille”.
Coloquio de Física PUCP.
Pontificia Universidad Católica del Perú.
El 12 abril 2012, Lima – Perú.

“Stability of fronts in the Kuramoto-Sivashinsky equation with moving flow”.
Short Talk in: International School in advanced Computational and Experimental Techniques in Nonlinear Dynamics.
May 6 - 10, 2013. Cusco, Perú.

“Stability of fronts in the Kuramoto-Sivashinsky equation with moving flow”.
Poster Presentation in: International Workshop in advanced Computational and Experimental Techniques in Nonlinear Dynamics.
May 13 - 17, 2013. Cusco, Perú.

Contents

List of figures

List of tables

Chapter 1

Introduction

A variety of reaction-diffusion systems exhibits propagating waves and spatial patterns [1,2]. Among them, we have the Belousov-Zhabotinsky (BZ) reaction [3,4], the chlorite-iodide-malonic acid (CIMA) reaction [5] and the iodate-arsenous acid (IAA) reaction [6]. The BZ reaction is an oscillatory reaction that exhibits travelling (concentration) waves [7], spiral waves, target patterns, and other spatio-temporal patterns [8], including stationary Turing structures [9] and chemical chaos [10]. Castets, *et al.* working experimentally with the Chlorite-iodide-malonic acid-starch reaction in a gel reactor found the first evidence of the existence of the symmetry breaking, reaction-diffusion structures predicted by Turing [11,12]. In addition, the reaction between iodide ion and chlorite ion exhibits bistability, oscillatory behavior and propagating waves [13,14]. The IAA reaction also exhibits bistability and chemical waves, but in contrast to the other reactions, the IAA reaction can be accurately described by a one variable (scalar) reaction-diffusion equation with cubic reaction kinetics [6]. The IAA reaction, like many other autocatalytic or oscillatory reactions, generates propagating reaction-diffusion fronts [15], which are the simplest type of chemical waves. The front is an interface that divides the system into two different states (or phases), which can be also found in other contexts such as, forest fire [16], crystal growth, landslide, epidemics [17], cell populations, corrosion [18], and so on. In particular, we are interested in propagating fronts, which result from the coupling of autocatalytic reaction with molecular diffusion [19]. These fronts typically move with constant velocity and constant spatial profile, separating reactants and products.

A simple model for autocatalytic reactions with a quadratic autocatalysis can be written as $A+B\rightarrow 2B$, where A is the reactant and B is the autocatalyst (a product speeding up its own formation because it is also a reactant). The rate law in this case is quadratic because it is proportional to the product of the concentrations of the two reactants, which can be written in terms of one-variable. In this case, the autocatalytic reaction-diffusion front is a constant

concentration profile separating two reacting species with different concentrations. The reactant A is ahead of the front, while the product B is behind of the front. Molecular diffusion plays an important role allowing the autocatalyst to spread, leading to propagating reaction fronts [1,14]. Fisher [20] worked a one-dimensional reaction-diffusion equation with a quadratic rate law to study the propagation of a dominant gene. At the same time, and independently, Kolmogorov *et al.* [21] worked with a more general nonlinear rate law. Hence, the equation they obtained independently is referred to as the Fisher-Kolmogorov equation (or sometimes FKPP equation). The solution to this reaction-diffusion equation with its quadratic nonlinearity corresponds to a propagating front [21]. However, there are other chemical systems (such as the IAA reaction) which can be described by a one variable reaction-diffusion equation where the reaction term is a cubic polynomial. In contrast to the quadratic reaction-diffusion equation, the cubic reaction-diffusion equation exhibits an analytical solution for velocity and concentration profile [1,6]. In addition, it is also useful to consider mixed-order autocatalysis where the rate law is a linear combination of quadratic and cubic rate laws to get more general features of propagating reaction-diffusion fronts [22]. Experiments with the IAA reaction (in gels to avoid fluid flow), having different diffusivities for the reactant and the autocatalyst, show instabilities that can be described with quadratic and cubic mixed-order models [23,24].

Propagating reaction fronts can be considered as a thin interface separating products from reactants. The dynamics of the interface can be described with an eikonal relation [25], or a front equation derived independently by Y. Kuramoto [26] and G. Sivashinsky [27]. The eikonal equation shows the dependency of the normal velocity of the reaction front on the curvature of the front. This eikonal equation has been confirmed experimentally working with spiral waves in the BZ reaction [28,8]. On the other hand, reaction fronts presenting instabilities caused by substances with different diffusivities can be modeled using the Kuramoto-Sivashinsky (KS) equation [23,29]. This KS equation was derived by Y. Kuramoto to study chemical wave propagation in reaction-diffusion systems and, independently, by G. Sivashinsky to model the propagation of combustion fronts (see appendix A.1). The KS equation also

appears in other contexts, including chemical turbulence [30], rapid directional solidification [31], phase turbulence [32], and falling-film flows [33,34]. Similar to combustion fronts [27], instabilities in propagating fronts of the IAA reaction (in gels to suppress convection) appear when the ratio of the reactant diffusivity to the autocatalyst diffusivity exceeds a critical value [24]. The propagation of these fronts can be approximated with the KS equation, which exhibits suitable conditions to describe flat front instabilities. The KS equation can also show transitions between steady flat fronts, curved fronts, and complex pattern formation [35].

The presence of fluid flow impacts on the evolution of reaction-diffusion systems since the fluid motion enhances transport and mixing [36,37]. For example, the presence of wind on a forest fire contributes to spread the fire, or ocean currents help plankton blooms by carrying the nutrients to the ocean surface. In the case of autocatalytic reaction fronts, density gradients generate convective fluid motion as the front propagates upward inside vertical tubes. For example, in ascending IAA reaction fronts, the change in density takes place because the reacted fluid is lighter than the unreacted fluid [38]. Hence the front separates fluids of different densities, which may result in Rayleigh-Taylor (RT) instabilities as a less dense fluid is placed under a denser fluid [39]. As the RT instability develops, the denser fluid goes down while the less dense fluid goes up. Consequently, the motion of the fluids decreases the potential energy of the fluid system. An initial small perturbation which takes the interface between the fluids out of equilibrium will grow fast, decreasing further the potential energy of the system. However, the problem of ascending IAA reaction fronts in vertical tubes differs from the RT problem because the front is not stabilized by surface tension. Since autocatalytic reaction fronts in the IAA reaction are thin, the reaction-diffusion model can be replaced with an eikonal relation between the normal front velocity and the front curvature [40]. This eikonal relation tends to stabilize the ascending front by flattening the front, while the buoyant effect tends to destabilize the flat front forming convective rolls [41]. Propagating fronts under the effects of convection due to a RT type of instability has been studied in several systems such as IAA acid mixtures [24,42,43], BZ reaction inside a vertical tube [44], and the iodate-sulfate system [45]. Experiments by

Masere *et al.* [46] on IAA mixture in vertical tubes showed that convective fluid motion due to density differences across the front can change the shape and speed of ascending fronts by increasing the tube diameter. On the other hand, experiments show no convection in descending fronts where the lighter fluid is above the heavier fluid. Moreover, Masere *et al.* found experimentally that no convection appears in ascending flat fronts for diameters less than a critical value. For diameters slightly above this value, the flat front becomes nonaxisymmetric with fluid rising on one side of the tube, and falling on the opposite side, as predicted by Vasquez *et al.* [42], while for higher values the flat front becomes axisymmetric.

Another type of interaction between reaction fronts and fluids takes place inside a Hele-Shaw cell (which consists of two parallel plates separated by a small gap), with the fluid flow generated by an external pressure gradient. Edwards *et al.* [47,48] studied the effects of advection (the movement of fluid particles from one place to another) on reaction fronts using a steady flow between two parallel plates. This steady two-dimensional flow (known as Poiseuille flow) exhibits a parabolic velocity profile. They found that Poiseuille flow between parallel plates changes the shape and the speed of stable fronts [48]. These results have been confirmed experimentally by Salin *et al.* [49] in experiments inside tubes and Hele-Shaw cells [50]. Thus the coupling between reaction-diffusion fronts with fluid motion affects the structure and velocity of the fronts.

Fluid flow affects stable flat fronts, as well as fronts showing complex spatio-temporal structures. The latter requires the use of reaction-diffusion equations with species of different diffusivities, or the use of the KS equation. Indeed, fronts described by the KS equation coupled to convective fluid flow can exhibit complex spatiotemporal behavior, such as steady cellular structures, oscillatory, or chaotic fronts [51,52,53]. The aim of the present work is to study the effects of advection in patterns arising from flat front instabilities described by the KS equation. We look for steady fronts that propagate at a constant speed either in the same direction as the flow or in the opposite direction. The stability of the fronts is analyzed using a linear stability analysis on the advected fronts. In addition, we look for steady structures appearing from the combined effects of

the dynamics of the KS equation and the RT instability. We then determine their stability using a linear stability analysis. We consider both cases, one where the denser fluid is placed on top of a less dense fluid and the opposite case. We show that depending on the size of our domain, complex fronts can appear such as steady curved fronts, oscillatory or chaotic fronts.

The study of chemical systems has contributed to the understanding of deterministic chaos [54,2]. An example of a chemical oscillator is the BZ reaction [4]. This reaction can exhibit a classic period-doubling sequence leading to chaotic behavior, where the oscillations are aperiodic (infinite period). This reaction can also display spatiotemporal patterns, in which the pattern is oscillatory in time and uniform in space, such as target patterns and spiral patterns [55]. These patterns can also arise in a combination of fluid flow with chemical reactions in reaction-diffusion-advection systems [56,57]. Among these patterns we find structures like curved fronts [42,46], fingering [58,51], and traveling patterns [56,59], which give rise due to the coupling between reaction-diffusion fronts with fluid motion [60]. In this work, we will present oscillatory and chaotic fronts as they are advected by fluid motion.

This thesis is organized as follows. In Chapter 2, we introduce the linear stability analysis for systems of ordinary differential equations. In Chapter 3, we introduce a steady laminar flow between infinite parallel plates. We derive the velocity profile of a Poiseuille flow and a Couette flow. We study viscous flows in a Hele-Shaw cell. We also analyze the Rayleigh-Taylor instability, including fluid viscosity and surface tension in the dispersion relation. In Chapter 4, we review the basic concepts related to chemical fronts, emphasizing the interaction between diffusion and reaction which leads to propagating fronts. We also include the eikonal approximation and the KS equation to describe the reaction fronts. In Chapter 5, we look for steady solutions described by the KS equation without fluid flow. We consider fronts propagating between two infinite parallel plates separated by a small distance, which corresponds to the domain width. This domain plays an important role in analyzing the fronts, since it determines the speed and symmetry of steady solutions of the KS equation. In Chapter 6, we analyze the effects of fluid flow on steady fronts described by the KS equation as they are advected by a Poiseuille flow. We also look for

oscillatory and chaotic fronts. In Chapter 7, we will study propagating fronts under an external Couette flow. This flow develops from the relative motion of two parallel plates separated by a constant distance resulting in a linear velocity profile. We compare our results with fronts developed under a Poiseuille flow. In Chapter 8, we consider fronts propagating between two infinite vertical plates separated by a small gap, containing two fluids of different densities. In this geometry the fluid flow can be approximated by Darcy's law in two dimensions. Darcy's law describes the rate at which a fluid flows through a porous medium. The domain is bounded by two vertical walls separated by a distance, which corresponds to the slab width. As the slab width is increased, the KS equation allows for the propagation of different fronts of steady shapes and symmetries. We also obtain oscillatory and chaotic fronts and look for conditions of stability for cellular structures, which corresponds to extended domains generated from solutions in smaller domains or cells. Finally, in Chapter 9, we review the most important ideas and conclude.

Chapter 2

Dynamical systems and stability

A dynamical system is a mathematical model to describe the evolution of a real system such as the growth of a bacteria population, radioactive decay, an electrical circuit, the time evolution of concentrations of reactants and products in a chemical reaction, the movement of a pendulum, etc. There are two kinds of dynamical systems: discrete time dynamical systems governed by difference equations (or discrete maps) and continuous time dynamical systems governed by differential equations. The former can be used to study population growth (or radioactive decay, pollution control, etc.) since changes in population occurs at discrete moments in time; while the latter can be used to study the evolution of concentrations of chemical reactions using differential equations (or the pendulum, the harmonic oscillator, etc.). It is worth mentioning that a continuous time system can be reduced to a discrete time map using the Poincaré surface of section method [61].

2.1 Stability

We are interested in study continuous dynamical systems whose time evolution is described by differential equations in terms of the state variables of the system. For example, in the case of a simple pendulum, the state variables are the angular position and velocity, since knowing these values at one time is enough to determine all their future values. Indeed, all the possible values of the state variables define a plane which is referred to as phase plane (or in general a phase space). Thus, a state of the system is represented by a point in phase space and the time evolution by an orbit or trajectory. Depending on the nature of the problem, we can have one differential equation or a set of differential equations. For example, a one-dimensional dynamical system could be of the form

$$\frac{du}{dt} = f(u,r), \tag{2.1}$$

where f is usually a nonlinear function and r is a parameter. In this case, the phase space is a line (one-dimensional) and for a fixed value of the parameter r, a state of the system is represented by a point and the time evolution by a one-dimensional trajectory. Let u_s be a stationary solution of Eq. (2.1) when the parameter takes the value $r = r_0$, therefore it satisfies $f(u_s, r_0) = 0$. The state u_s will be stable (in the sense of Lyapunov) if any solution of the dynamical system that starts near u_s remains close to it for all time. In contrast, u_s will be asymptotically stable if u_s is stable and all solutions that start near u_s tends to go back to u_s after a long time. In this case the fixed point in the phase space is an attractor. To get a qualitative understanding of these definitions, imagine a marble sitting at rest at the bottom of a bowl. This lower position corresponds to the equilibrium position of the marble. If the marble is pushed aside slightly, the marble will oscillate around its equilibrium position. If there are no dissipative forces, the marble will continue oscillating around this point all time. We observe that the marble remains in the neighborhood of the equilibrium position. However, if there are dissipative forces, the marble will get back to the equilibrium position eventually. The first case corresponds to a stable equilibrium, while the latter corresponds to an asymptotically stable equilibrium. On the other hand, to determine the linear stability of u_s we introduce a small perturbation to the stationary-state solution u_s, so that the state of the system is given by

$$u(t) = u_s + \zeta(t). \tag{2.2}$$

We will explain in detail this method in the following section.

2.2 Linear stability

For the sake of simplicity we consider the following first order differential equation

$$\frac{dx}{dt} = f(x). \tag{2.3}$$

This one dimensional system is autonomous because f does not depend explicitly on the independent variable t. Let x_s be an equilibrium solution (or steady solution) of the system, hence $f(x_s)=0$. Now, we want to know whether the state of equilibrium of the steady solution is stable or unstable. We analyze the stability by introducing small perturbations to the stationary-state solution. We substitute in Eq. (2.3)

$$x(t) = x_s + \zeta(t), \tag{2.4}$$

where $\zeta(t)$ is a small perturbation of the steady state x_s. We obtain

$$\frac{d\zeta}{dt} = f(x_s + \zeta). \tag{2.5}$$

Using Taylor's expansion for the function f about x_s and keeping only the linear terms on ζ, we obtain

$$\frac{d\zeta}{dt} \approx f(x_s) + \zeta f'(x_s) = \zeta f'(x_s). \tag{2.6}$$

Notice that the approximation used in Eq. (2.6) requires that $f'(x_s) \neq 0$. Assuming we are in this case, Eq. (2.6) can be written as

$$\frac{d\zeta}{dt} = \lambda\zeta, \tag{2.7}$$

where λ is a constant, being $\lambda = f'(x_s)$. The solution of Eq. (2.7) is given by

$$\zeta(t) = \zeta_0 e^{\lambda t}, \tag{2.8}$$

where $\zeta_0 = \zeta(0)$ is the amplitude of the perturbation and it is a small value. From Eq. (2.8) we observe that the perturbation will grow exponentially if $\lambda > 0$. That is, if $f'(x_s) > 0$ the steady state is unstable. On the other hand, if $f'(x_s) < 0$ the steady state solution is stable. What happen if $f'(x_s) = 0$? In this case the linearization used in Eq. (2.6) is not appropriate. In other words, we have to execute a nonlinear analysis to determine the stability of this steady state solution [62].

The linear stability analysis executed above can be extended to systems of many variables. As an example, let's study the case of two first order differential equations. The autonomous system is given by

$$\begin{aligned} \frac{dx}{dt} &= f(x,y) \\ \frac{dy}{dt} &= g(x,y) \end{aligned} \tag{2.9}$$

Let (x_s, y_s) be a steady solution of Eq. (2.9). Hence $f(x_s, y_s) = g(x_s, y_s) = 0$. We analyze the stability by introducing small perturbations to each component of the stationary-state solution. We have

$$x(t) = x_s + \zeta(t) \tag{2.10}$$

and

$$y(t) = y_s + \xi(t), \tag{2.11}$$

where $\zeta(t)$ and $\xi(t)$ are small perturbations to the components of the steady state (x_s, y_s). With these substitutions in Eq. (2.9), we obtain

$$\begin{aligned} \frac{d\zeta}{dt} &= f(x_s + \zeta, y_s + \xi) \\ \frac{d\xi}{dt} &= g(x_s + \zeta, y_s + \xi) \end{aligned} \tag{2.12}$$

Using Taylor's expansion for the functions f and g about the steady state $\boldsymbol{x}_s = (x_s, y_s)$, and keeping only the linear terms on ζ and ξ; we obtain

$$\begin{aligned} \frac{d\zeta}{dt} &\approx f(x_s, y_s) + \zeta \left.\frac{\partial f}{\partial x}\right|_{x=x_s} + \xi \left.\frac{\partial f}{\partial y}\right|_{x=x_s} = \zeta \left.\frac{\partial f}{\partial x}\right|_{x=x_s} + \xi \left.\frac{\partial f}{\partial y}\right|_{x=x_s} \\ \frac{d\xi}{dt} &\approx g(x_s, y_s) + \zeta \left.\frac{\partial g}{\partial x}\right|_{x=x_s} + \xi \left.\frac{\partial g}{\partial y}\right|_{x=x_s} = \zeta \left.\frac{\partial g}{\partial x}\right|_{x=x_s} + \xi \left.\frac{\partial g}{\partial y}\right|_{x=x_s} \end{aligned} \tag{2.13}$$

Since the partial derivatives of Eq. (2.13) are evaluated at the steady state $\boldsymbol{x}_s = (x_s, y_s)$, they are numbers. Hence, the system in Eq. (2.13) can be written in the matrix form

$$\begin{pmatrix} \frac{d\zeta}{dt} \\ \frac{d\xi}{dt} \end{pmatrix} = \begin{pmatrix} \left.\frac{\partial f}{\partial x}\right|_{x=x_s} & \left.\frac{\partial f}{\partial y}\right|_{x=x_s} \\ \left.\frac{\partial g}{\partial x}\right|_{x=x_s} & \left.\frac{\partial g}{\partial y}\right|_{x=x_s} \end{pmatrix} \begin{pmatrix} \zeta \\ \xi \end{pmatrix} = \mathbf{J} \begin{pmatrix} \zeta \\ \xi \end{pmatrix}. \tag{2.14}$$

Where the 2×2 matrix $\mathbf{J}$ is referred to as the Jacobian matrix evaluated at the steady state (x_s, y_s). The general solution of Eq. (2.14) is given by

$$\begin{pmatrix} \zeta \\ \xi \end{pmatrix} = \mathbf{v}_1 e^{\lambda_1 t} + \mathbf{v}_2 e^{\lambda_2 t}. \tag{2.15}$$

Where the constant column vectors $\mathbf{v}_1$ and $\mathbf{v}_2$, and the constants λ_1, and λ_2 are determined from

$$\mathbf{J}\mathbf{v}_i = \lambda_i \mathbf{v}_i \quad (\text{for } i = 1,\ 2) \tag{2.16}$$

Equation (2.16) results from replacing Eq. (2.15) into Eq. (2.14). We are dealing with an eigenvalue problem, where λ_i are the eigenvalues of the Jacobian matrix $\mathbf{J}$ evaluated at the steady state, and the column vectors $\mathbf{v}_i$ are their respective eigenvectors. In general, the eigenvalues λ_i are complex numbers. Therefore, the steady state will be stable if the real parts of λ_1 and λ_2 are both negative. In this way, we can easily generalize the method to a system of n first order differential equations. Let the system be of the form

$$\begin{aligned} \frac{dx_1}{dt} &= f_1(x_1, x_2, \ldots, x_n) \\ \frac{dx_2}{dt} &= f_2(x_1, x_2, \ldots, x_n) \\ &\vdots \\ \frac{dx_n}{dt} &= f_n(x_1, x_2, \ldots, x_n). \end{aligned} \tag{2.17}$$

We assume that a steady solution of the system is given by $\boldsymbol{x}_s = (x_{1s}, x_{2s}, \ldots, x_{ns})$. Then, we introduced a small perturbation about the steady solution

$$\boldsymbol{x}(t) = \boldsymbol{x}_s + \boldsymbol{\zeta}(t). \tag{2.18}$$

Where $\boldsymbol{x} = (x_1, x_2, \ldots, x_n)$ and $\boldsymbol{\zeta}(t) = \left(\zeta_1(t), \zeta_2(t), \ldots, \zeta_n(t)\right)$. Introducing Eq. (2.18) into Eq. (2.17) and keeping only the linear terms with respect to the perturbation, we obtain a system of n equation for the time evolution of the perturbation

$$\frac{d\boldsymbol{\zeta}^T}{dt} = \mathbf{J}\boldsymbol{\zeta}^T. \tag{2.19}$$

Where the Jacobian matrix $\mathbf{J}$ is now an $n \times n$ matrix evaluated at the steady state $\boldsymbol{x}_s$ with elements given by $\mathrm{J}_{ij} = \left(\partial f_i / x_j\right)\Big|_{\mathbf{x}=\boldsymbol{x}_s}$. The general solution of Eq. (2.19) is given by

$$\boldsymbol{\zeta}^T = \mathbf{v}_1 e^{\lambda_1 t} + \mathbf{v}_2 e^{\lambda_2 t} + \cdots + \mathbf{v}_n e^{\lambda_n t}. \tag{2.20}$$

Where the constant column vectors $\mathbf{v}_i$ and the constants λ_i are determined from

$$\mathbf{J}\mathbf{v}_i = \lambda_i \mathbf{v}_i \quad (\text{for } i = 1, 2, \ldots, n). \tag{2.21}$$

Where λ_i are the eigenvalues of the Jacobian matrix $\mathbf{J}$ evaluated at the steady state, and the column vectors $\mathbf{v}_i$ are their respective eigenvectors. In general the eigenvalues λ_i are complex numbers, hence the steady state will be stable if the eigenvalue with the largest real part is negative.

2.3 Linear stability in spatially extended systems

We consider a continuous state variable $u(x,t)$ that depends on t and on a spatial coordinate x. The dynamical system is given by

$$\frac{\partial u(x,t)}{\partial t} = F(u, \partial u/\partial x, \ldots, r). \tag{2.22}$$

Where F is in general a nonlinear function that depends on u and on higher spatial derivatives of u, and it also depends on a parameter r. In experiment the value of the parameter r is varied gradually to take the system out of equilibrium; hence the parameter r is referred to as the control parameter [63].

We assume that Eq. (2.22) has a stationary-state (or basic state) solution $u_0(x)$. We introduce an arbitrary infinitesimal perturbation $\tilde{u}(x,t)$ about $u_0(x)$. Hence, the steady solution with the perturbation is given by

$$u(x,t) = u_0(x) + \tilde{u}(x,t). \tag{2.23}$$

We replace Eq. (2.23) into Eq. (2.22) and linearize the equation (see Sec. 2.2) with respect to the perturbation. Notice that the perturbation has to satisfy the boundary conditions of the system. To execute a linear stability analysis, the perturbation can be expanded as a linear combination of Fourier components [64], which are linearly independent (normal modes)

$$\tilde{u}(x,t) = \sum_k A_k e^{\sigma_k t} e^{ikx}. \tag{2.24}$$

In addition, we can analyze the stability of each of the normal modes separately, since the linearity of the perturbation implies that the modes evolve independent from each other. Thus, a single normal mode of the perturbation can be written as

$$\tilde{u}_k(x,t) = A_k e^{\sigma t} e^{ikx}, \tag{2.25}$$

where σ is the growth rate of a single normal mode of the perturbation and k is the respective wavenumber of this normal mode. Here the constant k will be a real number, if we assume that the system is unbounded in the x direction. This is a consequence of translational invariance in the x direction in order to avoid that the perturbation amplitude diverges at infinity, either at $x \to -\infty$ or $x \to +\infty$. The constant σ is in general a complex number. The perturbation will be linearly unstable when its magnitude grows exponentially with time. This will happen when the real part of the growth rate σ takes a positive value at least in one of the normal modes. Therefore, the steady solution will be stable if all of the growth rates have a negative real part (or equivalently, if the growth rate with the largest real part is negative, the steady solution is stable). In the case of a periodic boundary condition, we have a finite system of length L which is periodic. The perturbation also has to satisfy the boundary condition. That is,

$$\tilde{u}(x,t) = \tilde{u}(x+L,t) \tag{2.26}$$

for any value of x and t. From Eq. (2.24) and Eq. (2.26), we find that $e^{ikL} = 1$. Therefore, in the case of periodic boundary conditions the real number k is restricted to the values

$$k = \frac{2\pi}{L} n, \quad n = 0, \pm 1, \pm 2, \ldots \tag{2.27}$$

We know that the steady solution is stable with respect to the perturbations if for a fixed value of r all of the growth rates $\sigma(k,r)$ have a negative real part. On the contrary, the steady solution is unstable if the growth rates $\sigma(k,r)$ are positive (at least in one of the normal modes). Hence, it is useful to find the neutral stability curve $\mathrm{Re}\{\sigma(k,r)\} = 0$. The plot of this curve in the r-k plane (or space) divides the stable region from the unstable region for the steady solution with respect to the perturbation.

Chapter 3

Hydrodynamics flows and instabilities

Our purpose is to study the propagation of reaction fronts in fluids using the methods of dynamical systems. Fluid motion is a dynamical system described by a set of equations: the Navier-Stokes equations. In this chapter we will focus in two types of steady flow which are exact solutions of the Navier-Stokes equations. These steady, fully developed laminar flows correspond to the plane Poiseuille flow and the plane Couette flow. The velocity profile of a fully develop flow is independent of the downstream coordinate. We assume a two-dimensional incompressible fluid flow to simplify the Navier-Stokes equations. The plane Poiseuille flow is a type of viscous flow which moves between infinite parallel plates. This flow is caused by an externally applied pressure gradient. Another type of viscous flow is the plane Couette flow. In this case, the fluid motion is caused by a moving surface which drags the viscous fluid along with it. Although these solutions of the Navier-stokes equations correspond to steady laminar flows, these flows may become turbulent. Indeed, there is a threshold number related to average fluid velocity (Reynolds number) above which small perturbations will grow fast and the steady stable flow becomes unstable. These small perturbations may be introduced through irregularities in the experimental setup. There are other types of instabilities related to the motion of fluids, such as Rayleigh-Bénard convection caused by a thermal gradient on thin layers [65], and Taylor-Couette flow where the centrifugal force has a destabilizing effect [66,67]. In contrast, the Rayleigh-Taylor instability corresponds to the instability of an interface between two fluids initially at rest due to density gradients under gravity. In this chapter we also describe the Rayleigh-Taylor instability, including viscous fluids and surface tension. The effects of the Rayleigh-Taylor instability on propagating fronts will be discuss in Chap. 6.

3.1 Plane Poiseuille flow

We consider an incompressible steady flow confined by two infinite parallel plates located at $x = 0$ and $x = \mathrm{L}$, being the z-axis the direction of the flow. The

flow is sustained by an externally applied pressure gradient in the z-direction. In this regard, the mass density ρ of the fluid is constant, the mass conservation equation becomes $\nabla \cdot \vec{v} = 0$, and the Navier-Stokes equations for incompressible fluids is given by [68]

$$\rho\left[\frac{\partial \vec{v}}{\partial t} + (\vec{v} \cdot \nabla)\vec{v}\right] = -\nabla p + \mu \nabla^2 \vec{v}. \tag{3.1}$$

Where $\vec{v}$ is the fluid velocity field, p is the pressure and the coefficient μ is the dynamic viscosity (or usually called the viscosity). Since the flow is confined between two parallel plates, the fluid velocity at the plates is zero. We also assume that the flow velocity $\vec{v}$ is only function of x. The continuity equation requires that $\partial v_x / \partial x = 0$, which implies that v_x is a constant. The value of this constant is zero, since $v_x = 0$ at the plates. This result is in agreement with the fact that the flow is along the z-direction and parallel to the plates. Under these circumstances, Eq. (3.1) in components reduces to

$$0 = -\frac{\partial p}{\partial z} + \mu \frac{d^2 v_z}{dx^2} \tag{3.2}$$

and

$$0 = \frac{\partial p}{\partial x}. \tag{3.3}$$

We deduce from Eq. (3.3) that pressure is only function of z. In addition, from Eq. (3.2) we observe that $\partial p / \partial z$ must be a function of z only, while the other term must be a function of x only. Since Eq. (3.2) is valid everywhere between the plates, we conclude that both terms are constant. Thus, the pressure varies linearly along the z-direction. Since pressure is only function of z, Eq. (3.2) becomes

$$0 = -\frac{dp}{dz} + \mu \frac{d^2 v_z}{dx^2}. \tag{3.4}$$

Integrating Eq. (3.4) twice with respect to x, we obtain

$$0 = -\frac{x^2}{2}\frac{dp}{dz} + \mu v_z + Cx + D, \tag{3.5}$$

where C and D are constants, which are determined from the boundary conditions ($v_z = 0$ at the plates). The values of these constants are $C = (\mathrm{L}/2)(dp/dz)$ and $D = 0$. Therefore, the velocity profile of a plane Poiseuille flow shown in Fig. 3.1 is given by

$$v_z = -\frac{1}{2\mu}\frac{dp}{dz}x(\mathrm{L} - x), \tag{3.6}$$

and the mean fluid velocity is given by

$$\bar{v} = \frac{1}{\mathrm{L}}\int_0^{\mathrm{L}} v_z dx = -\frac{\mathrm{L}^2}{12\mu}\frac{dp}{dz}. \tag{3.7}$$

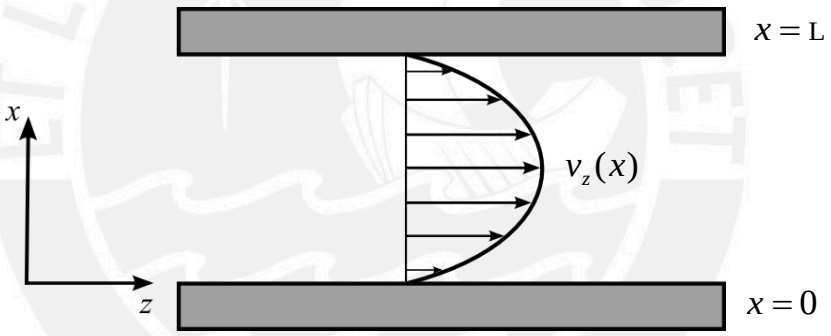

Figure 3.1: Parabolic velocity profile of a plane Poiseuille flow confined between two parallel plates.

3.2 Plane Couette flow

In the case of a Couette flow, the flow is sustained by the relative motion between the parallel plates. We consider that the plate located at $x = \mathrm{L}$ moves with constant speed u in the z-direction, while the other plate, which is located at $x = 0$, is stationary as shown in Fig. 3.2. These plates are parallel to the yz-plane. Taking into account that the flow is only driven by the motion of the plate located at $x = \mathrm{L}$, without any externally imposed pressure gradient, Eq. (3.5) reduces to

$$0 = \mu v_z + Cx + D, \tag{3.8}$$

and the constants C and D are determined from the boundary conditions, which in this case are $v_z = 0$ at $x = 0$, and $v_z = u$ at $x = \mathrm{L}$. The results are $C = -\mu(u/\mathrm{L})$ and $D = 0$. Therefore, the velocity profile of a plane Couette flow is given by

$$v_z = (u/\mathrm{L})\,x. \tag{3.9}$$

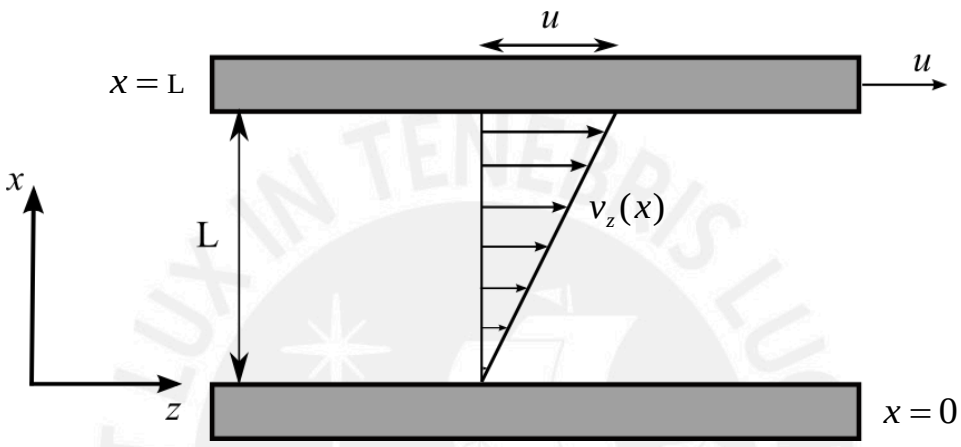

Figure 3.2: Linear velocity profile of a plane Couette flow. The relative velocity between the parallel plates is u.

3.3 Viscous flow in a Hele-Shaw cell

We consider an incompressible fluid flow moving in a narrow space between two stationary parallel plates as shown in Fig. 3.3. This geometry is known as a Hele-Shaw cell. We use a rectangular coordinate system with axes x, y, and z. The plates are parallel to the yz-plane, being z the vertical axis. The x axis is perpendicular to the plates, which are separated by a small gap of thickness d. The plates are located at $x = \pm d/2$. The fluid velocity field $\vec{v}$ between the plates obeys the Navier-Stokes equations

$$\rho\left[\frac{\partial \vec{v}}{\partial t} + (\vec{v}\cdot\nabla)\vec{v}\right] = -\nabla p + \mu\nabla^2\vec{v} + \rho\vec{g}, \tag{3.10}$$

and

$$\nabla\cdot\vec{v} = 0, \tag{3.11}$$

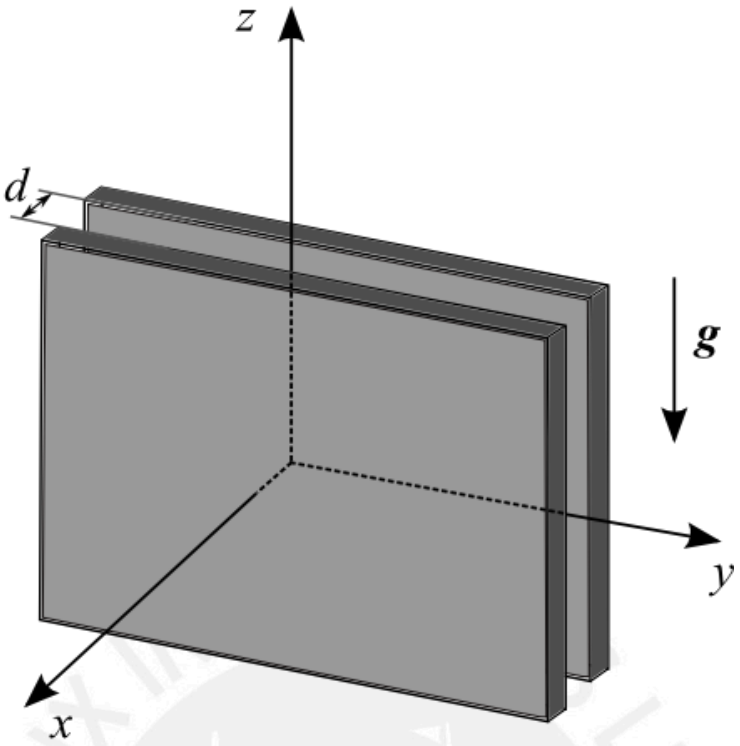

Figure 3.3: Sketch of a Hele-Shaw cell.

where $\vec{g}$ is the acceleration of gravity. Notice that in Eq. (3.10) we have introduced the body force per unit volume ($\rho\vec{g}$). The body force is an external force that acts on a fluid element without physical contact like the gravitational or electromagnetic force. We assume that the gap d between the plates is small and that the flow is slow, so that the flow can be considered steady and parallel to the plates. In other words, no flow takes place in the x-direction ($v_x = 0$). We also assume that v_y, and v_z have parabolic Poiseuille profiles in the x direction [69]. That is, the flow achieves its maximum velocity at $x = 0$ and the velocity of the flow vanishes at the plates of the Hele-Shaw cell in agreement with the boundary conditions: $v_y = v_z = 0$ at $x = \pm d/2$. Thus, the components of the fluid velocity field can be written as

$$\begin{aligned} v_x(x,y,z,t) &= 0 \\ v_y(x,y,z,t) &= \frac{6}{d^2}\left(\frac{d^2}{4} - x^2\right)V_y(y,z,t) \\ v_z(x,y,z,t) &= \frac{6}{d^2}\left(\frac{d^2}{4} - x^2\right)V_z(y,z,t). \end{aligned} \tag{3.12}$$

Where V_y and V_z are the average of v_y and v_z over $-d/2 \le x \le d/2$, respectively. Substituting Eq. (3.12) into Eq. (3.10) and averaging these equations over $-d/2 \le x \le d/2$, we obtain

$$\rho\left[\frac{\partial \vec{\mathrm{V}}}{\partial t}+\frac{6}{5}\left(\vec{\mathrm{V}}\cdot\nabla\right)\vec{\mathrm{V}}\right]=-\nabla P+\rho\vec{\mathrm{g}}+\mu\nabla^2\vec{\mathrm{V}}-\frac{12\mu}{d^2}\vec{\mathrm{V}}, \tag{3.13}$$

Here P is the average of the pressure p over the gap $-d/2 \le x \le d/2$ and all vectors are two dimensional, being defined in the yz-plane. That is, $\vec{\mathrm{V}}=(V_y,V_z)$, $\vec{\mathrm{g}}=(0,-g)$, and the bold gradient $\nabla=(\partial/\partial y,\partial/\partial z)$. Similarly, substituting Eq. (3.12) into Eq. (3.11) and averaging yield $\nabla\cdot\vec{\mathrm{V}}=0$. We obtain the terms of Eq. (3.13) as follows:

- the average value of the time derivative $\partial v_j/\partial t$ of the component v_j of the velocity field

$$\left\langle\frac{\partial v_j}{\partial t}\right\rangle=\frac{1}{d}\int_{-d/2}^{d/2}\frac{\partial v_j}{\partial t}dx=\frac{\partial V_j}{\partial t}\quad(\text{for } j=y,z). \tag{3.14}$$

- the average value of the non-linear term implies the calculus of

$$\begin{aligned}\left\langle v_y\frac{\partial v_j}{\partial y}\right\rangle&=\frac{1}{d}\int_{-d/2}^{d/2}v_y\frac{\partial v_j}{\partial y}dx\\&=V_y\frac{\partial V_j}{\partial y}\frac{1}{d}\int_{-d/2}^{d/2}\left[\frac{6}{d^2}\left(\frac{d^2}{4}-x^2\right)\right]^2dx\\&=\frac{6}{5}V_y\frac{\partial V_j}{\partial y}\quad(\text{for } j=y,z),\end{aligned} \tag{3.15}$$

  and similarly with the z-axis

$$\left\langle v_z\frac{\partial v_j}{\partial z}\right\rangle=\frac{6}{5}V_z\frac{\partial V_j}{\partial z}\quad(\text{for } j=y,z).$$

- finally, the average value of the term with the viscosity

$$\mu\left\langle\left(\frac{\partial^2}{\partial x^2}+\frac{\partial^2}{\partial y^2}+\frac{\partial^2}{\partial z^2}\right)v_j\right\rangle=\mu\left(\frac{\partial^2}{\partial y^2}+\frac{\partial^2}{\partial z^2}\right)V_j+\frac{\mu}{d}\int_{-d/2}^{d/2}\frac{\partial^2 v_j}{\partial x^2}dx$$

$$=\mu\nabla^2 V_j+\mu V_j\int_{-d/2}^{d/2}\frac{\partial^2}{\partial x^2}\left[\frac{6}{d^2}\left(\frac{d^2}{4}-x^2\right)\right]dx \qquad (3.16)$$

$$=\mu\left(\nabla^2 V_j-\frac{12}{d^2}V_j\right) \qquad (\text{for } j=y,z).$$

In the case of a small gap between the plates ($d\to 0$) and a steady laminar flow ($\partial\vec{V}/\partial t=0$), we can assume that the partial derivatives of V_y and V_z with respect to y and z are also negligible in contrast to the partial derivatives of V_y and V_z with respect to x. Hence

$$\frac{\partial V_j}{\partial y}=\frac{\partial V_j}{\partial z}=\frac{\partial^2 V_j}{\partial y^2}=\frac{\partial^2 V_j}{\partial z^2}=0 \quad (\text{for } j=y,z). \qquad (3.17)$$

With these substitutions, Eq. (3.13) becomes

$$\vec{\mathrm{V}}=-\frac{K}{\mu}(\nabla P-\rho\vec{\mathrm{g}}) \qquad (3.18)$$

where $K=d^2/12$ is the permeability of the Hele-Shaw cell. Equation (3.18) is known as Darcy's law, which governs flows in porous media. Thus Eq. (3.18) describes a two-dimensional flow in a Hele-Shaw cell being analogous to Darcy's law which is a phenomenological law for flow in porous media.

3.4 Rayleigh-Taylor instability

The instability of a flat interface that separates two fluids of different densities under gravity occurs when the denser fluid is supported by the less dense fluid. This instability, known as Rayleigh-Taylor instability, can also take place when the fluids are accelerated towards the denser fluid [39].

We consider a simple case of Rayleigh-Taylor instability by assuming two immiscible and incompressible fluids without viscosity whose flow is irrotational. This situation corresponds to a high Reynolds number flow, in which the viscous term of the Navier-Stokes equations becomes negligible. The two incompressible inviscid fluids are initially at rest, and they are separated by a

flat interface under gravity. Let ρ_+ be the density of the fluid located in the upper half-space $z>0$, whereas ρ_- corresponds to the density of the fluid located in the lower half-space $z<0$. We use a rectangular coordinate system and the interface is located at $z=0$. The z axis is the vertical axis, while the x and y axes are parallel to the interface as shown in Fig. 3.4.

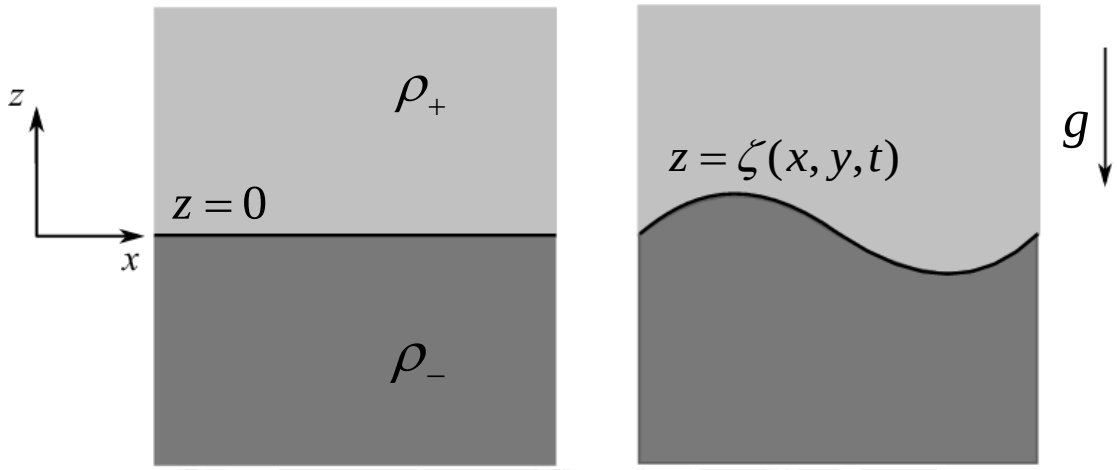

Figure 3.4: (a) Two incompressible inviscid fluids separated by a flat interface under gravity. (b) The interface between two incompressible inviscid fluids is subject to small wave-like perturbation.

In this case the Navier-Stokes equations [Eq. (3.10)] reduces to Euler's equation

$$\frac{\partial \vec{v}}{\partial t}+(\vec{v}\cdot\nabla)\vec{v}+\frac{1}{\rho}\nabla p-\vec{g}=0, \tag{3.19}$$

We assume that the flow is irrotational so that we can use a potential function for the velocity field $\vec{v}=\nabla\psi$. In addition, we use the identity $(\vec{v}\cdot\nabla)\vec{v}=\nabla\left(v^2/2\right)-\vec{v}\times\nabla\times\vec{v}$. With these substitutions, Eq. (3.19) becomes

$$\nabla\left(\frac{\partial\psi}{\partial t}+\frac{v^2}{2}+\frac{p}{\rho}+gz\right)=0. \tag{3.20}$$

Integrating Eq. (3.20) we obtain the time-dependent Bernoulli's equation

$$\rho\frac{\partial\psi}{\partial t}+\frac{1}{2}\rho v^2+p+\rho gz=f(t), \tag{3.21}$$

where the Bernoulli constant may now be a function of time because the velocity potential is now unsteady. We also use the fact that the fluid is incompressible so the density is constant and the continuity equation becomes $\nabla\cdot\vec{v}=0$, leading to Laplace's equation

$$\nabla^2\psi=0. \tag{3.22}$$

There exists a base solution that satisfies Eq. (3.22) and it corresponds to $\psi=0$ with a flat interface. We denote this base solution corresponding to equilibrium state (or basic state) by ψ_0. In order to analyze the stability of the flat interface, we introduce small perturbations to the equilibrium state. That is, a potential perturbation to the field velocity and a surface perturbation. For simplicity, we are going to consider a two dimensional fluid motion and execute a linear stability analysis to determine the stability of the interface. We designate the potential perturbation to the field velocity by ψ' and the surface perturbation by $\zeta(x,t)$. Notice that the fluid motion whose stability is being studied arises from these small perturbations. We assume sinusoidal perturbations of the equilibrium state since the linearity of the problem allows us to represent any perturbation as linear superposition of normal modes. Since these normal modes constitute an orthonormal basis, the stability of each of the modes is analyzed independently. Let us consider a simple perturbation with frequency ω and wavenumber k, being proportional to $e^{i(kx-\omega t)}$. Notice that the proportionality factor may be a function of z. There is no constraint in the x direction, hence the wavenumber k is real (Sec. 2.3). On the other hand, the frequency ω is in general a complex number. That is $\omega=\omega_r+i\omega_i$, thus the system will be unstable for any value of k if $\omega_i>0$. This analysis corresponds to a single-mode perturbation, which is a perturbation with only one wavelength applied to the interface. We proceed to obtain a relation between the wavenumber k of the mode and its frequency ω. This relation is referred to as dispersion relation $\omega=\omega(k)$. Thus, if we find a frequency ω whose imaginary

part is positive ($\mathrm{Im}\{\omega\} > 0$) for at least one real value of k, the system will be linearly unstable.

Therefore, to analyze the linear stability of the interface, we consider normal mode perturbations with frequency ω and wavenumber k. The system is subject to three boundary conditions. The first condition requires that the potential perturbations of the fluid velocity ψ' decay exponentially with z. For this reason, these potential perturbations are often referred to as surface modes. The second condition requires that the mass flow not cross the interface $\zeta(x,t)$. Hence, the fluid particles can only move tangentially to the fluid interface. Since the surface $S = z - \zeta(x,t) = 0$ describes the interface in motion at any time, the total time derivative of S must be zero: $\partial S/\partial t + \vec{v} \cdot \nabla S = 0$. This condition is also referred to as kinematic boundary condition. The third condition requires that in the absence of surface tension, the normal stress should be continuous across the interface. This results in continuity of the pressure at the interface.

Replacing $\psi = \psi_0 + \psi'$ in Eq. (3.22), we obtain: $\nabla^2(\psi_0 + \psi') = \nabla^2\psi' = 0$. We look for solutions of the Laplace's equation corresponding to the normal mode with frequency ω and wavenumber k: $\psi' = A(z)e^{ikx}e^{-i\omega t}$. Hence the Laplace's equation leads us to

$$\frac{d^2A}{dz^2} - k^2A = 0. \tag{3.23}$$

In general, the solution of Eq. (3.23) has the form $A = \varphi_+ e^{-kz} + \varphi_- e^{+kz}$, where φ_+ and φ_- are unknown constants. However, in order to satisfy that the solution be bounded at $z \to +\infty$, φ_- has to be zero for $z > 0$. Similarly for $z < 0$, $\varphi_+ = 0$. Therefore the solution must have the form

$$\psi' = \begin{cases} \varphi_+ e^{i(kx-\omega t)-kz} & \text{for } z > 0 \\ \varphi_- e^{i(kx-\omega t)+kz} & \text{for } z < 0 \end{cases} . \tag{3.24}$$

The solutions for φ_+ and φ_- arise from the kinematic boundary condition. We can calculate the normal unit vector $\hat{n}$ by using $\hat{n} = \nabla S / |\nabla S|$. In the case of a two dimensional flow, $\nabla S = -\hat{e}_x \partial\zeta/\partial x + \hat{e}_z$, where $\hat{e}_x$ and $\hat{e}_z$ are unit vectors along the positive axes x and z, respectively; and $|\nabla S| = \left[(\partial\zeta/\partial x)^2 + 1 \right]^{1/2}$. Considering small perturbations ζ, $|\nabla S| \approx 1$ up to second order in ζ. Hence the kinematic boundary condition can be approximated as

$$\partial\zeta/\partial t = \vec{v} \cdot \nabla S \approx \vec{v} \cdot \vec{n} \approx v_z = \frac{\partial \psi'}{\partial z}. \tag{3.25}$$

Substituting a normal mode for the surface perturbation

$$\zeta(x,t) = \zeta_0 e^{i(kx - \omega t)}, \tag{3.26}$$

we obtain

$$\varphi_\pm = \pm \frac{\omega \zeta_0}{k} i. \tag{3.27}$$

In the absence of surface tension, the jump of the pressure across the interface must be zero:

$$[p]_{z=\zeta} = 0, \tag{3.28}$$

where the bracket means the jump of pressure across $z = \zeta$. In Eq. (3.21) we set the time function $f(t)$ equal to zero, because we assume that the disturbances decay considerable far from the interface and the time function does not depend on z. Using Eq. (3.28) and Eq. (3.21) with $f(t) = 0$ and $v = 0$, we obtain

$$\rho_+ \frac{\partial \psi'}{\partial t} + \rho_+ g\zeta = \rho_- \frac{\partial \psi'}{\partial t} + \rho_- g\zeta. \tag{3.29}$$

Expanding Eq. (3.29) about $z = 0$ and keeping only the linear terms on ψ', we obtain

$$(\rho_- - \rho_+) g\zeta_0 + i\omega(\rho_+ \varphi_+ - \rho_- \varphi_-) = 0. \tag{3.30}$$

Finally, using Eq. (3.27) we obtain the following dispersion relation

$$\omega^2 = kg\frac{(\rho_- - \rho_+)}{(\rho_- + \rho_+)}. \tag{3.31}$$

From Eq. (3.31), we observe that if the denser fluid is on top of the less dense fluid then $\rho_- - \rho_+ < 0$ and the frequency will be complex. We are interested in determine the condition under which the system is unstable. In general the frequency is a complex number $\omega = \omega_r + i\omega_i$, and our solution is proportional to $e^{-i\omega t}$. Since $e^{-i\omega t} = e^{-i\omega_r t}e^{\omega_i t}$, the flow is unstable if $\omega_i > 0$ for at least one real value of k. In the case of Eq. (3.31), the frequency could be real or purely imaginary. We define $\omega = i\sigma$ and we look for the condition under which $\sigma > 0$. This happens when $\rho_- - \rho_+ < 0$. Thus, the perturbations will grow exponentially given rise to Rayleigh-Taylor instabilities when the denser fluid is on top of the less dense fluid.

We now want to take into account the surface tension in the dispersion relation obtained above [Eq. (3.31)]. In this case, the pressure difference across the interface tends to curve the interface in order to keep the force balance on it. The condition of force balance on any surface element of the interface leads us to the Young-Laplace equation [68]

$$[p]_{z=\zeta} = -\gamma \nabla \cdot \hat{n}. \tag{3.32}$$

Here the pressure jump across the interface is denoted by the brackets and it is defined as the pressure of the fluid above the interface minus the pressure of the fluid below the interface, γ is the surface tension and $\hat{n}$ is the normal unit vector to the interface. The curvature of the interface, being positive when the center of curvature is in the fluid above the interface, is given by

$$\kappa = -\nabla \cdot \hat{n} = \frac{\partial^2 \zeta / \partial x^2}{\left[1 + \left(\partial \zeta / \partial x\right)^2\right]^{3/2}}. \tag{3.33}$$

Keeping only the linear terms and assuming small perturbations, Eq. (3.32) becomes

$$[p] = \gamma \frac{\partial^2 \zeta}{\partial x^2}. \tag{3.34}$$

Therefore, surface tension introduces a jump discontinuity in the pressure, replacing Eq. (3.28) by Eq. (3.34). Since we expand this expression about $z = 0$, we evaluate Eq. (3.34) at $z = 0$ instead of $z = \zeta$. From Eq. (3.34) and Eq. (3.21) with $f(t) = 0$ and $v = 0$, we obtain

$$-\rho_- \frac{\partial \psi'}{\partial t} - \rho_- g\zeta + \rho_+ \frac{\partial \psi'}{\partial t} + \rho_+ g\zeta = -\gamma \frac{\partial^2 \zeta}{\partial x^2}. \tag{3.35}$$

Expanding Eq. (3.35) about $z = 0$ and keeping only the linear terms on ψ', we obtain

$$(\rho_+ - \rho_-) g\zeta_0 + i\omega(\rho_- \varphi_- - \rho_+ \varphi_+) = \gamma \zeta_0 k^2. \tag{3.36}$$

Replacing Eq. (3.27) into Eq. (3.36) we obtain the dispersion relation

$$\omega^2 = \frac{(\rho_- - \rho_+)kg + \gamma k^3}{(\rho_- + \rho_+)}, \tag{3.37}$$

where the surface tension has a stabilizing effect. The interface will be unstable if ω^2 is negative.

The viscous effects are often neglected in the Rayleigh-Taylor instability when we work with thick layers. However, when we confine the fluids in a porous medium or in a Hele-Shaw cell, the viscosity becomes relevant [70]. In this case, the velocity field is governed by Darcy's law [Eq. (3.18)] and we neglect the contribution of viscosity to the normal stress at the interface, so that the normal stress balance reduces to the Young-Laplace equation [Eq. (3.32)]. Using Eq. (3.18) and the velocity potential ψ, which obeys $\vec{v} = \nabla \psi$, we obtain

$$\psi = -\frac{K}{\mu}(p + \rho g z). \tag{3.38}$$

Similarly, we introduce a small perturbation to the field velocity given by Eq. (3.24) and a surface perturbation given by Eq. (3.26). Using these equations together with Eq. (3.32) and Eq. (3.38) we obtain

$$-\frac{\mu_+}{K}\varphi_+ - \rho_+ g\zeta_0 + \frac{\mu_-}{K}\varphi_- + \rho_- g\zeta_0 = -\gamma\zeta_0 k^2. \tag{3.39}$$

Here K is the permeability of the porous medium or the Hele-Shaw cell, μ_+ is the viscosity of the upper fluid and μ_- is the viscosity of the lower one. Replacing Eq. (3.27) into Eq. (3.39), and defining $\omega = \sigma i$, we obtain the dispersion relation

$$\sigma = -K\frac{(\rho_- - \rho_+)gk + \gamma k^3}{\mu_+ + \mu_-}. \tag{3.40}$$

It is worth mentioning that the last result also corresponds to the dispersion relation of the Saffman-Taylor instability with zero throughflow velocity [71]. Indeed, when a less viscous fluid is used to displace a more viscous one in a porous medium, the interface between the two fluids develops finger-like patterns which are referred to as viscous fingering.

Chapter 4

Propagating reaction fronts

Propagating fronts can be found in many natural phenomena separating different coexisting phases such as, forest fire [16], crystal growth, landslide, epidemics [17], and cell populations. For example, in an epidemic we can consider the front as the interface which separates infected people from uninfected people. We can model this propagating front by a reaction-diffusion equation to predict the speed of the epidemic and the change in the percentage of infected people as a function of time. In this case diffusion plays the role of spreading the agent of epidemic, while reaction specifies how uninfected people react with the agent of epidemic. Indeed, the natural phenomena mentioned above correspond to reaction-diffusion systems. Thus, solving the reaction-diffusion equation, we obtain information about the evolution of the different phases.

Other methods relay on a thin front approximation. This approximation considers the chemical front as a surface (or interface with negligible thickness) that separates reacted from unreacted fluid. Among these methods we have the eikonal-curvature relation that shows the dependency of the normal velocity of the reaction front on the local front curvature [8,72,28]. Considering a thin interface between reactants and products, the Kuramoto-Sivashinsky equation can be used to model the evolution of reaction fronts with diffusive instabilities [29] and thermal-diffusive flame instabilities in the propagation of plane flame fronts [73].

4.1 Reaction-diffusion equation

Random particle motion causes the transport of matter from one place to another which is referred to as diffusion. A diffusion flux (J) is defined as the number of particles passing through a unit cross-sectional area per unit time, where the particles can be atoms, molecules, or ions [74]. The concentration of particles (or number density) corresponds to the number of particle per unit volume.

The Fick's first law, which is based on observations, states that diffusion flux always points in the direction from high concentration to low concentration [75], and it can be represented in a one-dimensional form as

$$J = -D\frac{\partial c}{\partial x}, \tag{4.1}$$

where J is the flux of particles (diffusion flux), D is the diffusion coefficient or diffusivity, and c is the concentration of particles.

In most of the cases the concentration of particles at any position changes with time, which implies that the flux also changes with time. The non-steady state diffusion is described by Fick's second law. To obtain Fick's second law in one-dimension, we consider a rectangular parallelepiped volume element with two faces of unit area perpendicular to the x-axis as shown in Fig. 4.1. One of these faces is located at x, while the other is located at $x+\Delta x$. The net incoming flux of particles into this volume element is given by the difference between the incoming flux and the outgoing flux: $J(x)-J(x+\Delta x)$. Assuming that $\Delta x \to 0$, we can expand $J(x+\Delta x)$ about x using a Taylor series and keeping only the linear terms we have $J(x+\Delta x) \approx J(x)+(\partial J/\partial x)\Delta x$. The conservation of mass implies that the net incoming flux of particles into the volume element must be equal to the rate of accumulation of particles into this volume element

$$-\frac{\partial J}{\partial x}\Delta x = \left(\frac{\partial c}{\partial t}\right)\Delta x, \tag{4.2}$$

reducing simply to

$$-\frac{\partial J(x,t)}{\partial x} = \frac{\partial c(x,t)}{\partial t}. \tag{4.3}$$

Replacing Eq. (4.1) into Eq. (4.3), and assuming that D does not depend on x, we obtain a partial differential equation (PDE) in one-dimension for non-steady state diffusion, referred to as a diffusion equation in one-dimension [76]

$$\frac{\partial c(x,t)}{\partial t} = D\frac{\partial^2 c(x,t)}{\partial x^2}. \tag{4.4}$$

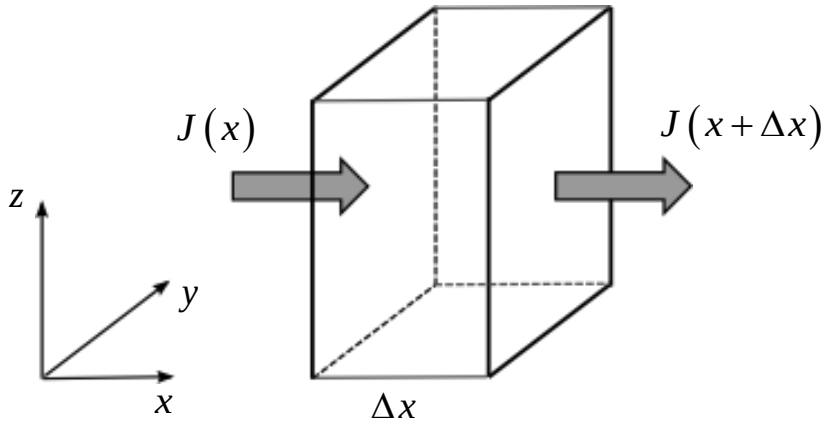

Figure 4.1: Sketch of a rectangular parallelepiped volume element with two faces of unit area perpendicular to the x-axis. The arrows indicate the incoming flux and the outgoing flux of particles into this volume element.

Equation (4.4) corresponds to Fick's second law in one-dimension, and this equation can be written in three-dimension as

$$\frac{\partial c}{\partial t} = \nabla \cdot \left(D \nabla c \right). \tag{4.5}$$

In the case of steady state diffusion with D constant, the concentration c does not change by time, so that Eq. (4.5) becomes Laplace's equation

$$\nabla^2 c = 0. \tag{4.6}$$

The solution of Eq. (4.6) corresponds to Fick's first law for steady state diffusion as expected. However, in general, the solutions of Eq. (4.5) depend on an initial condition and corresponding boundary conditions.

A reaction-diffusion (RD) equation appears in the study of population growth and chemical reactions. It includes a reaction term besides a diffusion term, having the following form for one component in one spatial dimension

$$\frac{\partial c}{\partial t} = D \nabla^2 c + f\left(c \right). \tag{4.7}$$

Here c represents the population density or the concentration of a substance. The smooth function $f(c)$ is in general a nonlinear function which represents the local change of c. For example, in the case of population growth, it is related to the rate of birth (or death) and to the carrying capacity of the biological species in the specific environment. In the case of chemical reaction it represents the chemical reaction rate law. Equation (4.7) have been studied by Fisher [20] and by Kolmogorov, Petrovsky, and Piskunov [21] in the context of population dynamics. They used Eq. (4.7) with $f(c)=\alpha c(1-c)$ to study the propagation of a dominant gene. In this case the solution to this equation corresponds to a propagating front [77], and it is referred to as the FKPP equation. This equation can be generalized to include many species with their interrelations and their diffusion constants, giving rise to much more complex spatiotemporal propagation phenomena [78].

4.2 Reaction-diffusion equation with cubic order autocatalysis

A very important type of reaction front arises in the case of cubic autocatalysis [1,79]. Cubic chemical autocatalysis arises from a two species reaction of the form

$$A+2B\rightarrow 3B,\quad \text{rate}=kab^2. \tag{4.8}$$

Where A is the reactant with concentration a and diffusion coefficient D_a, B is the autocatalyst with concentration b and diffusion coefficient D_b; being k the rate constant [22,80]. The iodate-arsenous acid (IAA) reaction with adequate concentrations of the reactants can be described by a one variable (scalar) reaction-diffusion equation with cubic reaction kinetics [19,6,81]. This equation exhibits a solution in the form of $c(x,t)=c(x-vt)$. Since the propagation velocity v of the front is constant and the front travels without changing its shape, it will be useful to change to a reference frame co-moving with the front. In this moving reference frame Eq. (4.7) becomes an ordinary differential equation

$$-v\frac{dc}{d\xi} = D\frac{d^2c}{d\xi^2} + f(c). \tag{4.9}$$

Here $c = c(\xi)$ and $\xi = x - vt$. Using $f(c) = -\alpha(c-c_1)(c-c_2)(c-c_3)$ with α a positive constant, we present the exact analytical solution of Eq. (4.7) based on the work of Saul and Showalter [19]. The steady state solutions c_i are obtained from $f(c_i) = 0$. We assume that $c_1 < c_2 < c_3$, being c_1 and c_3 linearly stable to small perturbations ($\partial f/\partial c < 0$), while the intermediate steady state solution c_2 is linearly unstable ($\partial f/\partial c > 0$). We are looking for a wave-front solution, which moves with speed v between two steady states. In this case we work with c_1 and c_3. The front speed v can be positive or negative, because Eq. (4.7) is invariant with respect to the transformation $x \to -x$. Since we want a travelling wave between c_1 and c_3, the boundary conditions are as follows: $\lim_{\xi\to-\infty} c(\xi) = c_3$ and $\lim_{\xi\to+\infty} c(\xi) = c_1$. We define $G(c) = dc/d\xi$ as in Ref. [19], so that $d^2c/d\xi^2 = (dG/dc)(dc/d\xi) = (dG/dc)G$. Replacing in Eq. (4.9) we obtain

$$-vG - DG\frac{dG}{dc} = f. \tag{4.10}$$

Since we also want $G(c)$ to link the steady states c_1 and c_3, from Eq. (4.10) we find that $G(c_1) = G(c_3) = 0$. In addition, from Eq. (4.10) we also notice that if dG/dc is of order n, G must be of order $n+1$, and f must be of order $2n+1$. However, we know that $f(c)$ is of order 3. Thus, G must be of order 2, having the form

$$G = k(c-c_1)(c-c_3). \tag{4.11}$$

Replacing Eq. (4.11) and its derivative into Eq. (4.10), and using the fact that $f(c) = (\alpha/k)(c_2 - c)G$, we obtain

$$(c-c_1)(c-c_3)\left\{(2Dk^2 - \alpha)c - Dk^2(c_1+c_3) + kv + \alpha c_2\right\} = 0. \tag{4.12}$$

Since Eq. (4.12) must be zero for all values of c, the only way is making

$$2Dk^2 - \alpha = 0, \tag{4.13}$$

and

$$-Dk^2\left(c_1 + c_3\right) + kv + \alpha c_2 = 0. \tag{4.14}$$

From Eq. (4.13) we obtain the value of $k = \left(\alpha/2D\right)^{1/2}$, and we choose its positive value to get $dc/d\xi < 0$ in order to satisfy the boundary conditions. Replacing the value of k in Eq. (4.14) we obtain

$$v = \left(2D\alpha\right)^{1/2}\left[\frac{1}{2}\left(c_1 + c_3\right) - c_2\right]. \tag{4.15}$$

We also replace the value of k in Eq. (4.11) and using $G(c) = dc/d\xi$, we obtain

$$\frac{dc}{d\xi} = k\left(c - c_1\right)\left(c - c_2\right). \tag{4.16}$$

Solving this first order differential equation [Eq. (4.16)], we obtain the front solution with $\xi = x - vt$

$$c\left(x,t\right) = \frac{c_1 + c_3}{2} + \frac{c_1 - c_3}{2}\tanh\left(-\frac{1}{2}\left[k\left(c_1 - c_3\right)\left(x - vt\right) + B\right]\right), \tag{4.17}$$

where B is a constant to be determined from the initial conditions.

The IAA system can be described by two main reactions [6]. The Dushman reaction, where iodide is oxidized by iodate [82]:

$$\mathrm{IO_3^- + 5I^- + 6H^+ = 3I_2 + 3H_2O}. \tag{4.18}$$

Here $\mathrm{IO_3^-}$ is an iodate ion, $\mathrm{I^-}$ is an iodide ion, and $\mathrm{H^+}$ is a hydrogen ion. The second reaction corresponds to the Roebuck reaction, in which arsenous acid is oxidized by iodine [83]:

$$\mathrm{H_3AsO_3 + I_2 + H_2O = H_3AsO_4 + 2I^- + 2H^+}. \tag{4.19}$$

The acid on the left-hand side of Eq. (4.19) is the arsenous acid, while the acid on the right-hand side is the arsenic acid. The rate laws of these reactions have

been obtained empirically [6]. The rate law for the Dushman reaction [Eq. (4.18)] is given by

$$-\frac{1}{5}\frac{d[\mathrm{I}^-]}{dt} = \left(k_a + k_b[\mathrm{I}^-]\right)[\mathrm{I}^-][\mathrm{IO}_3^-][\mathrm{H}^+]^2, \tag{4.20}$$

while the rate law for the Roebuck reaction [Eq. (4.19)] is given by

$$-\frac{d[\mathrm{I}_2]}{dt} = k_c \frac{[\mathrm{I}_2][\mathrm{H}_3\mathrm{AsO}_3]}{[\mathrm{I}^-][\mathrm{H}^+]}. \tag{4.21}$$

Where the rate constants are $k_a = 4.50\times10^3 \mathrm{M}^{-3}\mathrm{s}^{-1}$, $k_b = 4.36\times10^8 \mathrm{M}^{-4}\mathrm{s}^{-1}$, and $k_c = 3.20\times10^{-2}\mathrm{Ms}^{-1}$.

In the case of iodide fronts in the IAA reaction with arsenous acid in stoichiometric excess to iodate, the net reaction is given by [6]

$$\mathrm{IO}_3^- + 3\mathrm{H}_3\mathrm{AsO}_3 = \mathrm{I}^- + 3\mathrm{H}_3\mathrm{AsO}_4. \tag{4.22}$$

Assuming that iodate and iodide have the same diffusion coefficient and that the initial concentration of iodide is negligible in contrast to the initial concentration of iodate, the IAA reaction can be described by a one variable reaction-diffusion equation. The IAA reaction kinetics is modeled by the cubic rate law $f(c) = -\alpha c(c+c_s)(c-1)$. Here c is the normalized concentration of iodide with respect to the initial concentration of iodate [50]. The value of c_s depends on the empirical rate constants k_a and k_b and it is also normalized with respect to the initial concentration of iodate, being $c_s > 0$. In this case the spatially homogeneous steady states are: $c = 1$ and $c = 0$, and the wave-front solution will move from the $c = 1$ region to the $c = 0$ region, being $c = 1$ the final reacted state which corresponds to the thermodynamic equilibrium. Using Eq. (4.15), we obtain the speed of the wave-front solution, which is given by

$$v = (2\alpha D)^{1/2}\left(\frac{1}{2} + c_s\right), \tag{4.23}$$

and from Eq. (4.17), we obtain the traveling wave-front solution, which is given by

$$c(x,t)=\frac{1}{2}+\frac{1}{2}\tanh\left[-\frac{1}{2}\sqrt{\frac{\alpha}{2D}}(x-vt)+B\right]. \tag{4.24}$$

The initial concentrations values used in typical wave experiments by Hanna *et al.* [6] are $\left[IO_3^-\right]_0=5.00\times10^{-3}\text{M}$, and $\left[H_3AsO_3\right]_0=1.55\times10^{-2}\text{M}$. We assume the same diffusion coefficient for iodide and iodate $D=2.0\times10^{-3}\text{mm}^2\text{s}^{-1}$. The value of c_s depends on empirical rate constants related to the process of oxidation of iodide by iodate [6] and on the initial concentration of iodate $c_s=(k_a/k_b)/\left[IO_3^-\right]_0=\left(4.50\times10^3\text{M}^{-3}\text{s}^{-1}/4.36\times10^8\text{M}^{-4}\text{s}^{-1}\right)/5.00\times10^{-3}\text{M}\approx0.00206.$

The constant $\alpha=\left(\left[IO_3^-\right]_0\right)^2k_b\left[H^+\right]^2$ depends on the constant hydrogen ion concentration involved in the process of reduction of iodine by arsenous acid [19,6]: $\alpha=\left(5.00\times10^{-3}\text{M}\right)^2\left(4.36\times10^8\text{M}^{-4}\text{s}^{-1}\right)\left(7.1\times10^{-3}\text{M}\right)^2=0.55\text{s}^{-1}$. Replacing this values in Eq. (4.23) we obtain a front propagation speed of 2.36×10^{-2} mm/s, in agreement with the experimental results [6].

4.3 Eikonal equation

A variety of chemical systems exhibit propagating chemical waves such as the Belousov-Zhabotinsky (BZ) reaction and the iodate-arsenous acid (IAA) reaction [84]. Although the propagation of a chemical wave in a two-dimensional system is not difficult to obtain experimentally, modeling two dimensional wave-fronts is more difficult because of their curvature. Previous works [8] without fluid motion have shown that the normal speed of a curved wave-front is related to its curvature. This relation is referred to as the eikonal equation and it is given by

$$V_n=V_0+D\kappa, \tag{4.25}$$

where V_n is the normal speed of the wave-front, V_0 is the speed of a plane wave (a planar front), D is the molecular diffusivity, and κ is the curvature of the wave-front. The curvature κ is positive if the front propagates toward the center of curvature. In Fig. 4.2 we observe that the eikonal equation increases

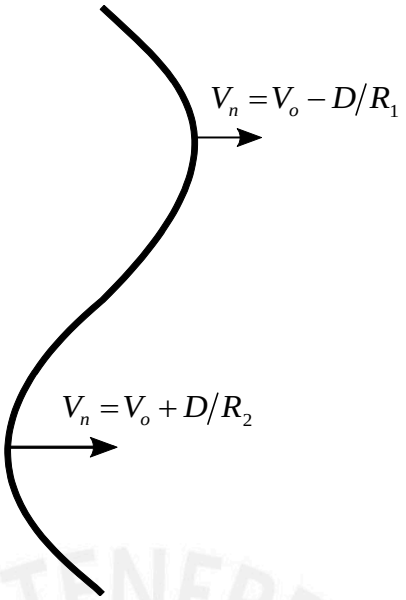

Figure 4.2: The eikonal equation increases the normal velocity of the points of the wavefront with positive curvature and decreases the normal velocity of the other points with negative curvature.

the normal velocity of the points of the wave-front with positive curvature and decreases the normal velocity of the other points with negative curvature. Thus, Eq. (4.25) tends to flatten the wave-front. In order to get a qualitative understanding to this equation, imagine the propagation of a two-dimensional circular wave-front in polar coordinates. The evolution of this circular front is according to reaction-diffusion equation given by

$$\frac{\partial c}{\partial t} = D\left(\frac{\partial^2 c}{\partial r^2} + \frac{1}{r}\frac{\partial c}{\partial r}\right) + f(c). \tag{4.26}$$

On the other hand, the evolution of a one dimensional reaction-diffusion front advected by a constant flow of speed $\tilde{v}$ can be rewritten as

$$\frac{\partial c}{\partial t} = D\frac{\partial^2 c}{\partial x^2} + \tilde{v}\frac{\partial c}{\partial x} + f(c). \tag{4.27}$$

Since the speed of the advecting flow is opposite to the front propagation, the speed of the front in Eq. (4.27) is $v = v_0 - \tilde{v}$, where v_0 would be the velocity of the front without this supposed advection term. If we compare Eq. (4.26) with

Eq. (4.27), the term $(D/r)(\partial c/\partial r)$ in Eq. (4.26) can be interpreted as an advection term, being $v = D/r$ the velocity of this supposed flow. Hence, the normal front velocity would be

$$v_n = v_0 - v = v_0 - \frac{D}{r}. \tag{4.28}$$

Eq. (4.28) gives us the meaning of the eikonal equation, in which we add to the flat front velocity a term proportional to the front curvature. This result corresponds to the case of negative curvature, as shown in Fig. 4.2 for $\kappa = -R_1^{-1}$. Here the front is moving away from the center of curvature, while its normal velocity decreases in agreement with Eq. (4.25).

4.4 Kuramoto-Sivashinsky equation

Propagating chemical wave with diffusive instabilities and flame fronts with thermal-diffusive instabilities can be described by the Kuramoto-Sivashinsky (KS) equation [26,73]. The one dimensional KS equation is given by

$$\frac{\partial u}{\partial t} = \nu \frac{\partial^2 u}{\partial x^2} - \frac{\partial^4 u}{\partial x^4} + u \frac{\partial u}{\partial x}, \tag{4.29}$$

where $u(x,t)$ is an scalar field and $x \in [0, \mathrm{L}]$. This partial differential equation is nonlinear due to the term $u\partial u/\partial x$. We also observe a diffusion term $\nu \partial^2 u/\partial x^2$, which causes instability when $\nu < 0$. The coefficient ν depends on the physical characteristics of the system. In the case of autocatalytic reaction fronts involving two species, the coefficient ν depends on the ratio of diffusivities between the reactant and the autocatalytic substance [24,29]. In this thesis we work with $\nu < 0$, which allows for unstable flat fronts and steady stable curved fronts, including oscillating and chaotic solutions.

The KS equation is non-integrable and therefore, there are no explicit solutions. In other words, there are no solutions of the form $u = u(x,t)$. The second form of the KS equation can be obtain by setting $u = \partial h/\partial x$ and integrating Eq. (4.29) with respect to x. Considering $\nu = -1$, this gives

$$\frac{\partial h}{\partial t} = -\frac{\partial^2 h}{\partial x^2} - \frac{\partial^4 h}{\partial x^4} + \frac{1}{2}\left(\frac{\partial h}{\partial x}\right)^2. \tag{4.30}$$

Equation (4.30) has a flat front solution: $h(x,t) = 0$. We use the normal mode method to analyze the linear stability of the flat front solution. Let us introduce a simple perturbation with frequency ω and wavenumber k, being proportional to $e^{i(kx-\omega t)}$. This means that the perturbation has the form $\tilde{h}(x,t) = Ae^{i(kx-\omega t)}$, where A is a small constant. In addition, we consider the following boundary conditions: $\partial h/\partial x = 0$ and $\partial^3 h/\partial x^3 = 0$ [85]. Taking into account the boundary conditions, the perturbation can be written as $\tilde{h}(x,t) = A\cos(kx)e^{-i\omega t}$, where $x \in [0, \mathrm{L}]$ and $k = n\pi/\mathrm{L}$. Replacing the flat front solution with the addition of the perturbation into Eq. (4.30), and keeping only the linear terms with respect to the perturbation, we obtain

$$-i\omega = k^2 - k^4. \tag{4.31}$$

We define $\omega = \sigma i$, so that the flat front will be unstable if $\sigma > 0$. The dispersion relation is given by

$$\sigma = k^2 - k^4. \tag{4.32}$$

In Fig 4.3, we show the linearized dispersion relation for the KS equation. For small values of k, the growth rate σ is positive, indicating that the flat front solution is unstable. As we increase k, the growth rate σ increases until it reaches a maximum value of 0.25 at $k = 0.707$, it then decreases. Apart from the trivial solution, we observe that the flat front solution has critical stability $(\sigma = 0)$ at $k = 1$. The growth rate σ is negative for $k > 1$, indicating that the flat front solution is stable in this region. Since $k = n\pi/\mathrm{L}$, if the lowest mode $(n = 1)$ is negative, all the other modes will also be negative and the flat front will be stable. Hence, we have

$$\left(\frac{\pi}{\mathrm{L}}\right)^2 - \left(\frac{\pi}{\mathrm{L}}\right)^4 < 0. \tag{4.33}$$

Therefore, the flat front will be stable for $\mathrm{L} < \pi$.

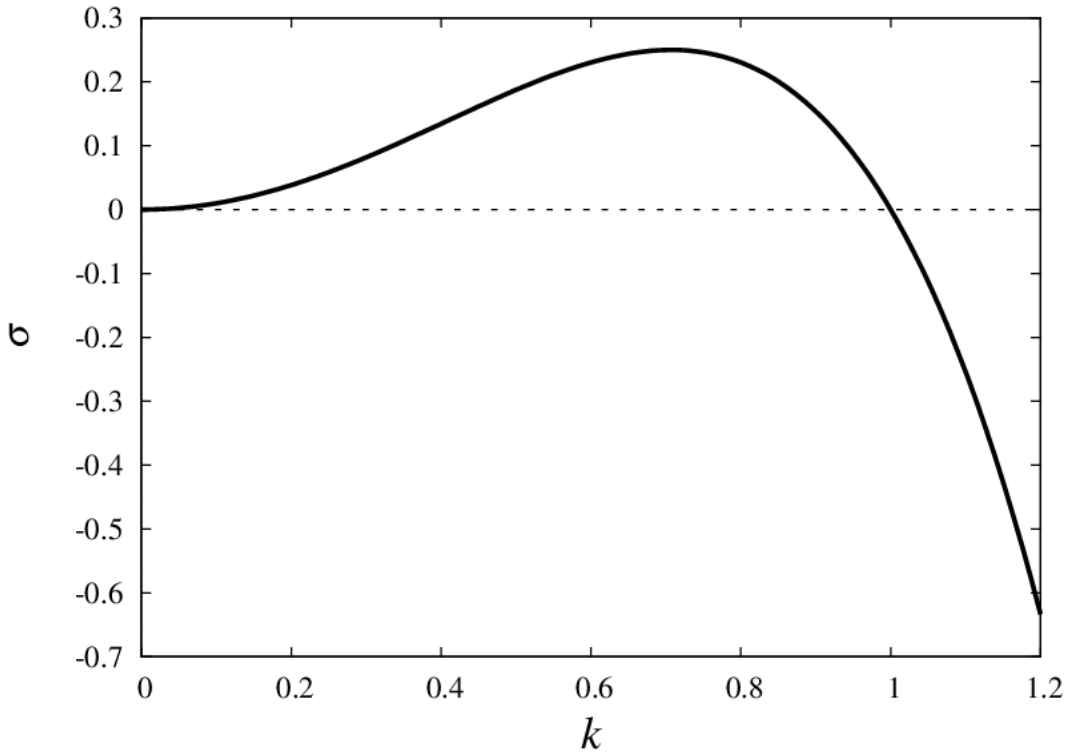

Figure 4.3: Growth rate σ as a function of the wavenumber k. The growth rate σ is negative for $k > 1$. Thus, the flat front will be unstable for $\mathrm{L} > \pi$.

The KS equation exhibits spatiotemporal behavior, such as oscillatory or chaotic solutions [86]. For example, in Fig. 4.4 we show the characteristic period-doubling bifurcations that lead to a chaotic regimen. The transition to chaos takes place as we increase the domain L. Later, we will discuss in detail different solutions for the KS equation.

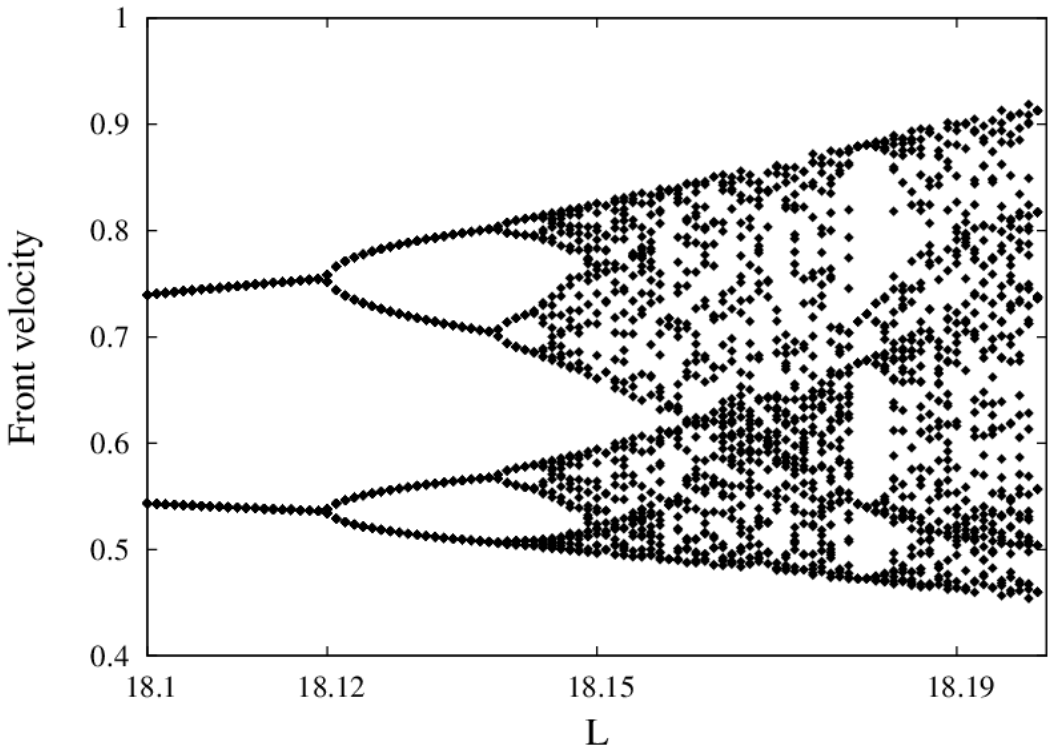

Figure 4.4: Bifurcation diagram showing the relative maximum and minimum of the time evolution of the front velocity. The period-doubling bifurcations increase as we increase the control parameter L.

Previous works have shown that the KS equation can model chemical reaction-diffusion systems [26]. For example, reaction fronts with chemicals having different diffusivities present instabilities that can be described with the KS equation [24,29]. Our goal is to study the effects of fluid motion in the speed, shape and stability of reaction fronts. For this purpose, we modify the KS equation to include fluid flow [47,79,29] as we discuss in Chap. 6.

Chapter 5

Propagating fronts described by the Kuramoto-Sivashinsky equation

Chemical reaction-diffusion fronts exhibiting diffusive instabilities can be modeled using the Kuramoto-Sivashinsky (KS) equation. Diffusive instabilities arise when the diffusivity of the autocatalyst is sufficiently lower than the diffusivity of the reactant [23,29]. Experimental studies of front instabilities carried out with the iodate-arsenous acid reaction in gels to avoid fluid flow showed that the flat front loses stability above a critical ratio of diffusion coefficients between the reactant and autocatalyst, developing cellular structures (periodic spatial structures) similar to those observed in propagating flame fronts [24,87]. Numerical studies of the KS equation revealed a rich variety of spatiotemporal behavior [88,86], such as propagating fronts and cellular structures that resemble the behavior of fronts near diffusive instabilities. In this chapter we will explore the different types of spatio-temporal structures arising in the KS equation as well as their stability. We will find transitions between flat fronts and curved fronts, together with oscillating states in transition to spatio-temporal chaos.

5.1 Equation of motion

We study the propagation of chemical fronts described by the KS equation in two dimensions. The front is confined between two parallel plates located at $X=0$ and $X=\tilde{L}$ as shown in Fig. 5.1. The system allows a flat front that propagates with constant velocity V_0 in a direction parallel to the Z axis. The spatial front profile $H(X,T)$ at time T, measured relative to the flat front, obeys the KS equation:

$$\frac{\partial H}{\partial T}=\nu\frac{\partial^2 H}{\partial X^2}+\frac{V_0}{2}\left(\frac{\partial H}{\partial X}\right)^2-\kappa\frac{\partial^4 H}{\partial X^4}. \qquad (5.1)$$

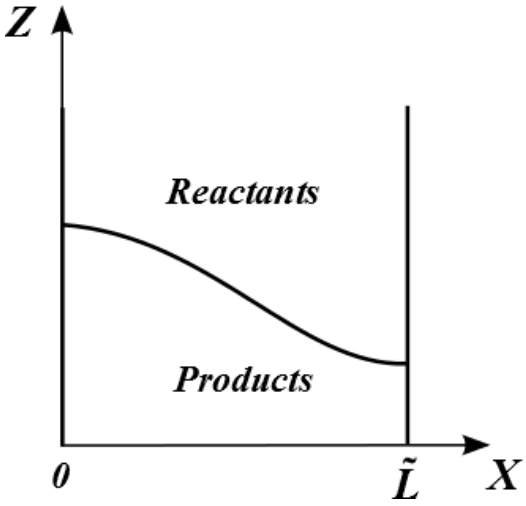

Figure 5.1: Sketch of the propagating front confined between two parallel plates.

We use a reference frame moving at the speed of the flat front (V_0). Therefore the solution $H=0$ represents the flat front moving with constant velocity in the laboratory frame of reference. The coefficients ν and κ depend on the physical characteristics of the system. For example, in the case of an autocatalytic reaction, the parameter ν depends on the ratio of diffusion coefficients between the reactant and the autocatalyst. According to Malevanets *et al.* [29], the flat front presents instabilities if $\nu<0$, given rise to steady stable curved fronts. We will change to a system of dimensionless units by making the substitution $X=L_x x$, $H=L_z h$, and $T=L_T t$, where the lowercase letters indicate dimensionless magnitudes, then the equation transforms into

$$\frac{L_z}{L_T}\frac{\partial h}{\partial t}=\nu\frac{L_z}{L_x^2}\frac{\partial^2 h}{\partial x^2}+\frac{V_0}{2}\frac{L_z^2}{L_x^2}\left(\frac{\partial h}{\partial x}\right)^2-\kappa\frac{L_z}{L_x^4}\frac{\partial^4 h}{\partial x^4}. \tag{5.2}$$

Assuming that κ is non-zero, we choose $L_x=\sqrt{\kappa/|\nu|}$, $L_z=|\nu|/V_0$, and $L_T=\kappa/\nu^2$ as in reference [53] to arrive at

$$\frac{\partial h}{\partial t}=\tilde{\nu}\frac{\partial^2 h}{\partial x^2}+\frac{1}{2}\left(\frac{\partial h}{\partial x}\right)^2-\frac{\partial^4 h}{\partial x^4}. \tag{5.3}$$

Here the x coordinate varies from 0 to L. The dimensionless parameter L is related to the gap between the plates ($\tilde{L}$) by $\mathrm{L}=\tilde{L}/L_x$. We have defined

$\tilde{\nu} = \nu/|\nu|$, hence the value of $\tilde{\nu}$ can be only plus or minus one, depending on the sign of ν. In this thesis we only consider the case $\tilde{\nu} = -1$, which allows for unstable flat fronts and steady stable curved fronts [29]. We impose the boundary conditions at the vertical walls derived by Margolis *et al.* [85] for fronts propagating in a two dimensional channel corresponding to zero first and third partial spatial derivatives of the front height h: $\partial h/\partial x = \partial^3 h/\partial x^3 = 0$. The front height $h(x,t)$ is measured relative to the flat front.

5.2 Stationary solutions

Equation (5.3) exhibits a rich variety of solutions, such as steady fronts that propagate at constant speed, oscillatory and chaotic fronts. In this section we will focus on steady front solutions. Working in a reference frame co-moving with the front, the steady front solutions become stationary. To this end we use a non-linear shooting method to obtain the stationary solutions with their respective propagation velocity for different values of the domain width (L). We then carry out a linear stability analysis to determine the stability of these fronts. We obtained the stationary solutions and their stability using numerical methods described in the following subsections.

5.2.1 Non-linear shooting method

Since we are studying reaction fronts that propagate with constant velocity and constant waveform, we are looking for solutions of the form $h(x,t) = h_0(x) - ct$, where $h_0(x)$ is the spatial front profile and c is the constant velocity of the front. Consequently, the front looks stationary in a reference frame moving at the constant front velocity c, with $h_0(x)$ being the spatial front profile in this reference frame. With this substitution Eq. (5.3) becomes

$$-c = -\frac{d^2 h_0}{dx^2} + \frac{1}{2}\left(\frac{dh_0}{dx}\right)^2 - \frac{d^4 h_0}{dx^4}. \tag{5.4}$$

Since the derivative of a constant is zero, any constant may be added to the solution $h_0(x)$ and it will still be a solution. We choose the constant to make the

average position of the front equal to zero. One of these solutions corresponds to a stationary flat front solution of zero height.

We find a solution of Eq. (5.4) using a nonlinear shooting method [89]. We transform Eq. (5.4) into a set of four coupled first-order ordinary differential equations (ODEs) by defining each high order derivative as a new variable [90]. The differential equations are

$$\begin{cases} u = \dfrac{dh_0}{dx} \\ v = \dfrac{du}{dx} \\ w = \dfrac{dv}{dx} \\ \dfrac{dw}{dx} = c - v + \dfrac{1}{2}u^2 \end{cases} \tag{5.5}$$

We start the shooting method at $x = 0$. Since the value of $h_0(x)$ is arbitrary, we have two free parameters to start the shooting method: the speed c and the second derivative d^2h_0/dx^2. Given guessing values to these parameters, we are able to integrate the equations with a simple Euler method in order to reach the other boundary at $x = \mathrm{L}$. We then adjust the parameters to obtain the correct boundary conditions at $x = \mathrm{L}$. We used 10^5 points with the Euler method in this interval; a similar calculation using a fourth-order Runge-Kutta method did not yield a significant difference. Finally, we adjust the value of $h_0(x)$ at $x = 0$ to make the average position of the front equal to zero.

5.2.2 Linear stability analysis

We analyze the stability of chemical fronts by introducing small perturbations to the stationary-state solutions. Let $h_1(x,t)$ be a small perturbation of the stationary state $h_0(x)$. We have

$$h(x,t) = h_0(x) + h_1(x,t). \tag{5.6}$$

Substituting this into Eq. (5.3), we obtain

$$\frac{\partial h_1}{\partial t} = -\frac{\partial^2 h_1}{\partial x^2} + \frac{1}{2}\left(\frac{\partial h_1}{\partial x}\right)^2 + \left(\frac{\partial h_0}{\partial x}\right)\left(\frac{\partial h_1}{\partial x}\right) - \frac{\partial^4 h_1}{\partial x^4}. \tag{5.7}$$

Keeping only the linear terms on h_1, Eq. (5.7) becomes

$$\frac{\partial h_1}{\partial t} = -\frac{\partial^2 h_1}{\partial x^2} + \left(\frac{\partial h_0}{\partial x}\right)\left(\frac{\partial h_1}{\partial x}\right) - \frac{\partial^4 h_1}{\partial x^4}. \tag{5.8}$$

We look for solutions of the form

$$h_1(x,t) = e^{\sigma t}\tilde{h}(x), \tag{5.9}$$

where σ is the growth rate of the perturbation. With this form of the perturbation we can determine the stability of the stationary state h_0 since solutions with a negative real part of σ will decay with time. With this substitution, Eq. (5.8) becomes an eigenvalue equation, with σ the eigenvalue and $\tilde{h}(x)$ the eigenfunction

$$\sigma\tilde{h} = -\frac{d^2\tilde{h}}{dx^2} + \left(\frac{dh_0}{dx}\right)\left(\frac{d\tilde{h}}{dx}\right) - \frac{d^4\tilde{h}}{dx^4}. \tag{5.10}$$

We solve Eq. (5.10) using a shooting method similar to the one described in Sec. 5.2.1. We first transform the partial differential equation into a set of first-order ODEs. However, in this case, the system of ODEs is linear. This fact simplifies our work which is to determine the eigenvalue σ. The differential equations are

$$\begin{cases} y_1 = \dfrac{d\tilde{h}}{dx} \\ y_2 = \dfrac{dy_1}{dx} \\ y_3 = \dfrac{dy_2}{dx} \\ \dfrac{dy_3}{dx} = -\sigma\tilde{h} - y_2 + y_1\left(\dfrac{dh_0}{dx}\right) \end{cases} \tag{5.11}$$

The free parameters in this case are $\tilde{h}$ and $d^2\tilde{h}/dx^2$ at the starting point $x = 0$, and σ. Guessing some initial values to these parameters, we are able to

integrate the equations with a simple Euler method, reaching the boundary at $x = \mathrm{L}$. After that, we adjust the parameters and repeat the process until we obtain the correct boundary conditions at $x = \mathrm{L}$. In other words, the shooting method aims at finding the initial values at $x = 0$ that lead to the correct boundary conditions at $x = \mathrm{L}$. However, due to the fact that the system of ODEs is linear, we can generate two linearly independent solutions. Consequently, any solution that satisfies the boundary conditions at $x = \mathrm{L}$ is a linear combination of these two solutions. This leads to a linear system of two equations. The eigenvalue σ will make the determinant of this system equal to zero. To generate the first linearly independent solution, we start the shooting method at $x = 0$ with $\tilde{h} = 1$ and $d^2\tilde{h}/dx^2 = 0$; the second one is generated with $\tilde{h} = 0$ and $d^2\tilde{h}/dx^2 = 1$. The eigenvalue equation [Eq. (5.10)] allows for an infinite number of complex eigenvalues. The front will be stable if all of the eigenvalues have a negative real part. Therefore, if the eigenvalue with the largest real part is negative, the front is stable.

5.3 Results

We obtain stationary front solutions of the KS equation for different values of the slab width L. Since the solution depends on an arbitrary constant, we choose this constant to match the average front height equal to zero. The front height is measured relative to the average front height. We determine the stability of the fronts by calculating the growth rates σ for small perturbations.

5.3.1 Spatial front profiles

In order to describe the spatial front profile we define the axis as a line parallel to the z axis passing through the center of the two-dimensional domain at $x = \mathrm{L}/2$. Thus, the fronts can be flat, axisymmetric, or nonaxisymmetric with respect to the axis. In Fig. 5.2 we show four different front profiles, with the front height function measured relative to the average front height. We show cases where $\mathrm{L} > \pi$, since for these values the flat front presents instabilities [Eq. (4.33)] as we will discuss later. For $\mathrm{L} = 4$, a nonaxisymmetric front

develops (Fig. 5.2a). This front has one side higher than the other side. For $L = 8$, the front is axisymmetric, with a single maximum on the axis (Fig. 5.2b), while for $L = 8.5$ the front is nonaxisymmetric, having a single minimum (Fig. 5.2c). For $L = 9.5$ the front is also nonaxisymmetric, having three inflection points (Fig. 5.2d). The flat front is also a solution for these values of L. All these fronts have steady shape, each moving at different constant velocities.

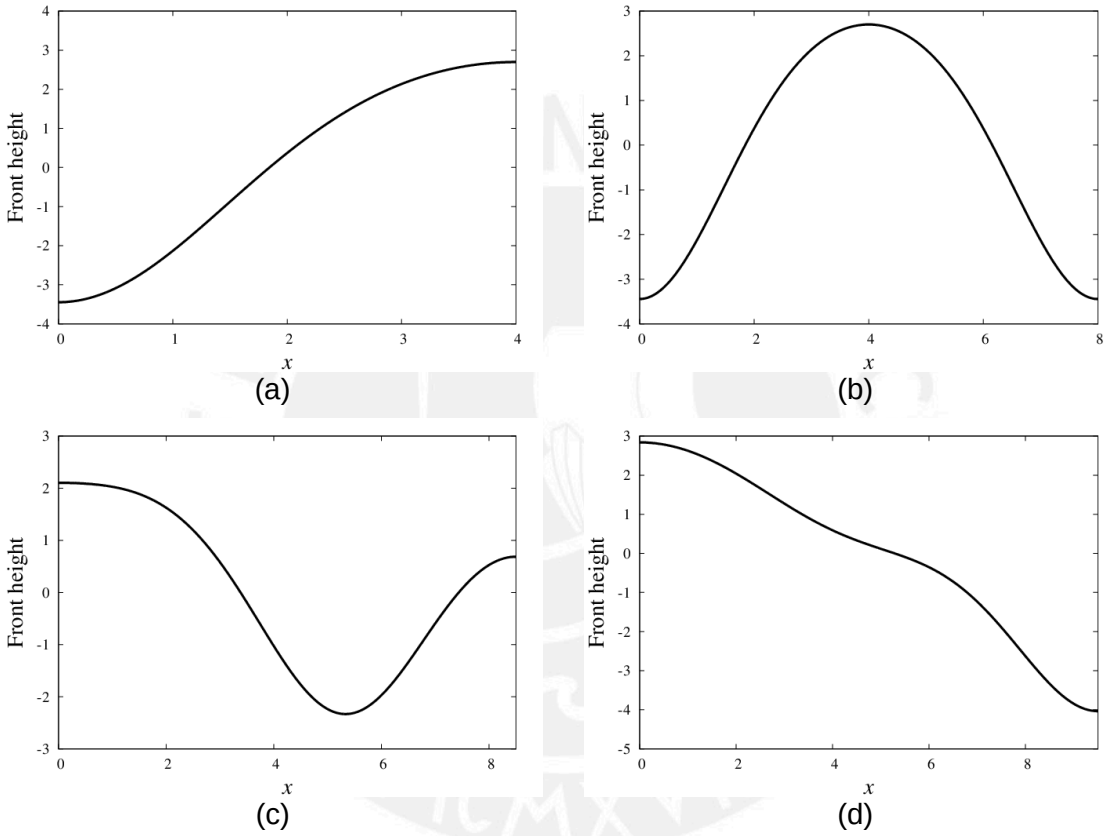

Figure 5.2: Different front profiles. The front height is measured from the average front height. (a) Nonaxisymmetric front having an inflection point ($L = 4$). (b) Axisymmetric front having a relative maximum ($L = 8.0$). (c) Nonaxisymmetric front having a relative minimum ($L = 8.5$). (d) Nonaxisymmetric front having three inflection points ($L = 9.5$).

Since the equations are nonlinear, more than one solution may appear, we show this for the case with $L = 9$. These fronts are shown in Fig. 5.3. The flat front (A) is indeed a solution for each value of L. We also find the nonaxisymmetric solutions (B and C), being C a reflection of B about the central axis. Indeed, the symmetry of Eq. (5.4) implies that the reflection of a

nonaxisymmetric solution about the central axis is also a solution with the same velocity. The concave upward solution (D) and the concave downward solution (E) are axisymmetric. Therefore, given a slab width, steady fronts of different spatial profiles can be developed. We will analyze the stability of the fronts in the following section.

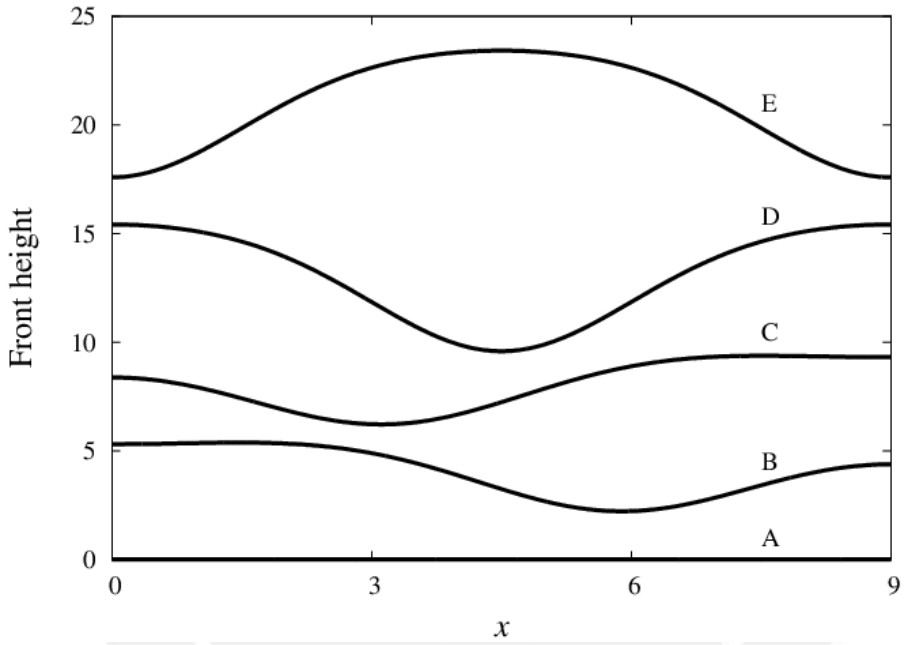

Figure 5.3: Different front profiles for $L = 9$. The zero height solution corresponds to flat front (A). Lines B and C correspond to nonaxisymmetric solutions, while lines D and E correspond to axisymmetric solutions. The fronts are shifted for comparison.

5.3.2 Regions of stability

In the previous section we obtain stationary fronts with different shapes, in a reference frame co-moving with the front, for different values of the domain width L. Now, we are interested in determine the front velocities for different values of the slab width L in the absence of an external fluid flow [91,92]. The growth rate for small perturbations σ determines the stability of each front. Figure 5.4 shows the velocities of several fronts relative to the velocity of the flat front for different values of L. In this figure, the flat front solution has a velocity

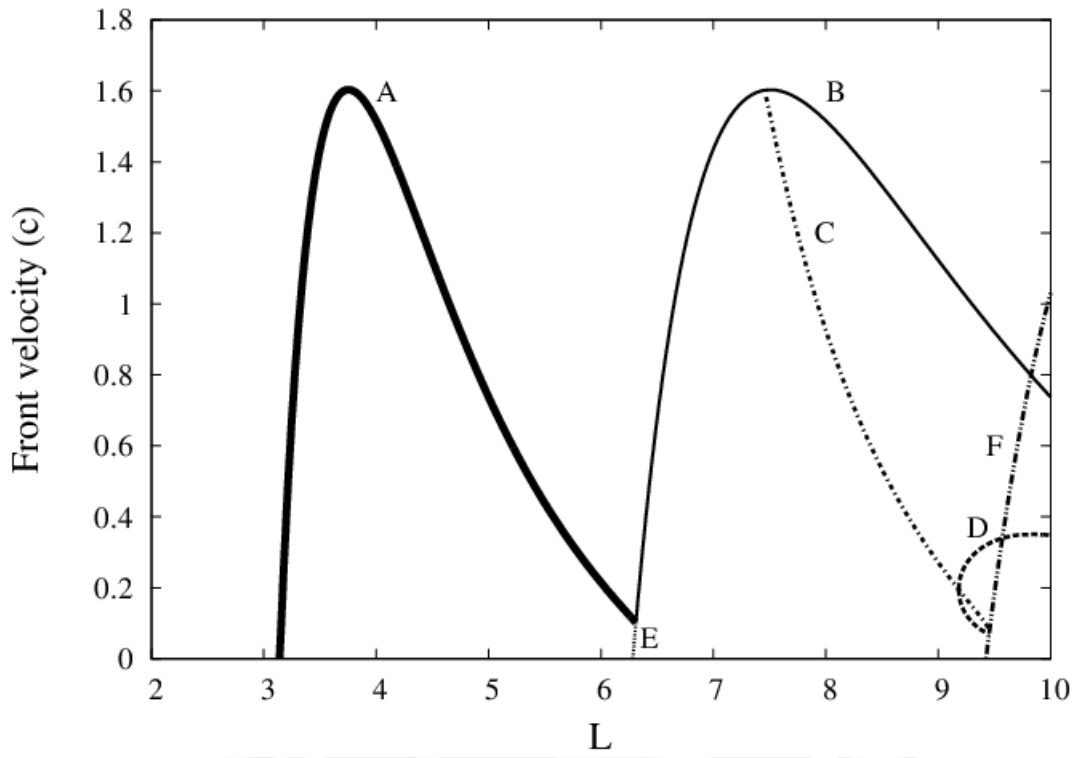

Figure 5.4: Front velocities for different distances between plates (L). The thick solid line (A) corresponds to stable nonaxisymmetric fronts. The solid line (B) corresponds to stable axisymmetric fronts. The dashed line (E) corresponds to unstable axisymmetric fronts. Broken lines (C, D, and F) correspond to unstable nonaxisymmetric fronts.

equal to zero, being a solution for all values of L. The stability of the flat front solution provides an analytical dispersion relation [Eq. (4.32)] between growth rates (σ) and perturbation wavenumbers (π/L) given by $\sigma = (\pi/\mathrm{L})^2 - (\pi/\mathrm{L})^4$, having critical stability ($\sigma = 0$) for $\mathrm{L} = \pi$. When we increase L above π, new stable nonaxisymmetric solutions appear. These solutions have a side near one boundary higher than the other, with their velocities shown in Fig. 5.4 by branch A. Because of the symmetry of the equation, the reflection about the axis is also a solution with the same velocity. In branch A, the front speed increases with increasing L until it reaches a maximum speed of 1.60 at L = 3.75, it then decreases until it meets branches B and E. Branch E corresponds to unstable axisymmetric solutions in the interval $6.28 < \mathrm{L} < 6.31$. In this range it coexists with branch A. As we increase the width L beyond 6.31, branch A disappears and new stable axisymmetric solutions appear (branch B). In branch B the front speed increases until it reaches a maximum speed, decreasing after this

maximum. Branch B contains two solutions with the same velocity: one is concave downward (having a maximum); the other, concave upward (having a minimum). The concave downward solution is always stable in the domain ($L > 6.31$), we discuss the stability of the other solution later. Axisymmetric fronts in branch B correspond to two mirrored nonaxisymmetric solutions; consequently, their maximum speed is the same as the maximum speed of nonaxisymmetric fronts. However, the fronts are not necessarily stable. We find other unstable nonaxisymmetric solutions with velocities described by branches C, D, and F. Branch C begins near the maximum of branch B, its velocity decreasing with increasing width L, continuing until it meets branches D and F at a single point ($L = 9.46$). For larger values of L, branch D shows higher velocities. In the range $9.18 \leq L \leq 9.46$ branch D has solutions with two different velocities for each value of L. Branch F meets the branch of flat fronts, having higher velocities with increasing L. We are interested in determining how these front velocities change when an external fluid flow is applied.

We obtain the largest real part of the growth rate [Re(σ)] for front perturbations (Fig. 5.5). These values of [Re(σ)] determine the stability of the solutions: positive values of [Re(σ)] indicate an unstable front. For small values of L, the only solution is the flat front solution (branch G) having Re(σ) negative. As we increase the width L, we find that Re(σ) becomes positive for $L > \pi$, indicating a transition to unstable fronts. As we increase the width L further, the real part of the growth rate reaches a maximum, remaining positive for all values of L under consideration. Branch A in Fig. 5.5 corresponds to growth rates associated with the nonaxisymmetric solutions described in Fig. 5.4. All these values are negative, indicating stability of the nonaxisymmetric fronts. We notice that branch A has a minimum value near $L = 4.60$, where we find a discontinuity in the slopes. This discontinuity is due to the existence of more than one eigenvalue for each solution. As we increase L, the highest growth rate decreases, while the second largest increases. They meet at the place where the slope presents a discontinuity. Branches B_1 and B_2 correspond to two axisymmetric solutions having the same propagation velocities. One of these

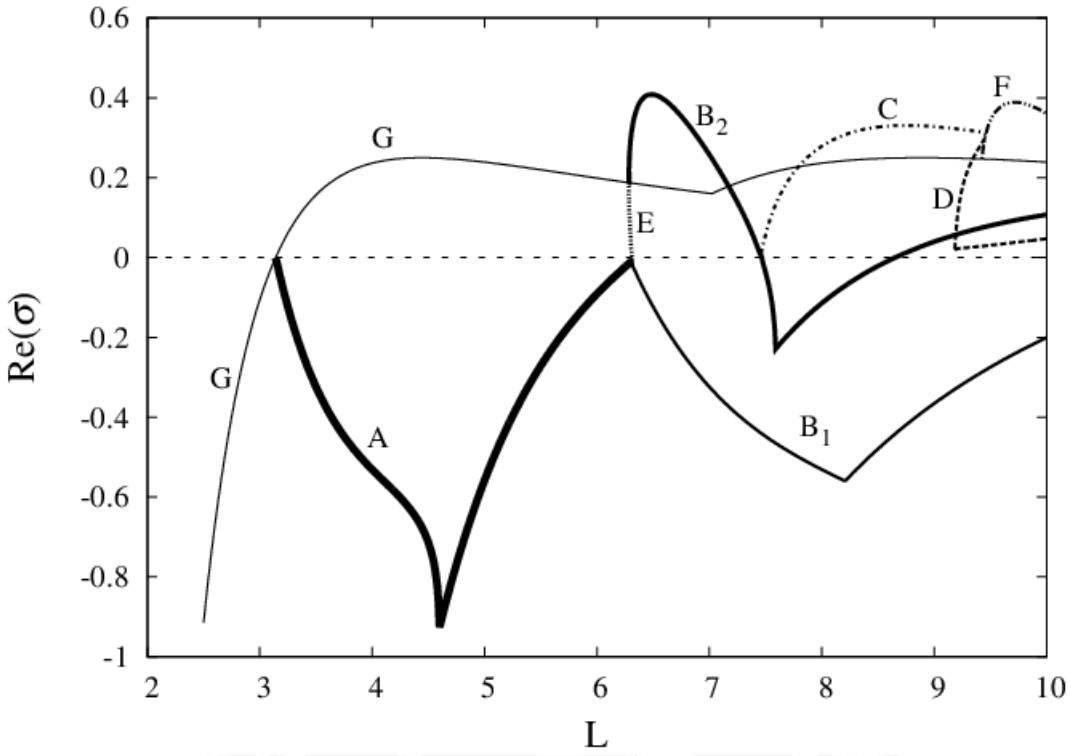

Figure 5.5: The largest real part of the eigenvalues σ for different distances L between plates. The front is unstable when the largest real part of the eigenvalues σ is positive. The thickest solid line (A) corresponds to nonaxisymmetric fronts. Solid line B_1 corresponds to axisymmetric fronts and solid line B_2 corresponds to other axisymmetric fronts. Broken lines (C, D, and F) correspond to nonaxisymmetric fronts. The dashed line (E) corresponds to other axisymmetric fronts. Solid line G corresponds to flat fronts.

solutions corresponds to concave downward fronts represented by line B_1; the other corresponds to concave upward fronts represented by line B_2. The growth rates indicate that the concave upward fronts are stable (B_1), while the concave downward fronts are unstable, except in the interval $7.47 < L < 8.65$. This interval is a region of bistability for both types of axisymmetric fronts. These branches also present minima with abrupt changes of slope, similar to the one exhibit by branch A. Branch E corresponds to two distinct unstable axisymmetric fronts having the same velocity. Branches C, D, and F show real parts of growth rates corresponding to nonaxisymmetric solutions. Their values are greater than zero, therefore these fronts are unstable. For all values of L in Fig. 5.5, we find at least one stable steady front. These stable solutions change from flat, to nonaxisymmetric, and then to axisymmetric as we increase L.

5.3.3 Cellular structures

For larger values of L, we find solutions that can be constructed using fronts developed in smaller cells [91,92,93]. In this case a larger pattern can be formed by placing the cell solutions side by side. For example, in Fig. 5.6 we show four front profiles. Two of them correspond to nonaxisymmetric fronts obtained with $L = 3.5$ (Fig. 5.6a and Fig. 5.6b), while the others correspond to axisymmetric fronts obtained with $L = 7.0$ (Fig. 5.6c and Fig. 5.6d). The

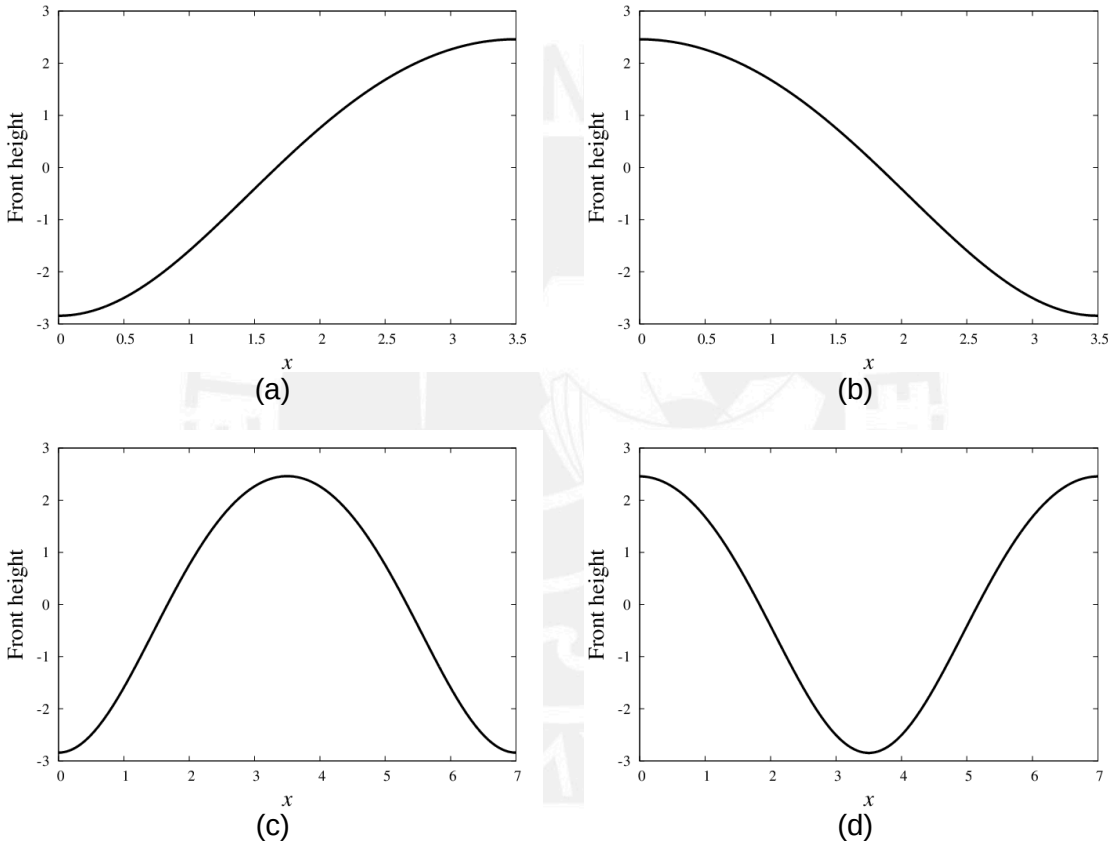

Figure 5.6: Front profiles for $L = 3.5$ and $L = 7.0$. The front height is measured from the average front height. (a) Nonaxisymmetric front obtained with $L = 3.5$. (b) Another axisymmetric front obtained with $L = 3.5$. (c) Axisymmetric front obtained with $L = 7.0$. (d) Another nonaxisymmetric front obtained with obtained with $L = 7.0$.

axisymmetric pattern of Fig. 5.6c corresponds to two nonaxisymmetric patterns formed with $L = 3.5$. Similarly, a concave upward axisymmetric pattern (Fig. 5.6d) can also be formed with these two nonaxisymmetric patterns obtained with $L = 3.5$. It is worth pointing out that the front of Fig. 5.6d is not a

reflection of the front of Fig. 5.6c about the average front height. As a consequence, both axisymmetric patterns with $L = 7.0$ share the same propagating speed, but not necessarily the same conditions of stability.

In Fig. 5.7 we show the velocities corresponding to cellular patterns and their respective stabilities. Branches A, C and E correspond to nonaxisymmetric solutions, whereas branches B and D correspond to axisymmetric solutions. Solid lines correspond to stable fronts, while broken lines correspond to unstable fronts. The axisymmetric solutions of branch B correspond to two mirrored nonaxisymmetric solutions of branch A; the solutions of branch C correspond to joining solutions of branches A and B, forming an undulating curve; the solutions of branch D correspond to joining solutions of branches A and C, forming an undulating curve; and so on. Consequently, the maximum speed for each branch is the same, being located at a width equal to $n \times L_1$, where $L_1 = 3.75$ is the location of the speed maximum for the smallest cell, n is an integer. Nonaxisymmetric stable solutions associated with branch A appear for $L > \pi$, where flat front solutions become unstable. Concave upward and concave downward axisymmetric fronts are represented by branch B sharing a region of bistability. However, the region of stability of the concave downward axisymmetric fronts is greater than the concave upward fronts. This region is represented by a solid line in branch B, which breaks for $L > 11.42$ indicating transition to unstable solution. Branch D also contains two solutions with the same velocity. These axisymmetric solutions have a maximum or minimum in the central axis. They are unstable except for the interval $14.97 < L < 16.84$, which is also a region of bistability for these axisymmetric fronts. The nonaxisymmetric solutions associated with branches A, C, and E, also have two solutions with the same velocity for each value of L in their respective domain. However, one of these solutions is the reflection of the other about the central axis, because of the symmetry of Eq. (5.4). Consequently, these nonaxisymmetric branches have the same values of $\mathrm{Re}(\sigma)$, the real parts of their growth rates. We found that although the speeds of the cellular patterns are determined by the speed of the smallest cell, they do not share the same conditions of stability.

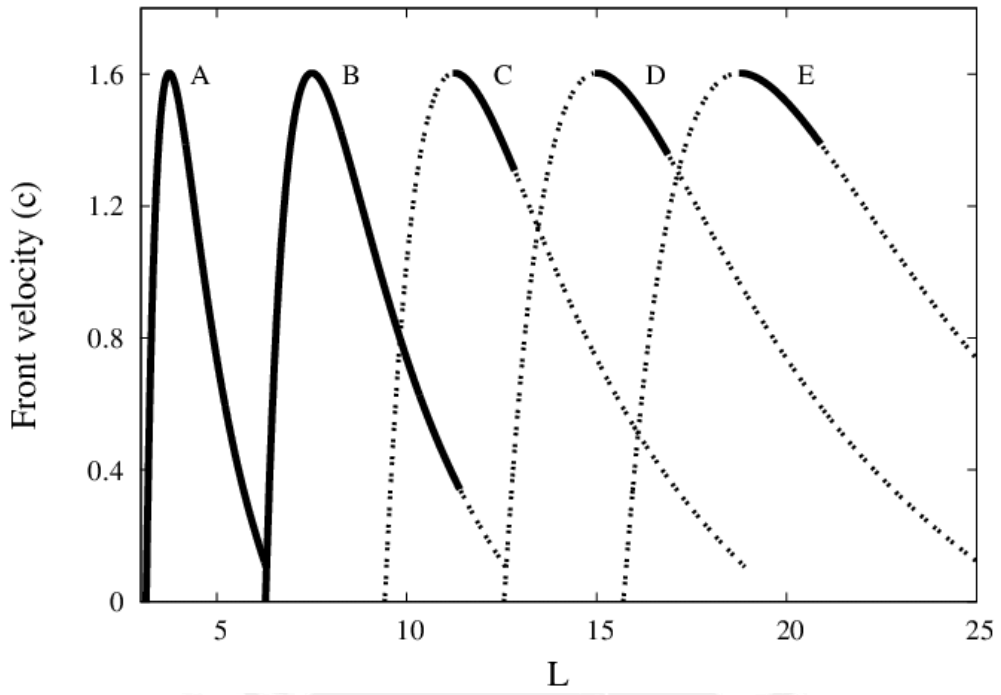

Figure 5.7: Front velocities for different distances between plates (L). Solid lines correspond to stable fronts; broken lines correspond to unstable fronts. Lines A, C and E correspond to distinct nonaxisymmetric fronts, whereas lines B and D correspond to distinct axisymmetric fronts.

We studied reaction fronts within a two-dimensional slab using the KS equation. The flat front loses stability as we increase the slab width L, leading first to a stable nonaxisymmetric front, and later to a stable axisymmetric front. In other words, these transitions can take place by changing the slab width L. We found stable axisymmetric fronts, having a maximum at the center of the slab (concave downward fronts) or a minimum (concave upward fronts). The concave upward and concave downward axisymmetric fronts share a small region of bistability. In addition, we studied the stability of extended patterns for larger values of the slab width L. We found that the speed of the smallest cell determines the speed of the cellular patterns. However, the cellular patterns presented different conditions of stability.

Chapter 6

Kuramoto-Sivashinsky fronts advected by a Poiseuille flow

Reaction fronts modeled with the KS equation can be modified by the presence of fluid flow, as in the case of chemical fronts in the iodate-arsenous acid reaction propagating inside vertical tubes [94]. In these fronts, density gradients generate convective fluid motion that determines the structure of the front. Chemical reaction fronts in Hele-Shaw cells also exhibit complex behavior due to the coupling with fluid flow [53]. In this chapter we consider the effects of fluid flow on steady fronts described by the KS equation as they are advected by a Poiseuille flow.

We consider a two-dimensional slab confined by two infinite plates as shown in Fig 5.1. A viscous fluid flow is applied between the plates along the Z direction. The flow is sustained by an externally applied pressure gradient in the Z-direction. In this geometry the pressure varies linearly along the Z-direction, so the velocity profile becomes parabolic (see Sec. 3.1). Working with our system of dimensionless units defined in Sec. 5.1 and using a reference frame moving at the speed of the flat front, the KS equation is given by Eq. (5.3). In this equation, we use lowercase letters for the corresponding variables in our system of dimensionless units. In addition, L is the dimensionless parameter corresponding to $\tilde{L}$. Hence, the x coordinate in Eq. (5.3) varies from 0 to L. Using Eq. (3.6) and Eq. (3.7) the parabolic velocity profile is given by

$$v_z(x,t) = \frac{6\bar{\mathrm{v}}}{\mathrm{L}^2}(\mathrm{L}-x)x. \tag{6.1}$$

Here $\bar{\mathrm{v}}$ is the average velocity of the flow measured in our system of dimensionless units. The position of the front at time t is described by the front height $h(x,t)$ above the x axis. The time evolution of the front is provided by Eq. (5.3) with the addition of the flow velocity [47],

$$\frac{\partial h}{\partial t} = -\frac{\partial^2 h}{\partial x^2} + \frac{1}{2}\left(\frac{\partial h}{\partial x}\right)^2 - \frac{\partial^4 h}{\partial x^4} + v_z. \tag{6.2}$$

Here we set $\tilde{v} = -1$, which allows for flat front instabilities as mentioned in Sec. 5.1. Because of the geometry, we still have the same boundary conditions for fronts propagating in a channel [85]: $\partial h/\partial x = \partial^3 h/\partial x^3 = 0$.

We also look for stationary solutions in our reference frame that moves with the velocity of the front (c). Therefore we can set the solutions as $h(x,t) = h_0(x) - ct$, where $h_0(x)$ corresponds to the spatial front profile. We also consider that the average position of the spatial front profile is zero in our reference frame. With this substitution Eq. (6.2) becomes

$$-c = -\frac{d^2 h_0}{dx^2} + \frac{1}{2}\left(\frac{dh_0}{dx}\right)^2 - \frac{d^4 h_0}{dx^4} + v_z. \tag{6.3}$$

We use the shooting method to solve Eq. (6.3). The $h_0(x)$ solution corresponds to the reaction front under a Poiseuille flow. The reaction fronts move along $+z$ direction in the absence of Poiseuille flow. A supportive flow is an external fluid flow that moves in the same direction of these reaction fronts without fluid flow. In other words, the flow moves along $+z$ direction "pushing" the reaction fronts. An adverse flow moves in the opposite direction. A linear stability analysis leads us to the eigenvalue equation [Eq. (5.10)], where the growth rate σ will determine the stability of the fronts.

6.1 The effect of a supportive Poiseuille flow

We first obtain stationary stable fronts for different average velocities of the supportive Poiseuille flow while keeping the slab width constant. The slab width is set to $\mathrm{L} = 3$ since at this width there is a stable flat front solution propagating in the $+z$ direction in the absence of Poiseuille flow. Figure 6.1 shows some of these stable stationary states for different average velocities of the supportive Poiseuille flow. The fronts are concave downward, with a single maximum on the axis (a line parallel to the z axis and passing through the center of the two-

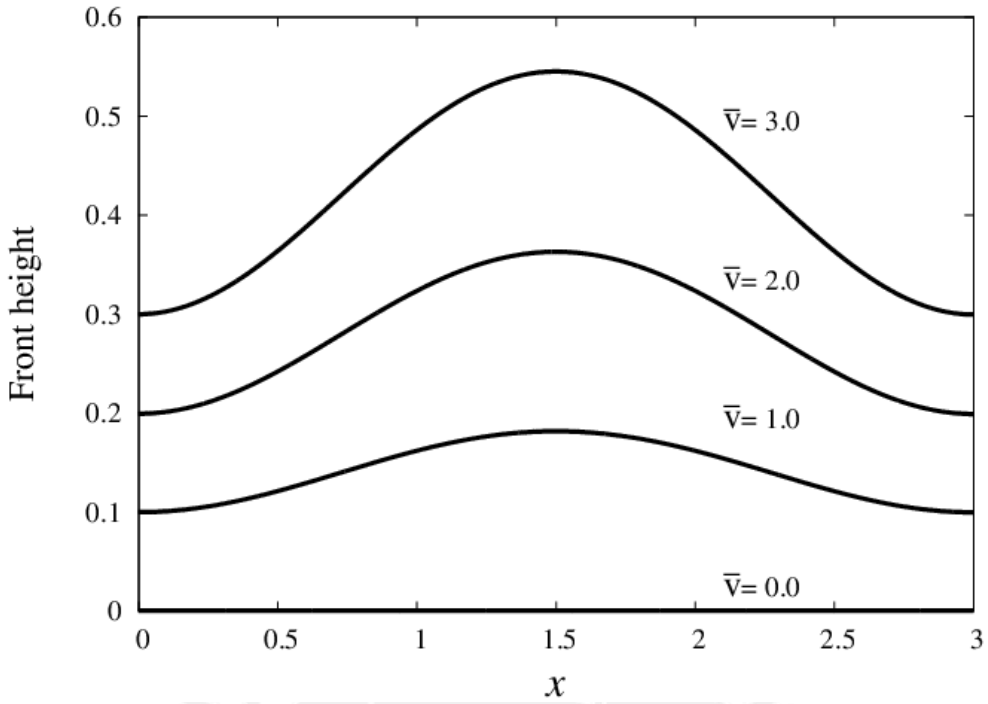

Figure 6.1: Front profiles for different average velocities of the supportive Poiseuille flow. For supportive flows the fronts are axisymmetric. The fronts are shifted for comparison.

dimensional domain). As we increase the average speed of the supportive Poiseuille flow ($\bar{v}$), the maximum front height measured with respect to the average height of the front also increases. Therefore, adding a supportive Poiseuille flow to flat fronts results in stable concave downward fronts for $L = 3$.

We apply a small supportive Poiseuille flow to study the effects on the velocities of the fronts. Figure 6.2 shows the front velocities with a supportive flow with $\bar{v} = 0.1$ for different values of the domain width L. The original flat front without Poiseuille flow (see Fig. 5.4) becomes axisymmetric. The transition from these axisymmetric fronts to nonaxisymmetric fronts occurs at $L = 3.15$, whereas this transition without Poiseuille flow occurs at $L = \pi$ (see Fig. 5.4). The difference between these transition points is certainly small in this case. For larger values of L, the unstable front becomes part of branch B_1 corresponding to concave downward fronts. As these fronts lose stability, stable nonaxisymmetric fronts appear (Branch A). The velocities in this branch

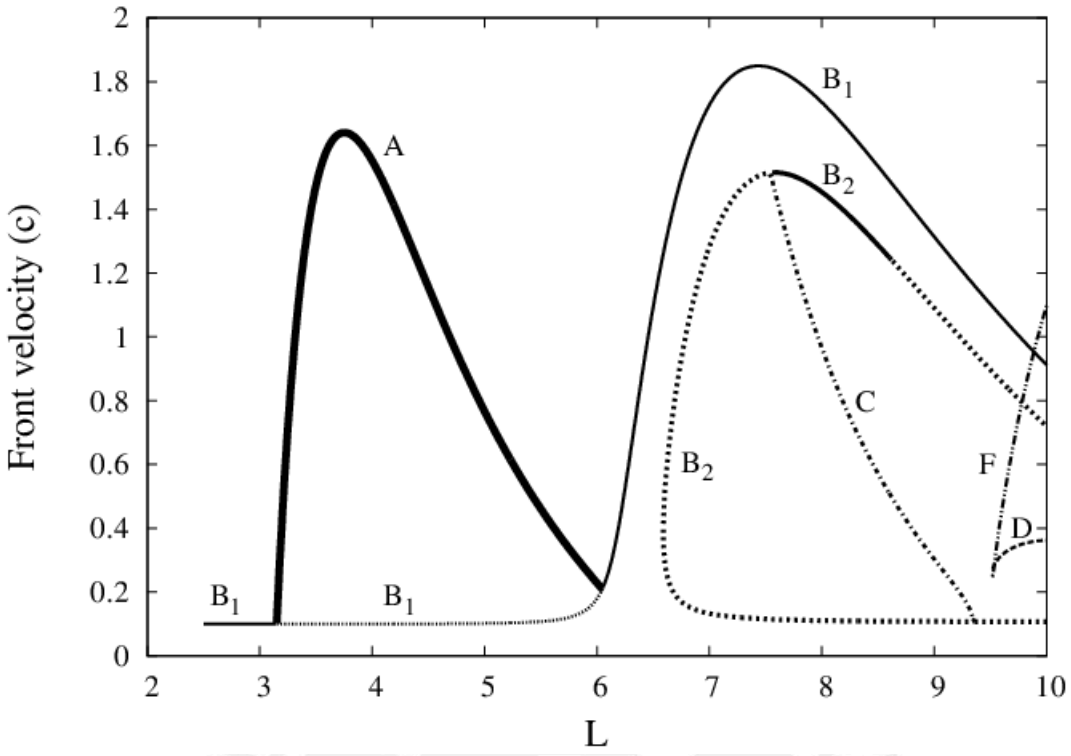

Figure 6.2: Front velocities subject to a Poiseuille flow in the same direction as the propagating front. The average velocity of the flow is $\bar{v} = 0.1$. Solid lines correspond to stable fronts; all broken lines correspond to unstable fronts. The thick solid line (A) corresponds to nonaxisymmetric fronts. Branch B_1 corresponds to axisymmetric fronts. Branch B_2 corresponds to other axisymmetric fronts. Broken lines (C, D, and F) correspond to nonaxisymmetric fronts.

increase as they reach a maximum at $L = 3.75$, with the branch ending at $L = 6.04$, where branch A meets branch B_1. This branch (B_1) corresponds to concave downward fronts with increasing speeds until they reach a maximum speed at $L = 7.44$. The maximum speed for axisymmetric fronts in branch B_1 is higher than the maximum speed for branch A, therefore supportive Poiseuille flows favour axisymmetric fronts. Branch B_2 consists of axisymmetric fronts but concave upward. Without Poiseuille flow (see Fig. 5.4), branches B_1 and B_2 exhibit the same velocities, but with Poiseuille flow they separate. Most of branch B_2 is unstable, except for a small region of bistability with fronts in branch B_1. Fronts that were previously flat (see Fig. 5.4) appear here as part of branch B_2. Branches C, D, and F correspond to unstable nonaxisymmetric fronts. Branch C originates where fronts on branch B_2 become stable, with their

velocities decreasing until the branch joins the lower portion of branch B_2. Branches D and F start at the same point at $L = 9.51$, increasing their velocities. Branch D initially has higher velocities, but there is a crossover with branch F at $L = 9.53$ forming a very small loop in Fig. 6.2. In summary, adding a supportive Poiseuille flow changes the speeds of stable fronts. Speeds decrease for concave upward fronts, increase slightly for stable nonaxisymmetric fronts, and show a much higher increase for concave downward fronts.

We calculate the growth rate σ from Eq. (5.10) to determine the stability of the fronts whose velocities are shown in Fig. 6.2. We show in Fig. 6.3 the largest real part of the growth rate for a supportive flow ($\bar{v} = 0.1$). Adding Poiseuille flow to flat fronts results in stable concave downward fronts for $L < 3.15$, as shown by the negative values of $\mathrm{Re}(\sigma)$. We observe a transition to positive values at $L = 3.15$, where branch A appears. Branch A, which is related to stable nonaxisymmetric fronts, has a slope discontinuity at its minimum value. The concave downward axisymmetric fronts (B_1) are unstable in the interval $3.15 < L < 6.04$. The concave upward fronts B_2 are now disconnected from branch B_1 in contrast to the case without Poiseuille flow (see Fig. 5.5). They are stable in the interval $7.56 < L < 8.62$, where we have a region of bistability between two types of axisymmetric fronts. The size of this region is 10% shorter than that of the one obtained in the absence of Poiseuille flow (see Fig. 5.5). The original flat fronts without Poiseuille flow have joined branch B_2 for larger values of L, becoming concave upward fronts. Branch C begins where branch B_2 becomes negative, with no connection to branches F and D. Applying Poiseuille flow results in higher growth rates for branches F and D. The presence of a supportive flow increases the region of stability for concave downward fronts, providing them with lower negative values for $\mathrm{Re}(\sigma)$.

Increasing the average speed of a supportive Poiseuille flow favours the formation of axisymmetric fronts as shown in Fig. 6.4. In this figure we display the velocity of stable fronts as a function of the slab width. In the absence of Poiseuille flow ($\bar{v} = 0$), the curve has two local maxima, one of them located between two points where the slope changes abruptly. The widths between these two points allow for stable nonaxisymmetric fronts, with the fronts being

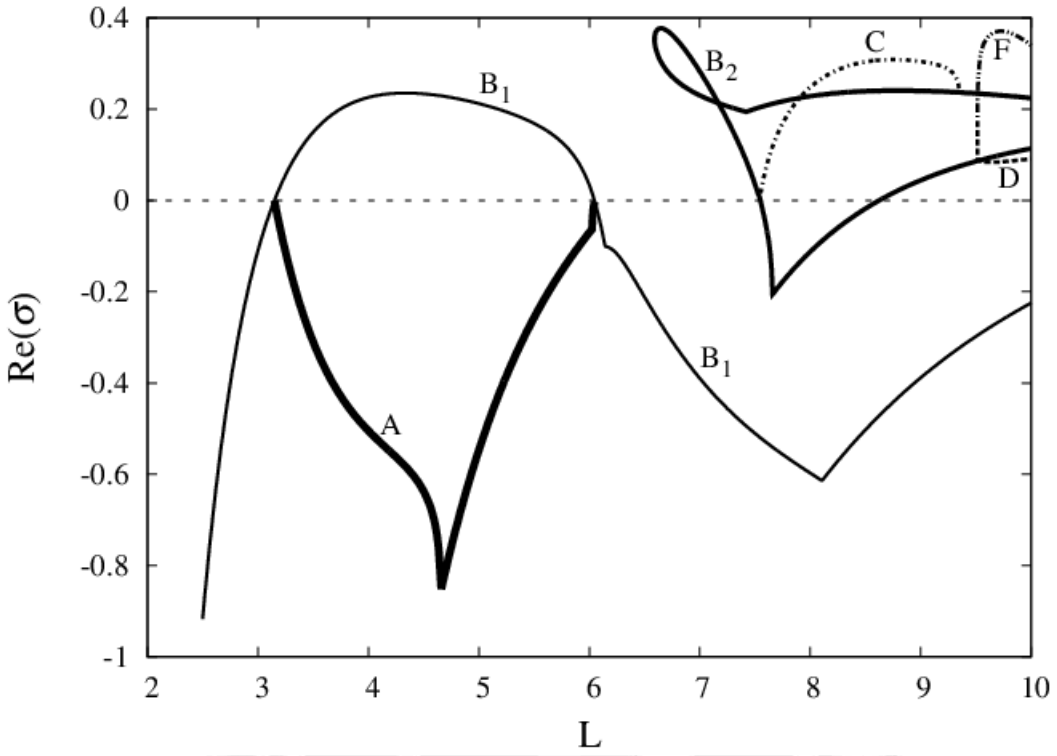

Figure 6.3: The largest real part of the eigenvalues σ for different distances L between plates. The Poiseuille flow is in the same direction as the propagating front. The average velocity of the flow is $\bar{v} = 0.1$. The front is unstable when the largest real part of the eigenvalues σ is positive. The thickest solid line (A) corresponds to nonaxisymmetric fronts. Solid line B_1 corresponds to axisymmetric fronts. Solid line B_2 corresponds to other axisymmetric fronts. Broken lines (C, D, and F) correspond to nonaxisymmetric fronts.

axisymmetric elsewhere. The value of the speed at each maximum is the same, with the maximum on the left corresponding to a stable nonaxisymmetric front. The other maximum corresponds to a stable axisymmetric front. In this case the transition points between stable axisymmetric and nonaxisymmetric fronts are located at $L = \pi$ and $L = 6.31$. By introducing a small supportive flow, we notice that the speeds of all fronts increase: the curve corresponding to $\bar{v} = 1.0$ is completely above the curve for $\bar{v} = 0$. However, the maximum speed for axisymmetric fronts is now higher than the one for nonaxisymmetric fronts. We also notice that the locations of the transition points are changed. Increasing the average flow speed reduces the region where stable nonaxisymmetric fronts are present. As the average speed is increased further, the transitions points

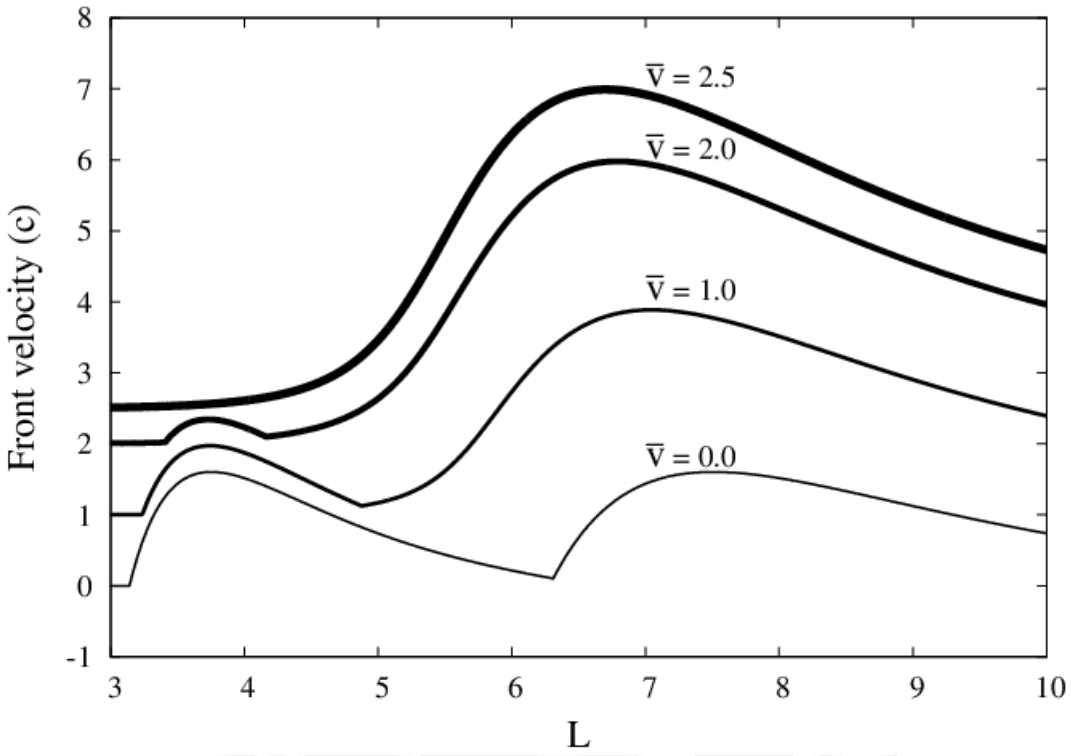

Figure 6.4: Front velocities as a function of the distance L between plates for different supportive Poiseuille flows. All fronts propagate in the same direction as the Poiseuille flow. The average flow speed ($\overline{v}$) affects the shape of the fronts. For $\overline{v} = 0$ the curve has two maxima. The first one corresponds to stable nonaxisymmetric fronts; the second corresponds to axisymmetric fronts. As $\overline{v}$ increases, nonaxisymmetric fronts disappear, as is the case of $\overline{v} = 2.5$.

approach each other, reducing the region of the nonaxisymmetric fronts until it finally disappear when $\overline{v} > 2.46$. This is also shown in Fig. 6.5, where we display the position of the transition points as we vary the average speed for the supportive flow. The curve representing the transition points separates regions where only stable axisymmetric fronts and nonaxisymmetric fronts can exist. This curve has a maximum value $\overline{v} = 2.46$ at $L = 3.7$. Consequently, for $\overline{v} = 2.46$ only stable axisymmetric fronts exist. A strong enough supportive Poiseuille flow will only allow stable axisymmetric fronts.

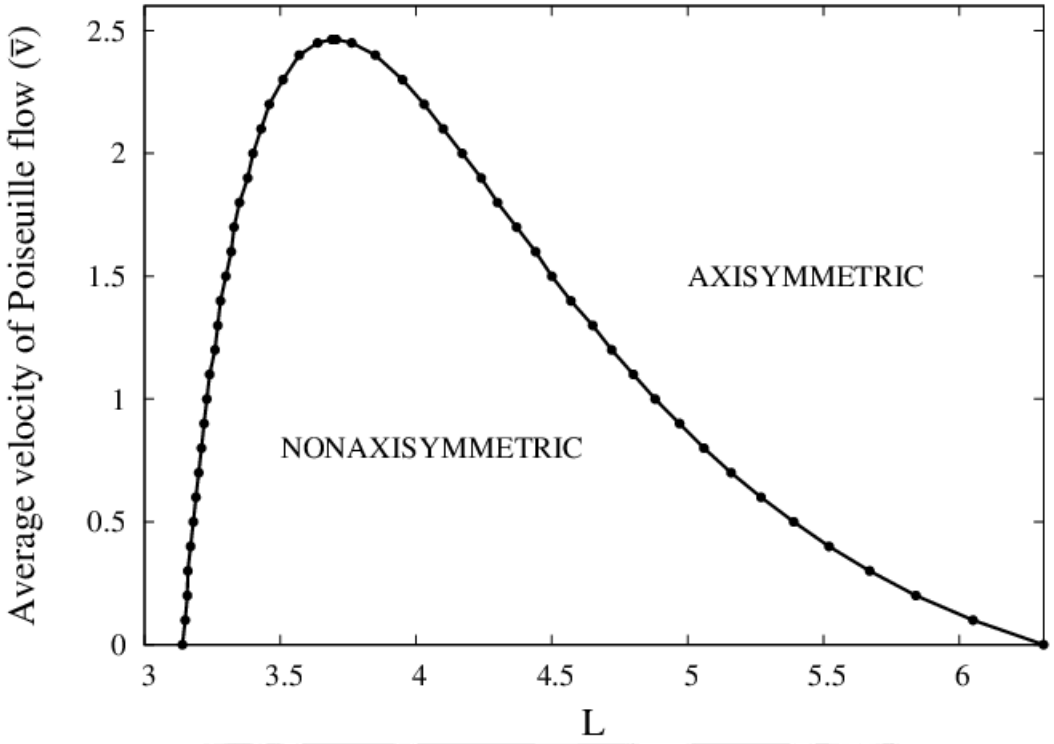

Figure 6.5: Regions for the existence of nonaxisymmetric and axisymmetric fronts for different values of the average flow velocity and plate separation. Only axisymmetric fronts can exit for $\bar{v} > 2.46$.

6.2 The effect of an adverse Poiseuille flow

We first obtain stationary stable fronts for different average velocities of the Poiseuille flow in the adverse direction while keeping the slab width constant. The slab width is set to $L = 3$ for comparison with the opposite case. The results are shown in Fig. 6.6. We first find a stable axisymmetric concave upward front for $\bar{v} = -2.0$ having a single minimum. As we increase the magnitude of the adverse flow ($\bar{v} = -2.5$) the front loses the axial symmetry, having one side higher than the other. Therefore, a strong enough Poiseuille flow in the adverse direction, which is an axisymmetric flow, can lead to a nonaxisymmetric front.

We apply a small Poiseuille flow in the adverse direction to study the effects on the velocities of the fronts. Figure 6.7 shows the front velocities for an average adverse speed of $\bar{v} = -0.1$. The original flat front without Poiseuille flow (see Fig. 5.4) becomes axisymmetric and loses stability to nonaxisymmetric

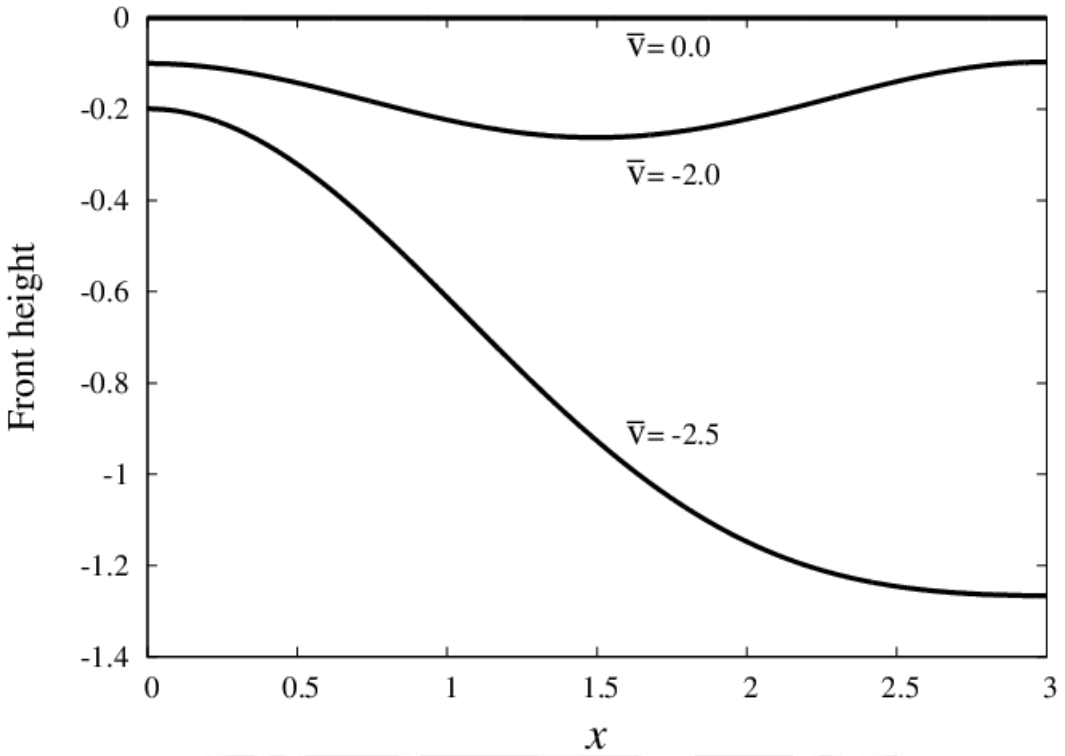

Figure 6.6: Front profiles for different average velocities of the Poiseuille flow in the adverse direction. Small adverse flows ($\bar{v} = -2.0$) allow stable axisymmetric fronts, but for higher speeds ($\bar{v} = -2.5$) the front becomes nonaxisymmetric. The fronts are shifted for comparison.

fronts (branch A) at L = 3.13. Branch A has a maximum speed at L = 3.75. This maximum is slightly smaller than the one obtained without Poiseuille flow (see Fig. 5.4). In addition, the adverse flow decreases the velocity of concave downward axisymmetric fronts (B_1) and increases the velocity of concave upward axisymmetric fronts (B_2). We notice that branch A becomes unstable before reaching branch B_1, leading to a small region where no front is stable. Branches C, D, and F correspond to nonaxisymmetric fronts. Branch C starts where fronts on branch B_2 become stable and finishes at L = 9.5, where it meets branch F. Both branch C and branch F are unstable. Branch D joins branch B_1 at L = 9.29, having two solutions for L smaller than this value. Branch D crosses over branches C and F, having a single solution for L > 9.29. A portion of branch D becomes stable due to the adverse flow. So in this case, we have two regions of bistability. The first one corresponds to upward and downward axisymmetric

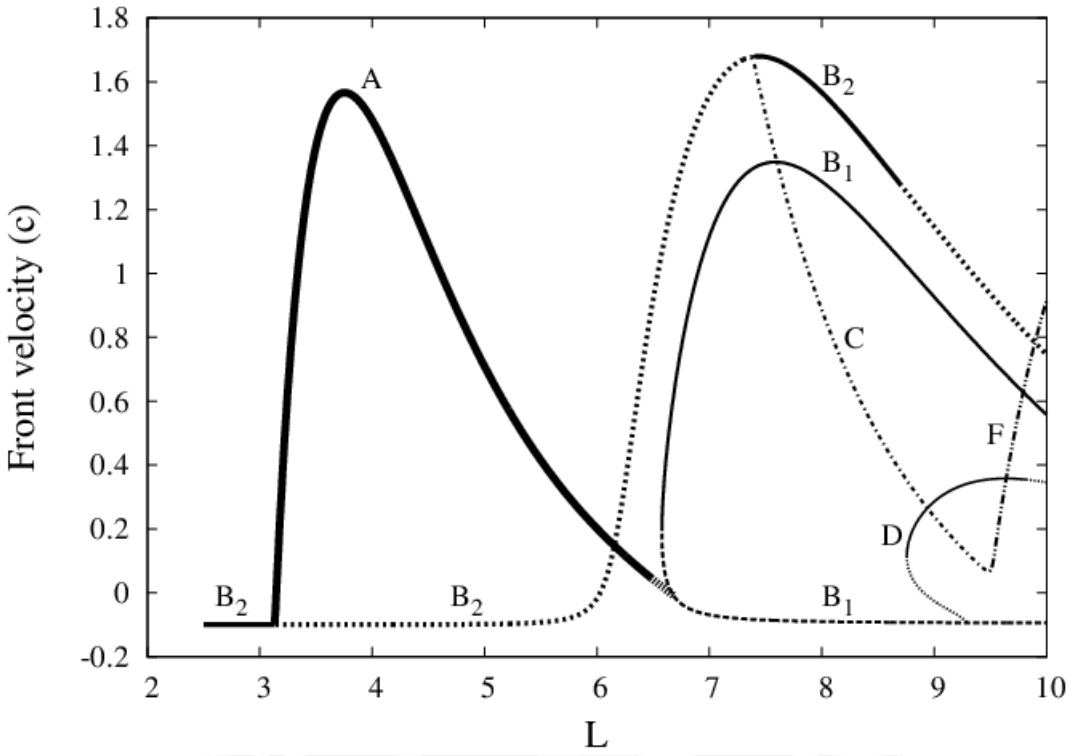

Figure 6.7: Front velocities subject to a Poiseuille flow in the adverse direction to the propagating front. The average velocity of the flow is $\bar{v} = -0.1$. Solid lines correspond to stable fronts; all broken lines correspond to unstable fronts. The thick solid line (A) corresponds to nonaxisymmetric fronts. Branch B_1 corresponds to axisymmetric fronts. Branch B_2 corresponds to other axisymmetric fronts. Broken lines correspond to nonaxisymmetric fronts. Line D also corresponds to other nonaxisymmetric fronts.

fronts and the other one corresponds to downward axisymmetric and nonaxisymmetric fronts. Therefore, the stability of the fronts can be affected by the adverse Poiseuille flow, modifying unstable fronts to become stable fronts.

We calculate the largest real part of the growth rate for an adverse flow ($\bar{v} = -0.1$). The results are shown in Fig. 6.8. The flat fronts for small values of L without Poiseuille flow (see Fig. 5.5) are now concave upward fronts. They are stable for $L < 3.13$, where they show a transition from negative to positive values of $\mathrm{Re}(\sigma)$. Branch A appears at this transition point, corresponding to nonaxisymmetric fronts. This branch has negative values for $\mathrm{Re}(\sigma)$ up to $L = 6.49$. We also find a region of bistability between concave upward axisymmetric fronts, associated with branch B_2, and fronts on branch B_1. This region of bistability is 8.5% larger than the one obtained without Poiseuille flow

(see Fig. 5.5). We also observe a small region, $6.49 < L < 6.58$, where all steady fronts are unstable. Stable concave downward axisymmetric fronts, associated with B_1, exist for $L > 6.58$. Branch D, which was completely unstable without Poiseuille flow, now has a region where $\mathrm{Re}(\sigma)$ is negative. Therefore, applying adverse Poiseuille flow results in stabilizing unstable fronts. In this case, adverse flow decreases the values of $\mathrm{Re}(\sigma)$ for nonaxisymmetric fronts and concave upward fronts, increasing their region of stability.

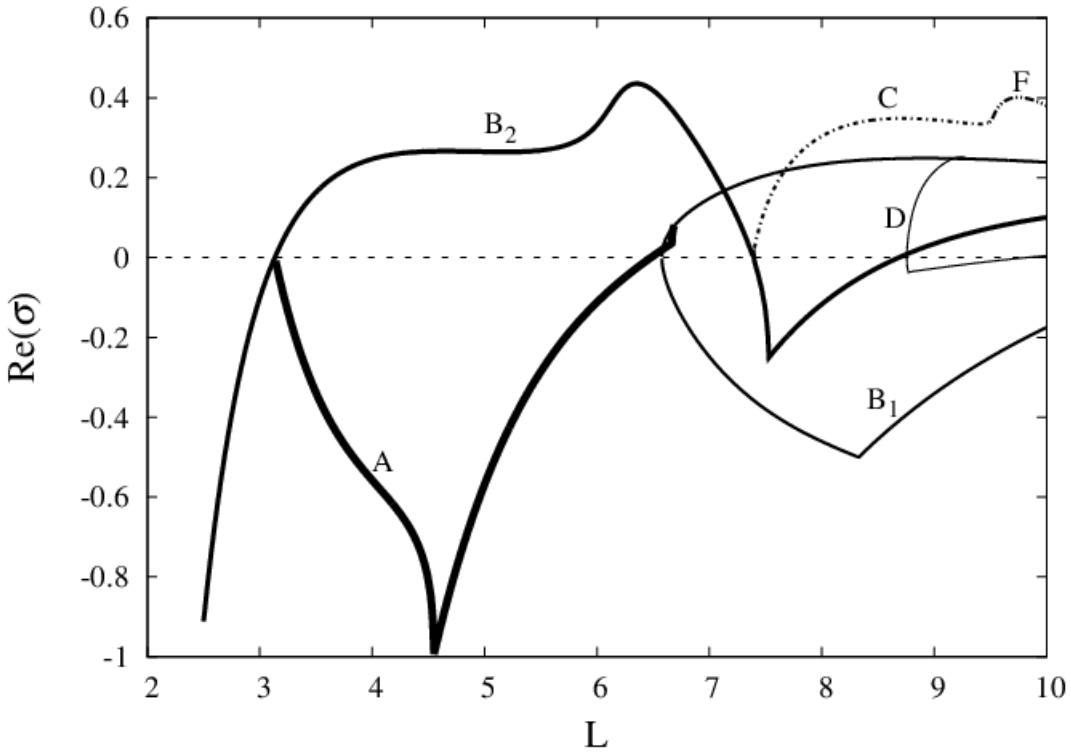

Figure 6.8: The largest real part of the eigenvalues σ for different distances L between plates. The Poiseuille flow is in the adverse direction to the propagating front. The average velocity of the flow is $\bar{v} = -0.1$. The front is unstable when the largest real part of the eigenvalues σ is positive. The thickest solid line (A) corresponds to nonaxisymmetric fronts. Solid line B_1 corresponds to axisymmetric fronts. Solid line B_2 also corresponds to other axisymmetric fronts. Broken lines (C and F) correspond to nonaxisymmetric fronts. Solid line D also corresponds to other nonaxisymmetric fronts.

Although an adverse Poiseuille flow opposes the direction of front propagation, some stable fronts increase their speeds for adverse flow. In Fig. 6.9(a) we display the speed as a function of the slab width L for different

flows in the adverse direction. Without Poiseuille flow the maximum axisymmetric flow speed is exactly the same as the maximum nonaxisymmetric flow speed [Fig. 6.9(a)]. Applying an adverse Poiseuille flow of $\bar{v} = -0.3$ reduces the speed of the nonaxisymmetric fronts. However, concave upward axisymmetric fronts have their speeds increased, while concave downward fronts have their speeds reduced. We also notice that at this speed stable nonaxisymmetric fronts appear at any value of L, whereas without flow they can only form for $L < 6.31$. Axisymmetric fronts can now form only at larger slab widths, sharing a region of bistability with nonaxisymmetric fronts. The curve representing stable axisymmetric fronts no longer meets the curve representing stable nonaxisymmetric fronts. As we reduce the velocity of the adverse flow to $\bar{v} = -0.5$, we also notice a similar effect [Fig. 6.9(b)]. But in this case, we also observe that the region where concave downward axisymmetric fronts can form is much smaller, being bounded at larger slab widths. Increasing the adverse speed further, to a velocity of $\bar{v} = -0.7$, we only find concave upward axisymmetric fronts. It is important to point out that the speeds of nonaxisymmetric fronts decrease with increasing adverse speed for widths near the maximum speed, but for larger slab widths the opposite effect takes place. For stable nonaxisymmetric fronts with relatively large slab widths ($L \geq 7$), increasing the adverse flow increases the velocity in the opposite direction of the flow.

To understand the effects of the Poiseuille flow on stable nonaxisymmetric fronts, we fix the width to $L = 3.5$, where a stable nonaxisymmetric front forms without flow, varying the average velocity of the flow. The results are shown in Fig. 6.10. For $\bar{v} = 0$, the axisymmetric front (flat front) is unstable and the nonaxisymmetric front is stable. Increasing the speed of a supportive Poiseuille flow brings the speeds of unstable axisymmetric fronts closer to the speeds of nonaxisymmetric fronts until they become the same at $\bar{v} = 2.27$. For larger values of the average velocity, only stable axisymmetric fronts are present (branch A in Fig. 6.10). In the case of adverse flows, we always obtain stable nonaxisymmetric fronts with decreasing front speeds. The axisymmetric fronts are initially unstable, but for strong adverse flows ($\bar{v} < -655$) the axisymmetric

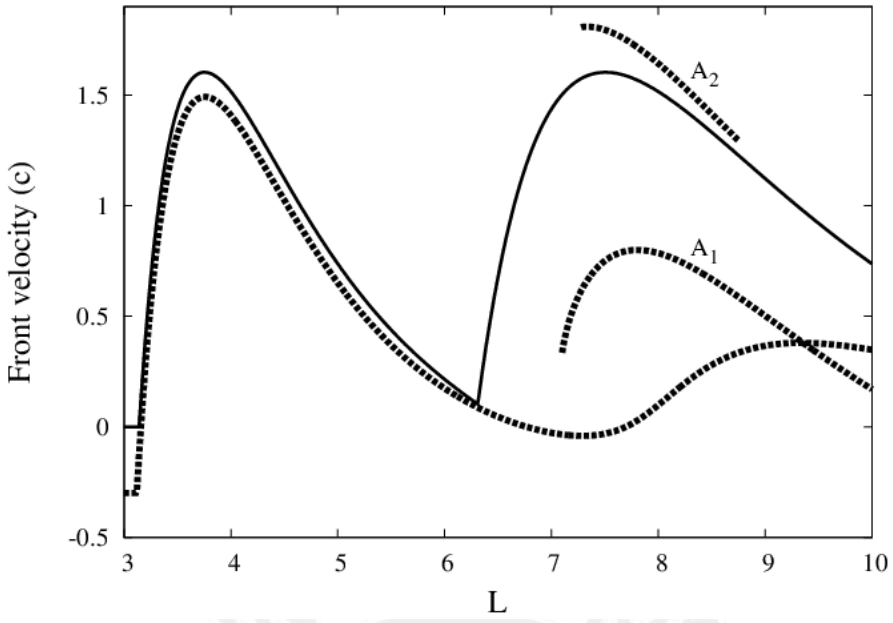

(a)

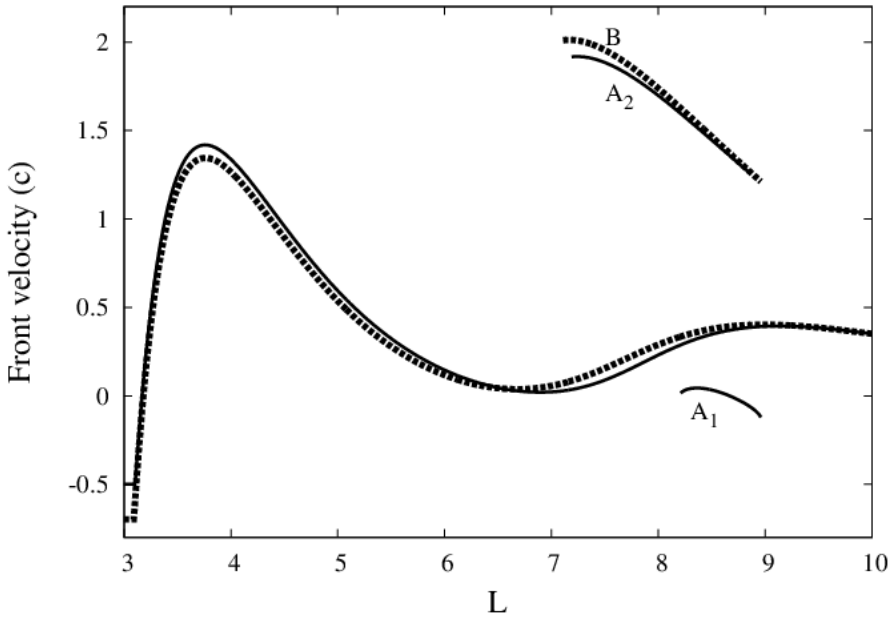

(b)

Figure 6.9: Front velocities as a function of the width L between plates for adverse Poiseuille flows. The figure only shows stable fronts. (a) The solid line corresponds to no Poiseuille flow ($\bar{v} = 0$), showing two maxima. The first one corresponds to stable nonaxisymmetric fronts; the second corresponds to axisymmetric fronts. The dashed line corresponds to $\bar{v} = -0.3$. Branches A_1 and A_2 represent stable axisymmetric fronts. (b) The solid line corresponds to $\bar{v} = -0.5$, with branches A_1 and A_2 representing axisymmetric fronts. The dashed line corresponds to $\bar{v} = -0.7$. Here there is only one branch B, corresponding to concave upward axisymmetric fronts.

fronts become stable again. As these axisymmetric fronts become stable, a branch of unstable nonaxisymmetric fronts appears (branch B in Fig. 6.10). While stable nonaxisymmetric fronts disappear at relatively low speeds of supportive flow, they are present even at high speeds of adverse flows.

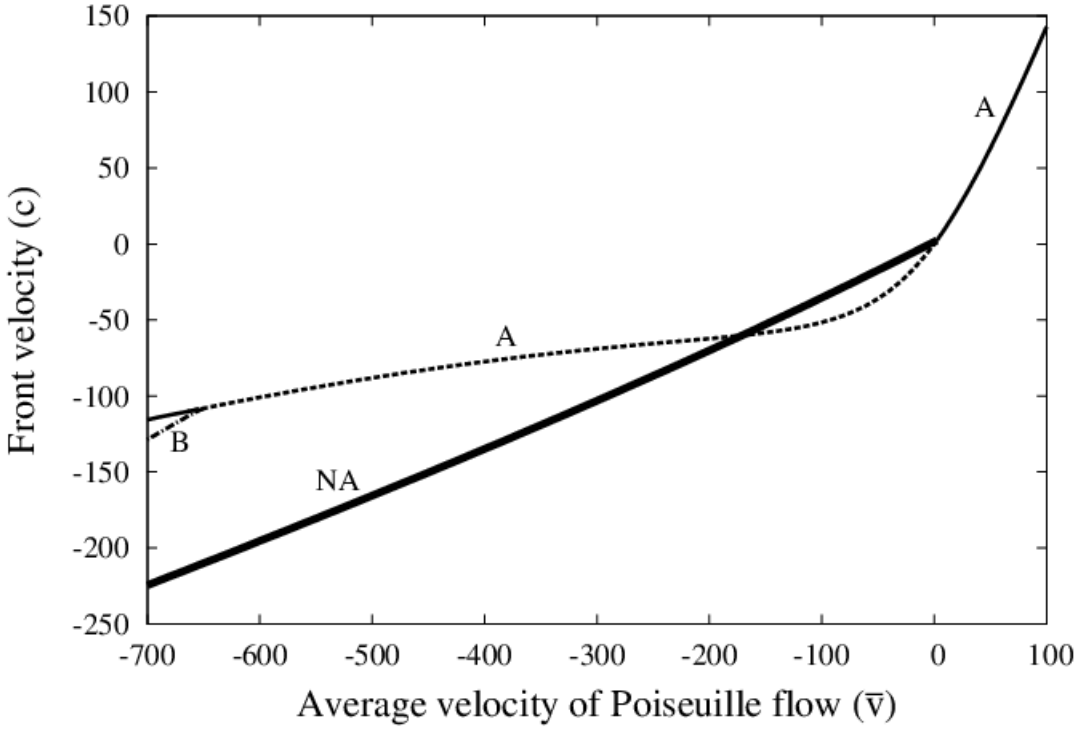

Figure 6.10: Front propagation velocity as a function of the average velocity of Poiseuille flow. The distance L between plates is 3.5. Branch A corresponds to axisymmetric fronts, both stable (solid lines) and unstable (dashed line). Branch B (dot-dashed line) corresponds to unstable nonaxisymmetric fronts. The thick solid line (NA) corresponds to stable nonaxisymmetric fronts.

6.3 Fronts evolving in time

Chemical systems can exhibit complex spatiotemporal behavior such as the Belousov-Zhabotinsky (BZ) reaction [95], including the modified BZ reactions [96], and the chlorite-thiosulfate (CT) reaction [97,98]. The BZ reaction is a chemical oscillator which exhibits a sequence of period-doubling bifurcations (the system shifts to a new oscillatory pattern with twice the period of its predecessor, leading in some cases to chaotic behavior). We use the KS

equation to describe the oscillatory and chaotic patterns. In order to contrast the effects of Poiseuille flow on oscillatory and chaotic patterns, we first calculate the period-doubling bifurcations and identify those bifurcations that lead to chaos in our system without fluid flow, and later we recalculate these bifurcations taking into account the presence of a supportive (or adverse) Poiseuille flow.

6.3.1 Numerical methods

In previous sections we focused on steady front solutions. We used a non-linear shooting method to obtain these solutions with their respective propagation velocities. In this section we focus on solutions that evolve with time, especially in oscillatory and chaotic solutions. To obtain these solutions, we require different numerical methods to those used in previous sections. We solve Eq. (6.2) by introducing Fourier series expansion on the front height h, hence it can be written as

$$h = \sum_{n=0} H_n(t)\cos(nqx), \tag{6.4}$$

Here the parameter q is defined by $q = \pi/\mathrm{L}$, where L is the width of the domain. The x coordinate varies from 0 to L. This Fourier series satisfy the boundary conditions at the vertical walls: $\partial h/\partial x = \partial^3 h/\partial x^3 = 0$. Introducing this Fourier series on h in Eq. (6.2), and projecting over the corresponding cosine function, we obtain a set of ordinary differential equations (ODEs)

$$\frac{dH_n}{dt} = (nq)^2 H_n - (nq)^4 H_n + \frac{q^2}{4}\sum_{\ell=1}\sum_{p=1} \ell p H_\ell H_p \left(\delta_{n,|\ell-p|} - \delta_{n,\ell+p}\right) + f_n \quad \text{for } n \geq 1 \tag{6.5}$$

and

$$\frac{dH_0}{dt} = \frac{q^2}{4}\sum_{p=1} p^2 H_p^2 + \bar{\mathrm{v}}. \tag{6.6}$$

Where the Fourier coefficient $H_0(t)$ provides the average front height and its derivative (dH_0/dt) corresponds to the front propagation velocity (c). The last term in Eq. (6.5) corresponds to the Fourier coefficient of the Poiseuille flow

$$f_n = \begin{cases} -\dfrac{24\bar{v}}{n^2\pi^2} & \text{for } n \text{ even} \\ 0 & \text{for } n \text{ odd} \end{cases} . \tag{6.7}$$

Thus Eq. (6.5) determines the time evolution of the Fourier coefficients of the front height h, which in turn determine the time evolution of the front.

We solve this set of ODEs numerically using an implicit Euler's method (or backward Euler method) for time evolution. To get a qualitative understanding of this method, we consider a single differential equation of the form

$$x' = g(t, x). \tag{6.8}$$

Here, $x' = dx/dt$, x is a function of t, while g is a function of t and x. In this case, the implicit Euler's formula is [99]

$$x_{n+1} = x_n + \Delta t\, g(t_{n+1}, x_{n+1}). \tag{6.9}$$

Where the time-step is Δt, the time at the n-th time-step is $t_n \equiv n\Delta t$, and the solution at the n-th time-step is $x_n \equiv x(t_n)$. Knowing x_n, we can find x_{n+1} implicitly, since x_{n+1} appears on both sides of Eq. (6.9). The implicit Euler´s formula is based on a Taylor series expansion of order 1. Although the implicit method is stable for linear systems, in general the implicit methods give a better stability [89]. It can be used with larger time-step. In contrast, the explicit Euler's formula is

$$x_{n+1} = x_n + \Delta t\, g(t_n, x_n). \tag{6.10}$$

This method requires smaller time-steps than the implicit method and it is not always stable.

6.3.2 Period-doubling transition to chaos

We have obtained a set of ordinary differential equations which corresponds to Eq. (6.5) and Eq. (6.6). We solve this set of equations numerically using an implicit Euler's method for time evolution with a time step set to $\Delta t = 0.001$ time

unit and a 25 term truncation for the Fourier coefficients H_n. We found no significant differences in the steady states with slightly fewer terms. We use small random initial conditions for each Fourier coefficient H_n at the beginning of the calculations and the system is let to evolve for a time to eliminate transient behavior. Since $H_0(t)$ provides the average position of the front, we define the velocity of the oscillatory (or chaotic) front as the velocity of the average position of the front (dH_0/dt). Hence we use Eq. (6.6) to calculate the front velocity. In Fig. 6.11a we show the front velocity as it varies with time (after a certain time to eliminate transient behavior). We observe that the front velocity oscillates between two values, a maximum and a minimum value. Since each of these two values repeats every 2 cycles, it is referred to as period-2 cycle. To obtain the results shown in Fig. 6.11a we set the domain width $\mathrm{L} = 8.7$. We now increase the value of the parameter to $\mathrm{L} = 9.01$. We observe that the front velocity oscillates among four different values, two relative maxima and two relative minima. It is referred to as period-4 cycle, since each of these values repeats every 4 cycles as shown in Fig. 6.11b. In contrast, we show in Fig. 6.12 (c) the chaotic behavior (aperiodic oscillations) of the front velocity for $\mathrm{L} = 9.024$. We can summarize the information of the three graphs given in Fig. 6.11 into a single graph using a bifurcation diagram as shown in Fig. 6.12. In this diagram we display the relative maximum and minimum values of the front velocity as it varies with time. Hence the oscillatory front velocity shown in Fig. 6.11a is represented by two points in the bifurcation diagram, the maximum and minimum values. Similarly, the oscillatory front velocity shown in Fig.6.11b is represented by four points in the bifurcation diagram, and so on. The chaotic behavior shown in Fig. 6.11c is represented by all the relative maxima and minima values of the front velocity ("infinite points") in the bifurcation diagram. Since the branches in this diagram split each time the period of the oscillation is doubled, it is referred to as period-doubling bifurcations [62].

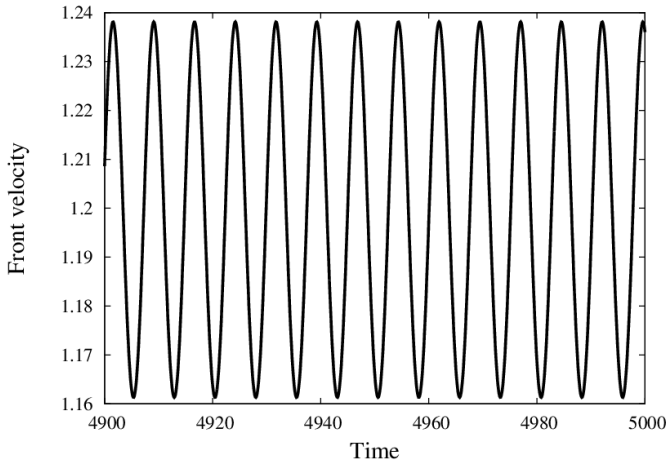

(a)

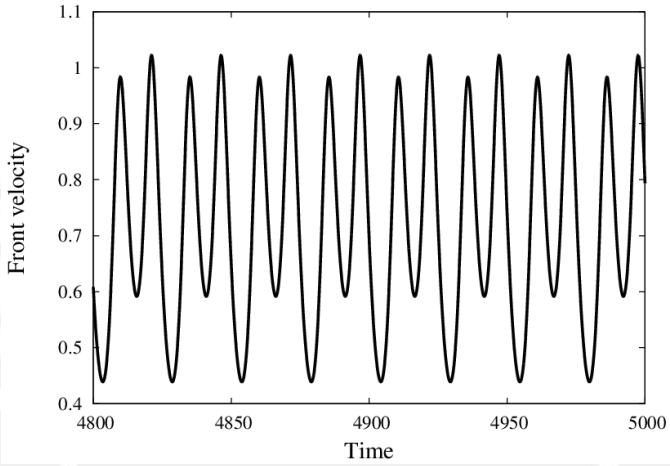

(b)

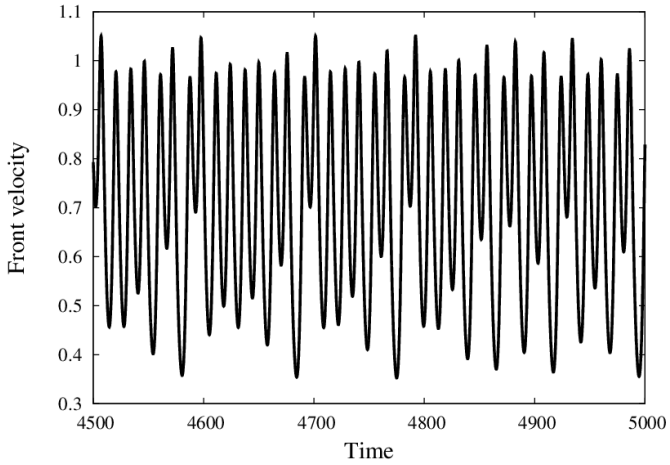

(c)

Figure 6.11: Front velocity oscillations with time. (a) Period-2 cycle obtained with $L = 8.7$. (b) Period-4 cycle obtained with $L = 9.01$. (c) Chaotic behavior (the oscillations are aperiodic) obtained with $L = 9.024$.

In Fig. 6.12 we observe a period doubling bifurcations in transition to chaos as we increase the width of the domain (L). We obtain this figure without external fluid flow. We observe that the oscillatory behavior starts at $L = 8.653$ and it is represented in the graph by two points corresponding to the relative maximum and minimum values of the front velocity. As we continue increasing L, these period-doubling bifurcations continue, reaching a chaotic behavior around $L = 9.022$. When we reach $L = 9.025$, the system achieves a stable steady solution.

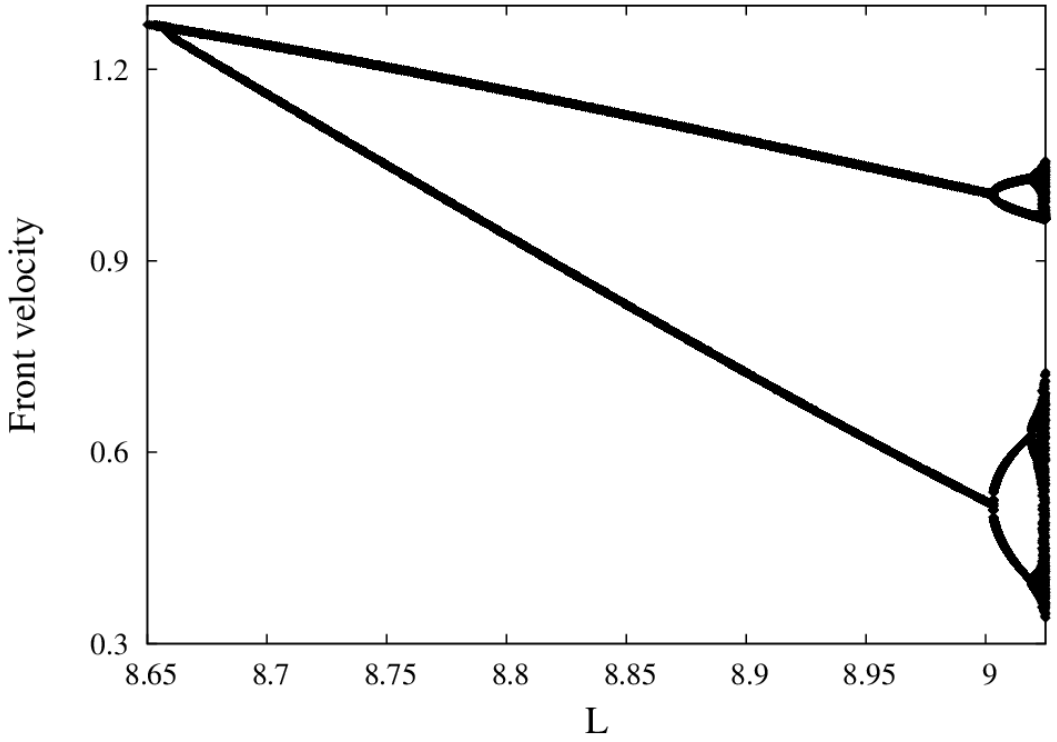

Figure 6.12: Bifurcation diagram without fluid flow showing the relative maximum and minimum of the time evolution of the front velocity. The period-doubling bifurcations increase as we increase the distance L between plates.

We obtain similar period-doubling bifurcations for a supportive Poiseuille flow ($\bar{v} = 0.1$) and an adverse Poiseuille flow ($\bar{v} = -0.1$). We show the results in Fig. 6.13 and Fig. 6.14, respectively. We observe that in the case of a supportive flow, the first bifurcation occurs at a lower value of L, namely,

$L = 8.622$ and in the case of an adverse flow, the first bifurcation occurs at a greater value: $L = 8.684$. We also notice that the interval of L where the period-doubling bifurcations occur is greater in the case of an adverse flow. Therefore, the adverse Poiseuille flow favors the period-doubling bifurcations.

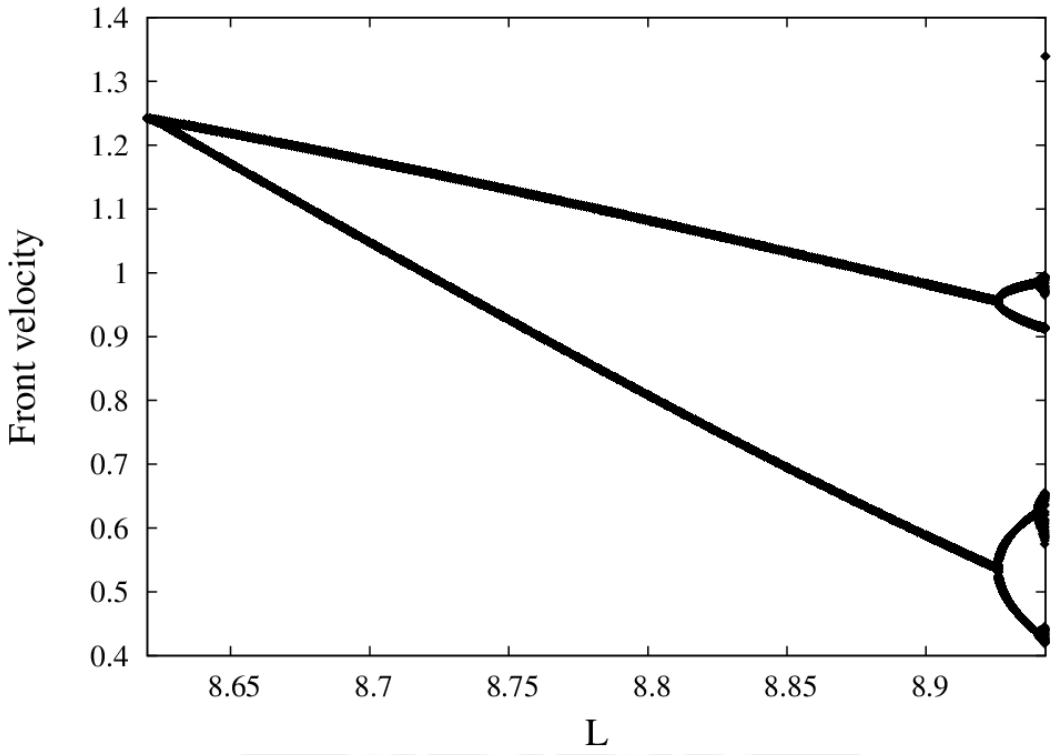

Figure 6.13: Bifurcation diagram for a supportive Poiseuille flow ($\bar{v} = 0.1$) showing the relative maximum and minimum of the time evolution of the front velocity. The period-doubling bifurcations increase as we increase the distance L between plates.

We have shown the front velocities for an average adverse speed of $\bar{v} = -0.1$ in Fig. 6.7 of Sec. 6.2. In this figure there are no stable steady solutions in the interval $6.477 < L < 6.578$. In this interval we find oscillatory solutions. We show in Fig. 6.15 the corresponding bifurcation diagram for these oscillatory solutions. The oscillatory behavior starts at $L = 6.477$ and we observe only one period-doubling bifurcation at $L = 6.536$. As we continue increasing L the system

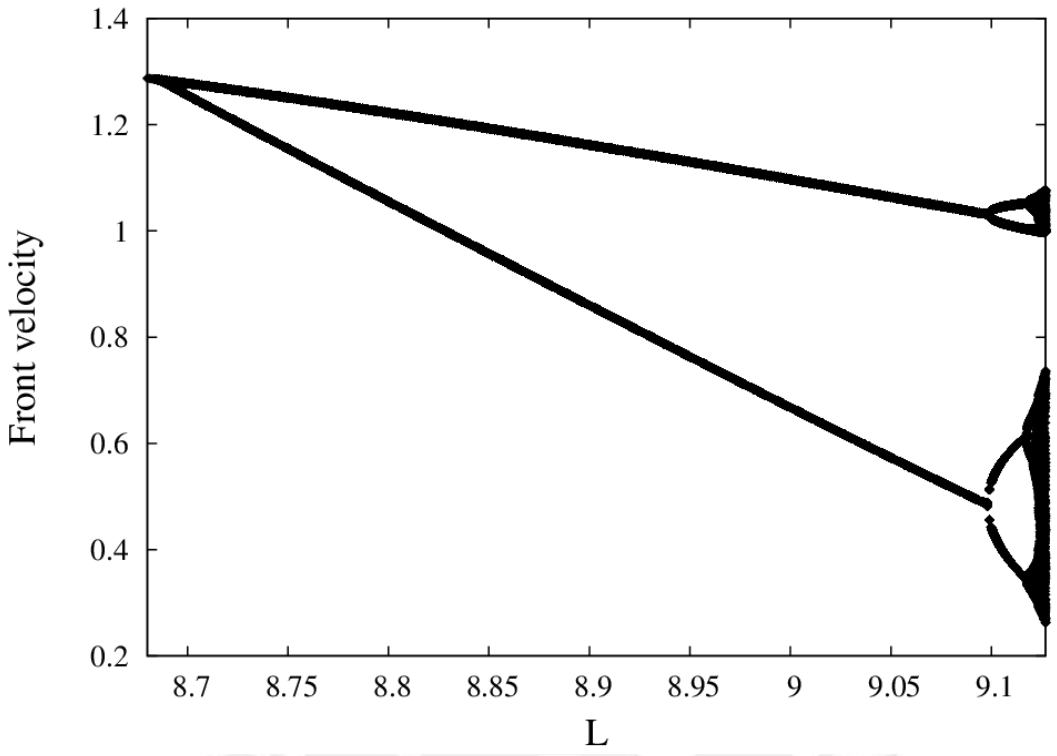

Figure 6.14: Bifurcation diagram for an adverse Poiseuille flow ($\bar{v} = -0.1$) showing the relative maximum and minimum of the time evolution of the front velocity. The period-doubling bifurcations increase as we increase the distance L between plates.

achieves a stable steady solution at $L = 6.578$. To study the effects of the Poiseuille flow on these particular oscillatory solutions, we calculate these oscillatory solutions for different values of the average Poiseuille flow velocity. We show in Fig. 6.16 the width L at which the oscillatory behavior starts and the width L at which the only one period-doubling bifurcation takes place in terms of the average Poiseuille flow velocity. We observe that these bifurcations points are shifted to greater values of L as we increase the magnitude of the adverse flow. These particular oscillatory solutions can be found with small adverse flow in the interval $-0.287 < \bar{v} < -0.03$. We also study solutions that evolve in time for greater values of L. The results are summarized in Table 6.1. Here we show the intervals where the oscillatory solutions appear with and without Poiseuille flow, and the regions where these oscillatory solutions become chaotic. We notice that the regions of oscillatory and chaotic solutions are affected by Poiseuille flow. Moreover, the adverse Poiseuille flow revealed new regions of oscillatory

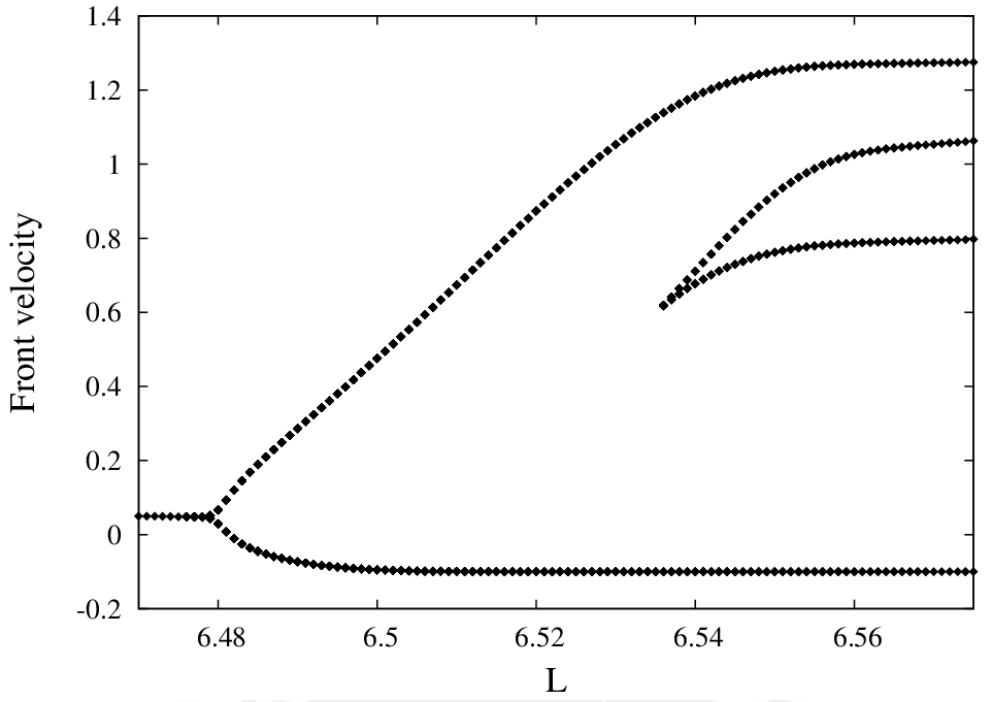

Figure 6.15: Bifurcation diagram for an adverse Poiseuille flow ($\bar{v} = -0.1$) showing the relative maximum and minimum of the time evolution of the front velocity.

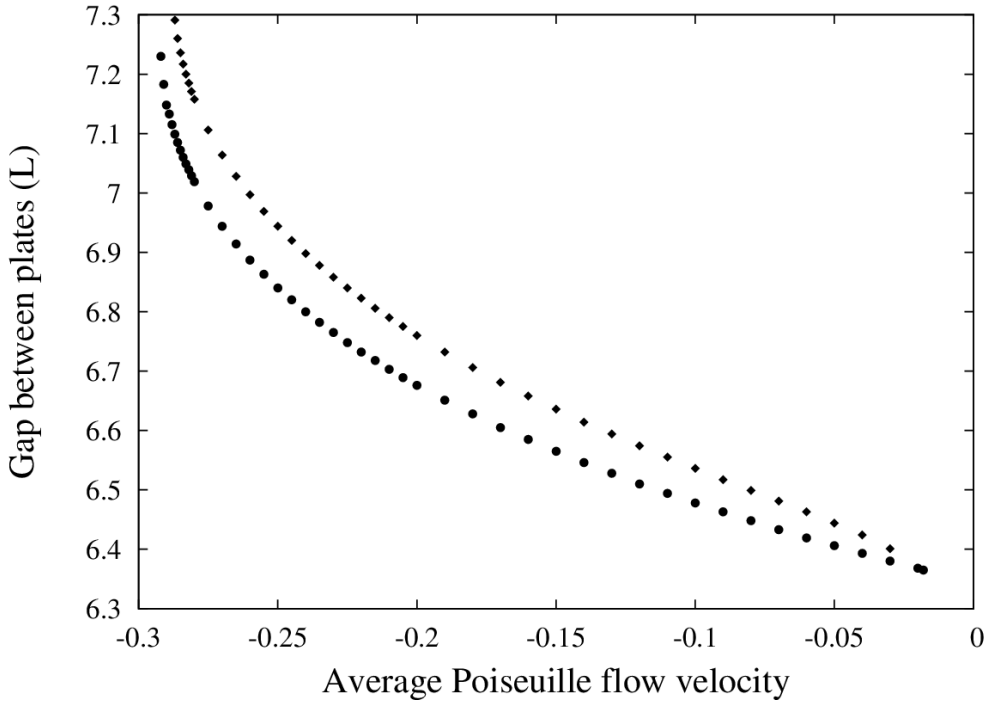

Figure 6.16: Location of the bifurcation points for different adverse Poiseuille flow. The dark circles correspond to the beginning of the oscillatory solutions, while the dark squares correspond to the first period-doubling bifurcation.

Description of the solutions	Adverse flow ($\bar{v} = -0.1$)	Without flow ($\bar{v} = 0.0$)	Supportive flow ($\bar{v} = 0.1$)
Oscillatory	$12.644 < L < 13.189$	$12.827 < L < 13.372$	$13.09 < L < 13.616$
Oscillatory	$15.532 < L < 16.184$	$15.777 < L < 16.265$	$15.97 < L < 16.372$
Oscillatory	$16.864 < L < 18.093$	$16.878 < L < 18.140$	$16.886 < L < 18.161$
Chaotic	$18.093 < L < 18.321$	$18.140 < L < 18.384$	$18.161 < L < 18.397$
Oscillatory	$18.321 < L < 19.537$	$18.384 < L < 19.317$	$18.397 < L < 19.113$
Chaotic	$19.537 < L < 19.644$	$19.317 < L < 19.801$	$19.113 < L < 19.984$
Oscillatory	$19.644 < L < 19.686$	$19.801 < L < 20.424$	$19.984 < L < 20.505$
Chaotic	$19.686 < L < 19.932$	$20.424 < L < 20.570$	$20.505 < L < 20.782$
Oscillatory	$19.932 < L < 20.008$	$20.570 < L < 21.289$	$20.782 < L < 21.303$
Chaotic	$20.008 < L < 20.178$	$21.289 < L < 22$	$21.303 < L < 22$
Oscillatory	$20.178 < L < 21.248$		
Chaotic	$21.248 < L < 22$		

Table 6.1: Window range of the oscillatory and chaotic solutions for greater values of the distance L between plates ($10 < L < 22$)

and chaotic solutions. Therefore a supportive Poiseuille flow shifts the beginning of the oscillatory behavior to greater values of L, while an adverse flow shifts them to lower values of L and reveals new regions of oscillatory and chaotic behavior.

6.4 Summary

We studied reaction fronts within a two-dimensional slab using the KS equation advected by a Poiseuille flow. The fronts exhibit transitions from a nonaxisymmetric to an axisymmetric profile. This transition can take place by changing the slab width L even without flow. Stable axisymmetric fronts develop when nonaxisymmetric fronts lose stability as we increase the width. Adding a Poiseuille flow will make the transitions occur at different widths, plus it will change the shape and speed of the fronts. Nonaxisymmetric fronts will remain stable for adverse flows, but they will disappear for strong supportive Poiseuille flows. In the latter case, the fronts become axisymmetric, having a maximum at the center of the slab. We also find stable axisymmetric fronts that have a minimum (concave upward fronts). They share a small region of bistability with concave upward fronts. A supportive Poiseuille flow will provide a higher increase in speed for concave downward fronts but has the opposite effect with the application of adverse flows. We also identify branches of unstable fronts that can turn into stable branches in the presence of a Poiseuille flow. In addition, the KS equation exhibits spatiotemporal chaos and the transitions to chaos are affected by the presence of a Poiseuille flow. We show some regions of oscillatory and chaotic solutions, including the period-doubling sequence in a bifurcation diagram.

Chapter 7

The effect of an external Couette flow on Kuramoto-Sivashinsky fronts

In previous chapter we studied the effect of a Poiseuille flow on steady reaction fronts described by the KS equation. We modified the KS equation to take into account the Poiseuille flow. We found that the structure of the steady fronts can be flat, axisymmetric, or nonaxisymmetric, depending on the gap between the plates and the average flow speed. Previous works with a cubic reaction-diffusion advection equation showed that Poiseuille flow between parallel plates changes the shape and the speed of stable fronts [48]. These results have been confirmed experimentally by Salin *et al.* working with tubes and Hele-Shaw cells. As we showed in Sec. 3.1, Poiseuille flow confined between two parallel plates with a constant pressure gradient gives rise to a symmetrical velocity profile. Now we are interested in the effects of an asymmetric fluid flow on steady reaction fronts described by the KS equation. A particularly advantageous candidate is the plane Couette flow (see Sec. 3.2), which involves pattern formation [100] and transition from laminar flow to turbulence [101]. In addition, the plane Couette flow corresponds to the limit case (of infinite cylinder radii) of Taylor-Couette flow, where fluid is confined between two concentric rotating cylinders. The Taylor-Couette flow has been used to measure fluid viscosity, and to study flow instabilities and pattern generation in non-equilibrium systems involving fluid motion [66,102]. In this chapter we will study the effects of Couette flow on patterns arising from front instabilities described by the KS equation. The KS equation exhibits spatiotemporal chaos and we can use this equation to model pattern formation. As in the previous chapter, we can adapt the KS equation to take into account the external flow. We look for steady front solutions and we determine their stability by executing a linear stability analysis. Finally, we compare our results with fronts developed under a Poiseuille flow.

7.1 Couette flow

Couette flow develops from the relative motion of two parallel plates separated by a constant distance resulting in a steady linear velocity profile. We consider fronts propagating between two infinite parallel plates separated by a small distance L. The parallel plates move in opposite directions, being u the relative velocity between the plates. Let the infinite plates be located at $x=0$ and $x=\mathrm{L}$, thus we have a plane Couette flow constrained by these infinite plates. In this regard, we consider that the plate located at $x=\mathrm{L}$ moves along the z direction with a constant velocity u, while the other plate remains stationary as shown in Fig. 3.2. Working in our system of dimensionless units defined in Sec. 5.1, the linear velocity profile is given by $v_z = u(x/\mathrm{L})$. We use the KS equation [Eq. (4.30)] with the addition of Couette flow to model the evolution of chemical fronts within the parallel plates [47]

$$\frac{\partial h}{\partial t} = -\frac{\partial^2 h}{\partial x^2} + \frac{1}{2}\left(\frac{\partial h}{\partial x}\right)^2 - \frac{\partial^4 h}{\partial x^4} + u\left(\frac{x}{\mathrm{L}}\right). \tag{7.1}$$

Here h represents the front height, relating the vertical z coordinate as a function of the horizontal x coordinate, and the time t. The last term in this equation corresponds to the linear velocity profile of Couette flow. The suitable boundary conditions at the plates are zero first and third partial derivatives for the front height with respect to the x coordinate [85]. We are interested in solutions that move steadily without changing their spatial profile at a constant speed. Therefore we can set the solutions as $h(x,t) = h_0(x) - ct$, where $h_0(x)$ corresponds to a stationary front under Couette flow in a reference frame moving with constant velocity c. We also consider that the average position of the spatial front profile is zero in this reference frame. Thus, in the absence of a Couette flow (u = 0), the KS equation exhibits a stationary flat front solution of zero height. We solve Eq. (7.1) using a nonlinear shooting method as we described in the previous chapter to solve Eq. (6.2). We also analyze the stability of the fronts using a linear stability analysis, which leads to Eq. (5.10). This eigenvalue equation determines the stability of $h_0(x)$, since solutions with negative real part of σ will decay with time.

7.2 Steady solutions

We obtain stationary fronts for different values of the slab width L while keeping constant the relative velocity u between the plates. These solutions correspond to KS equation with the addition of the Couette flow velocity solved using the shooting method. We also determine the stability of the fronts by calculating the growth rates σ. Figure 7.1 shows four different stable front profiles with the fluid velocity near them. The relative velocity between the plates is set to $u = 0.8$ to make these fronts stable. The front height is measured relative to the average front height. For $\mathrm{L} = 4.6$ we show a front having an inflection point at $x = 1.44$ (Fig. 7.1a). For $\mathrm{L} = 9.2$ we show three different front profiles: a front having a relative maximum near the middle of the slab width (Fig. 7.1b), a front having a relative minimum at $x = 3.82$ (Fig. 7.1c), and a front having three inflection points (Fig. 7.1d). Consequently, given a slab width, different stable fronts with different shapes can be developed.

We obtain fronts of different shapes and velocities as we vary the domain width L, while keeping constant the relative velocity u between the plates. To describe the fronts we defined the axis as a line parallel to the z axis passing through the center of the two-dimensional domain at $x = \mathrm{L}/2$. In the absence of fluid flow, the flat front is a solution for each value of the slab width L. We show in Fig. 7.2 the velocities of several fronts under Couette flow for different values of L. These velocities are measured with respect to the flat front velocity obtained without fluid flow. The relative velocity between the plates is $u = 0.2$. We find that the original nonaxisymmetric fronts separate into branches A_1 and A_2. These branches have the same velocities without Couette flow. In branch A_1, the front speed increases with increasing L until it reaches a maximum speed of 1.92 at $\mathrm{L} = 3.71,$, it then decreases until it meets branch B_1. The solutions of branch A_1 correspond to nonaxisymmetric fronts having an inflection point for $\mathrm{L} \leq 5.49$. For greater values of L, the solutions of branch A_1 exhibit a small relative maximum until it meets branch B_1. Branch A_2 also corresponds to nonaxisymmetric fronts having an inflection point, but these fronts have a higher side at $x = 0$ rather than at $x = \mathrm{L}$. This branch reaches a

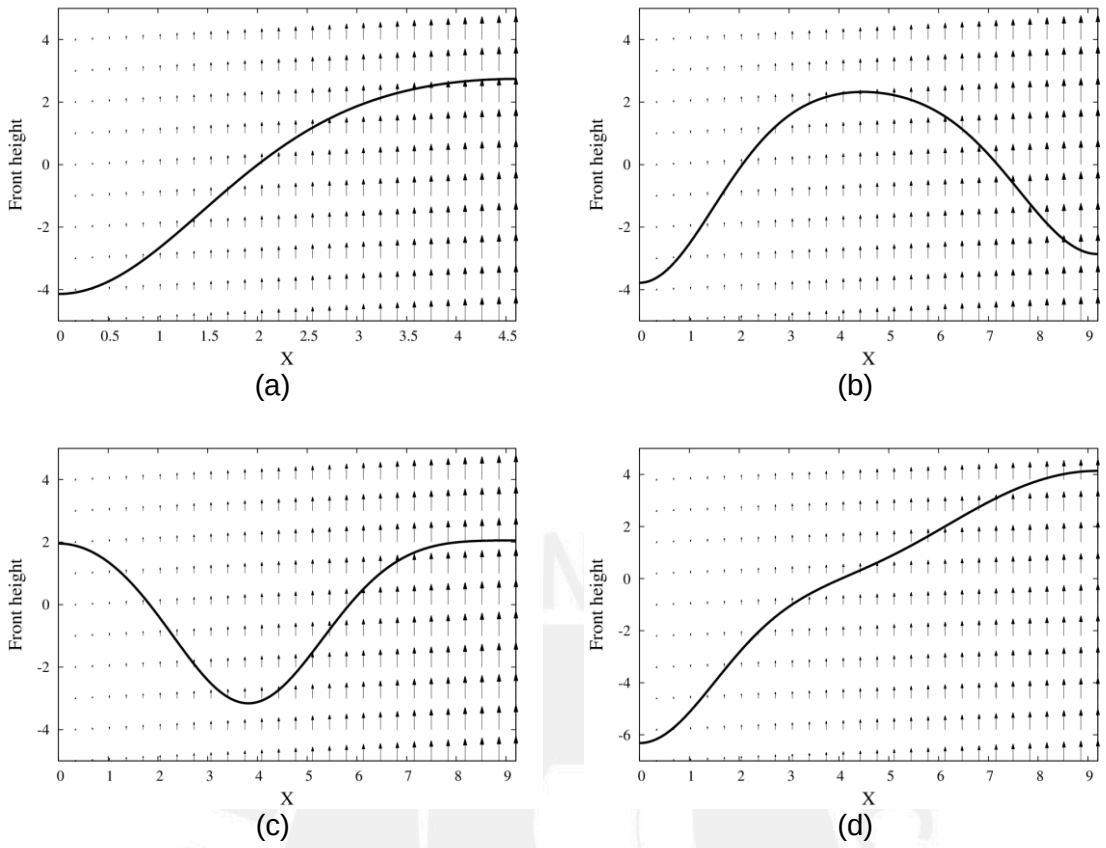

Figure 7.1: Fluid velocity near different steady stable nonaxisymmetric front profiles. The relative velocity between the plates is $u = 0.8$. The front height is measured from the average front height. (a) Front profile having an inflection point ($L = 4.6$). (b) Front profile having a relative maximum ($L = 9.2$). (c) Front profile having a relative minimum ($L = 9.2$). (d) Front profile having three inflection points ($L = 9.2$).

maximum speed of 1.47 at $L = 3.81$. Due to Couette flow, the speed of the original axisymmetric states now follows branches B_1, B_2, B_3. Solutions of branch B_1 correspond to nonaxisymmetric fronts with a relative maximum. This relative maximum increases as L increases. Branch B_1 reaches a maximum speed of 1.7 at $L = 7.51$. Branches B_2 and B_3 correspond to nonaxisymmetric fronts with a relative minimum. Couette flow also transforms flat front solutions into nonaxisymmetric fronts. These new solutions are part of the lowest portions of branches A_1, A_2, and B_2. Branches C and D have solutions with two different velocities for each value of L. The solutions of these branches correspond to other nonaxisymmetric fronts with three inflection points. Therefore, Couette flow turns flat or axisymmetric fronts into nonaxisymmetric fronts.

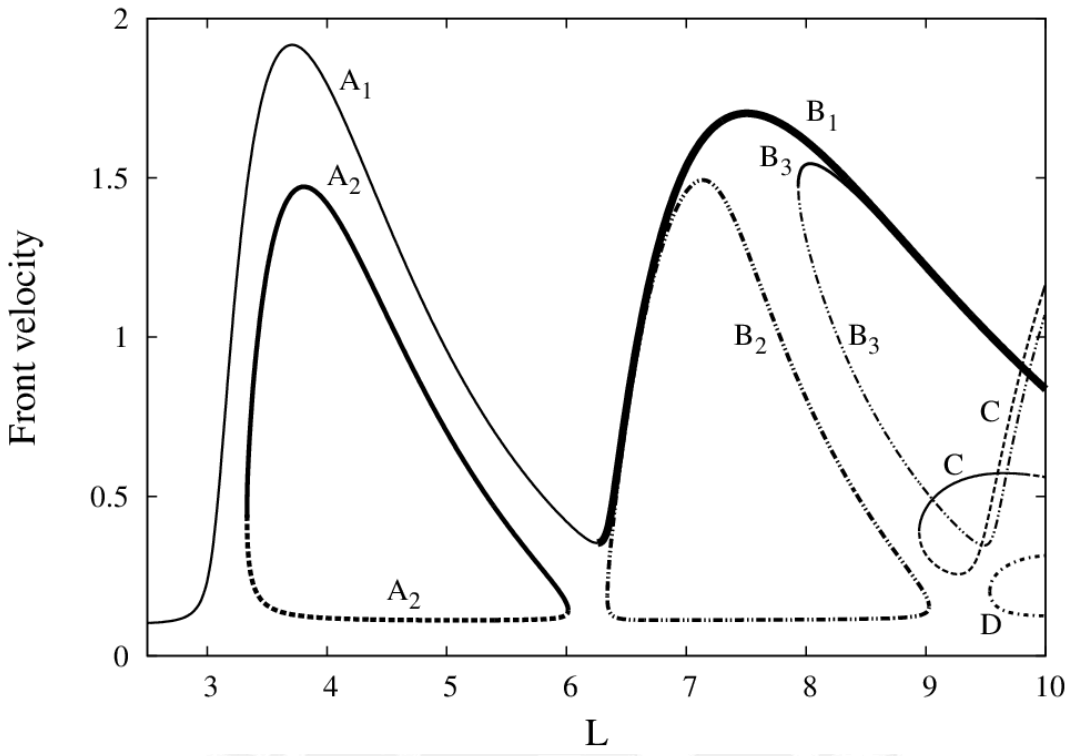

Figure 7.2: Front velocities relative to the flat front for different distances between plates (L). The relative velocity between the plates is $u = 0.2$. Solid lines correspond to stable fronts; all broken lines correspond to unstable fronts. Lines A_1 and A_2 correspond to nonaxisymmetric fronts, most of them having one inflection point. The thick solid line B_1 corresponds to nonaxisymmetric fronts with a relative maximum. Lines B_2 and B_3 correspond to nonaxisymmetric fronts with a relative minimum. Flat front solutions obtained without moving fluid ($u = 0$) change their shape and velocity due to Couette flow ($u = 0.2$). These new solutions correspond to the lowest part of lines A_1, A_2, and B_2. Lines C and D correspond to other nonaxisymmetric fronts with three inflection points.

The stability of the fronts is obtained by calculating the largest real part of the growth rate for front perturbations. We display these results in Fig. 7.3, where unstable fronts will have positive values of $\mathrm{Re}(\sigma)$. Branches A_1 and A_2 correspond to two nonaxisymmetric solutions with one inflection point. These solutions have a side near one boundary higher than the other. Solutions with their higher side at $x = L$ correspond to branch A_1. These solutions are stable. The other solutions with their higher side at $x = 0$ correspond to branch A_2. The growth rates indicate that branches A_1 and A_2 display a region of bistability in the interval $3.3 < L < 6.0$. Branch B_1 corresponds to nonaxisymmetric fronts with

a relative maximum. The growth rates show that these solutions are stable. Branch B_2 corresponds to nonaxisymmetric fronts with a relative minimum. These solutions are unstable. The other nonaxisymmetric fronts with a relative minimum corresponding to branch B_3 are also unstable, except in the interval $7.9 < L < 8.7$. This interval is a region of bistability for branches B_1 and B_3. Branch C, corresponding to nonaxisymmetric solutions with three inflection points, also exhibits a region of bistability with branch B_1 in the interval $8.9 < L < 9.9$. Branch D shows the real part of growth rates corresponding to nonaxisymmetric solutions with three inflection points. Their values are greater than zero, therefore these fronts are unstable. For all values of L in Fig. 7.3,

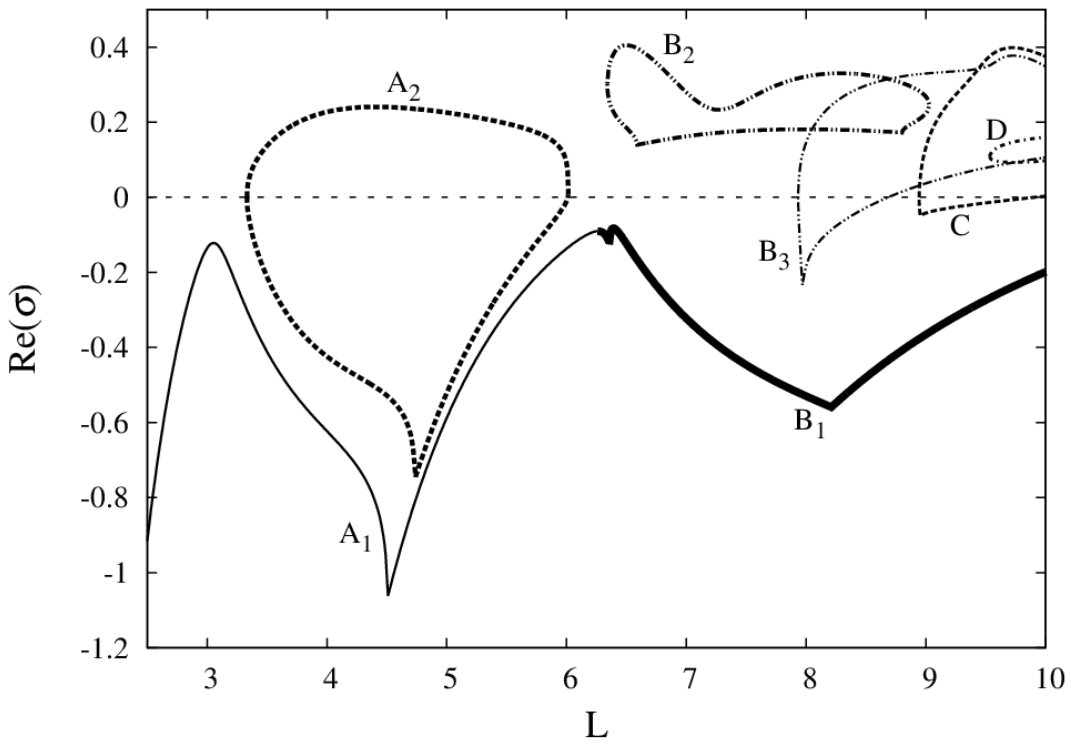

Figure 7.3: The largest real part of the eigenvalues σ for different distances L between plates. The relative velocity between the plates is $u = 0.2$. The front is unstable when the largest real part of the eigenvalues σ is positive. Solid lines A_1 and A_2 correspond to nonaxisymmetric fronts, most of them having one inflection point. The thick solid line B_1 corresponds to nonaxisymmetric fronts with a relative maximum. Lines B_2 and B_3 correspond to nonaxisymmetric fronts with a relative minimum. Lines C and D correspond to other nonaxisymmetric fronts with three inflection points.

we find at least one stable steady front. The introduction of Couette flow results in having only stable nonaxisymmetric solutions.

The effects of increasing the strength of the Couette flow by increasing the plate speed to $u = 0.6$, are displayed in Fig. 7.4. In this case we observe that the velocities in branches A_1 and B_1 increase as they reach a maximum at $L = 3.64$ and $L = 7.51$, respectively. However, the maximum speed in branches A_2 and B_2 reduces to 1.08 and 1.22, respectively. The domain of these branches have diminished by 62% and 51%, respectively, compared with the previous case with $u = 0.2$. Increasing the flow speed further, we observe that the domain of

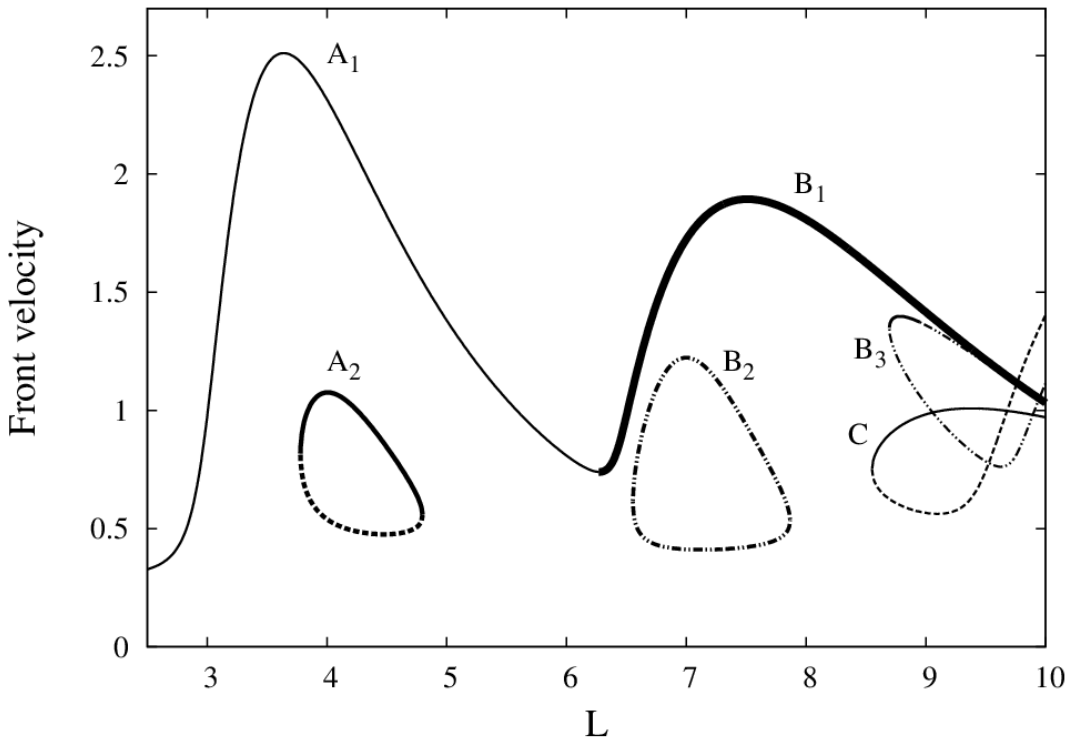

Figure 7.4: Front velocities relative to the flat front for different distances between plates (L). The relative velocity between the plates is $u = 0.6$. Solid lines correspond to stable fronts; all broken lines correspond to unstable fronts. Lines A_1 and A_2 correspond to nonaxisymmetric fronts, most of them having one inflection point. The thick solid line B_1 corresponds to nonaxisymmetric fronts with a relative maximum. Lines B_2 and B_3 correspond to nonaxisymmetric fronts with a relative minimum. Flat front solutions obtained without moving fluid ($u = 0$) change their shape and velocity due to Couette flow ($u = 0.6$). These new solutions correspond to the lowest part of lines A_1, A_2 and B_2. Line C corresponds to other nonaxisymmetric fronts with three inflection points.

branches A_2 and B_2 continue to shrink until they finally disappear. For $u > 0.69$, branch A_2 vanishes and branch B_2 disappears when $u > 0.82$. Branch B_3 also reduces its maximum speed and its domain length when increasing the Couette flow. This branch also vanishes for $u > 1.03$. On the contrary, when Couette flow is increased, branch C tends to increase its maximum speed and its domain length.

We also analyzed the stability of the fronts for a Couette flow having a relative speed between the plates $u = 0.6$. In Fig. 7.5 we display the largest real part of the growth rate for front perturbations. Branches A_1 and A_2, associated

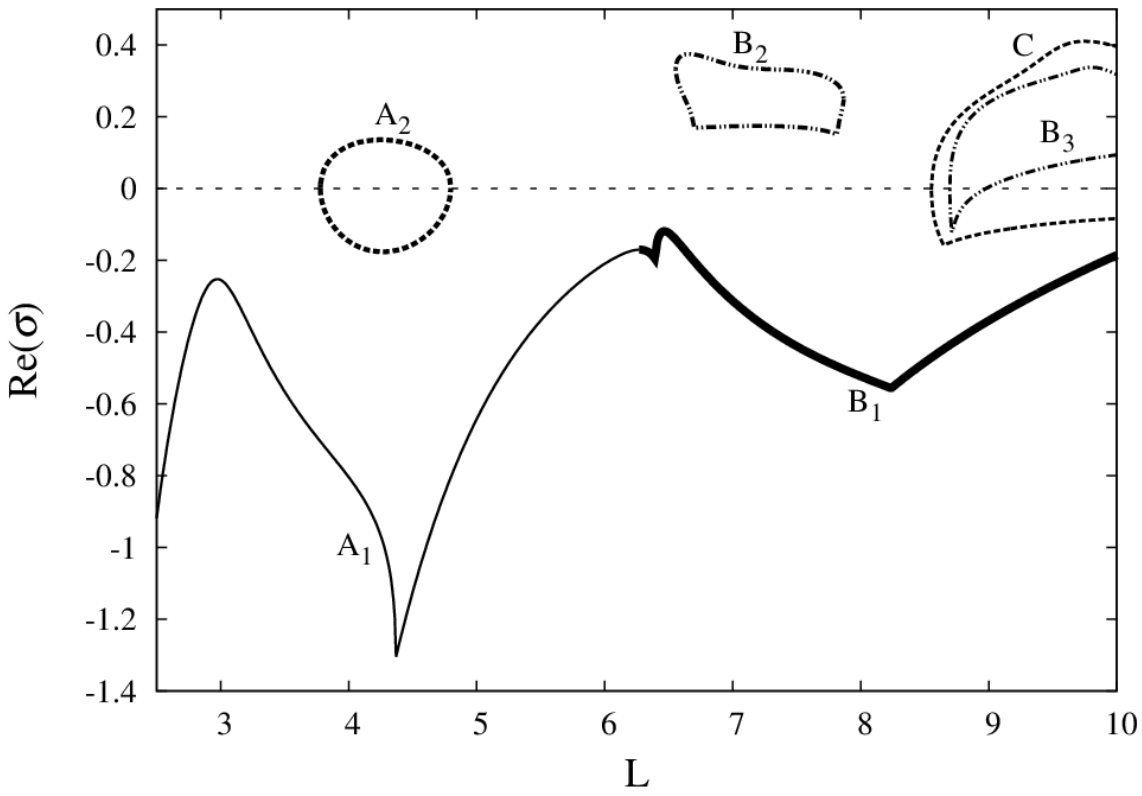

Figure 7.5: The largest real part of the eigenvalues σ for different distances L between plates. The relative velocity between the plates is $u = 0.6$. The front is unstable when the largest real part of the eigenvalues σ is positive. Lines A_1 and A_2 correspond to nonaxisymmetric fronts, most of them having one inflection point. The thick solid line $B1$ corresponds to nonaxisymmetric fronts with a relative maximum. Lines B_2 and B_3 correspond to nonaxisymmetric fronts with a relative minimum. Line C corresponds to other nonaxisymmetric fronts with three inflection points.

with nonaxisymmetric fronts with one inflection point share a region of bistability in the interval $3.8 < L < 4.8$. Branch A_1 increases slightly the magnitude of the negative values of the growth rates; compared with the previous case with $u = 0.2$. Nevertheless in branch A_2 the values are considerably reduced. Branch B_1 is a stable solution, whereas the solution for branch B_2 is always unstable. Branch B_3 exhibits a small region of stability in the interval $8.7 < L < 9.0$. However, branch C has increased its region of stability by 50% due to the increasing of Couette flow speed. Consequently, increasing the Couette flow speed favors the stability of the branches A_1, B_1 and C, while the other branches tend to reduce their regions of stability until they finally disappear.

7.3 Strong Couette flow

Another way to obtain different types of fronts is by changing the relative velocity between the plates while keeping the plate separation constant. In Fig. 7.6, we show the front propagation velocity for different fronts as a function of the relative velocity between the plates with a constant slab width equal to $L = 7.5$. For $u = 0$ there are three solutions, but only one of them is stable. The stable solution corresponds to branch B_1, being axisymmetric with a relative maximum at the center. The unstable solutions for $u = 0$ correspond to branch B_2. The solution with zero velocity corresponds to flat front solution, while the other solution corresponds to a nonaxisymmetric front solution with a relative minimum. The lower portion of branch B_2 corresponds to a modified flat front solution due to Couette flow; it becomes now a nonaxisymmetric front with an inflection point. For $u > 0.25$, this solution begins to show a relative minimum until it disappears for $u > 0.726$. The upper portion of branch B_2 shows the response of the unstable nonaxisymmetric front with a relative minimum due to Couette flow speed. This solution also disappears for $u > 0.726$. The initially stable axisymmetric front with $u = 0$ having a relative maximum changes by the action of the Couette flow: the maximum shifts away from the center of the two-dimensional domain thus losing the axial symmetry. However, these solutions remain stable as we increase the relative velocity u. We find a region of bistability in the interval $2.0 < u < 2.8$. The nonaxisymmetric fronts with a relative

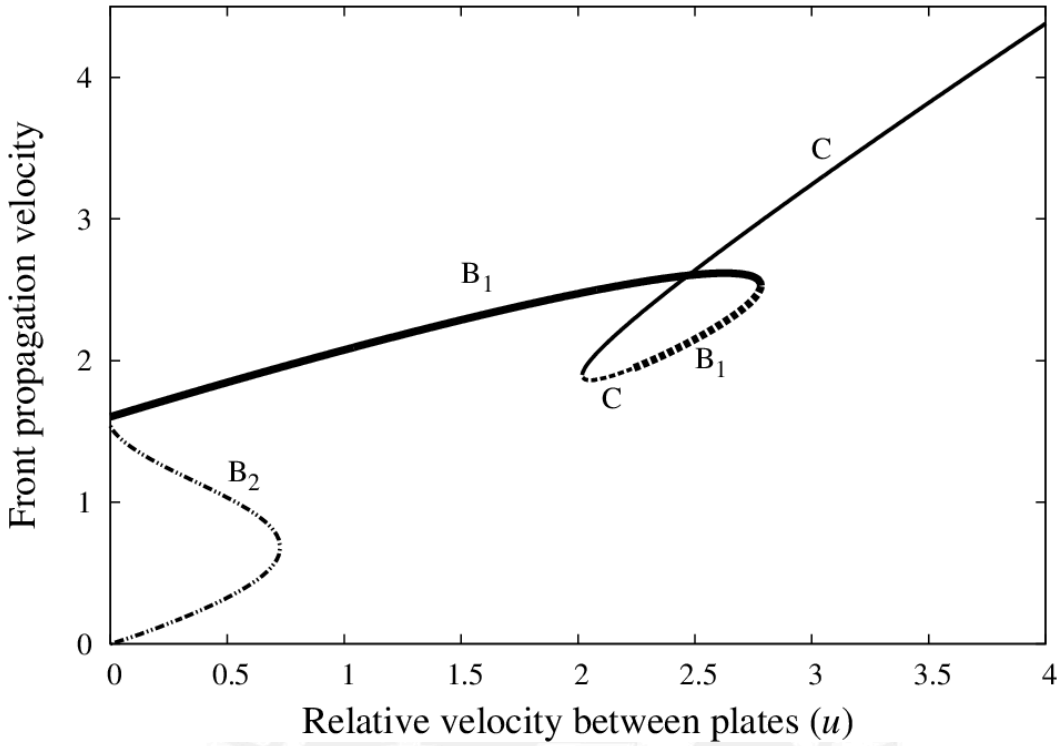

Figure 7.6: Front velocity in terms of the relative velocity (u) between the plates. The distance L between the plates is 7.5. Line B_1 corresponds to nonaxisymmetric fronts with a relative maximum, both stable (solid line) and unstable (dashed line). Line C corresponds to nonaxisymmetric fronts with three inflection points, both stable (solid line) and unstable (dashed line). Line B_2 corresponds to unstable nonaxisymmetric fronts with a relative minimum. The lower portion of B_2 shows the flat front transformation due to Couette flow.

maximum (branch B_1) coexist with nonaxisymmetric fronts with three inflection points (branch C). Within this interval, we also find unstable solutions in branches B_1 and C. For $u > 2.78$ only stable nonaxisymmetric fronts with three inflection points exist. To study in more detail the fronts found in branches B_1 and C in the region of bistability of Fig. 7.6, we choose plate velocities in this region computing the stable fronts as functions of the domain width L. In Fig. 7.7a we display the front velocities for stable fronts with $u = 2.5$. We observe that branches A_1 and C meet at $x = 6.97$, while branches B_1 and C cross each other two times at $x = 7.05$ and $x = 7.45$. However, branch B_1 shows a reduced domain. The domain of branch B_1 starts to decrease for $u > 2.34$. In Fig. 7.7b we

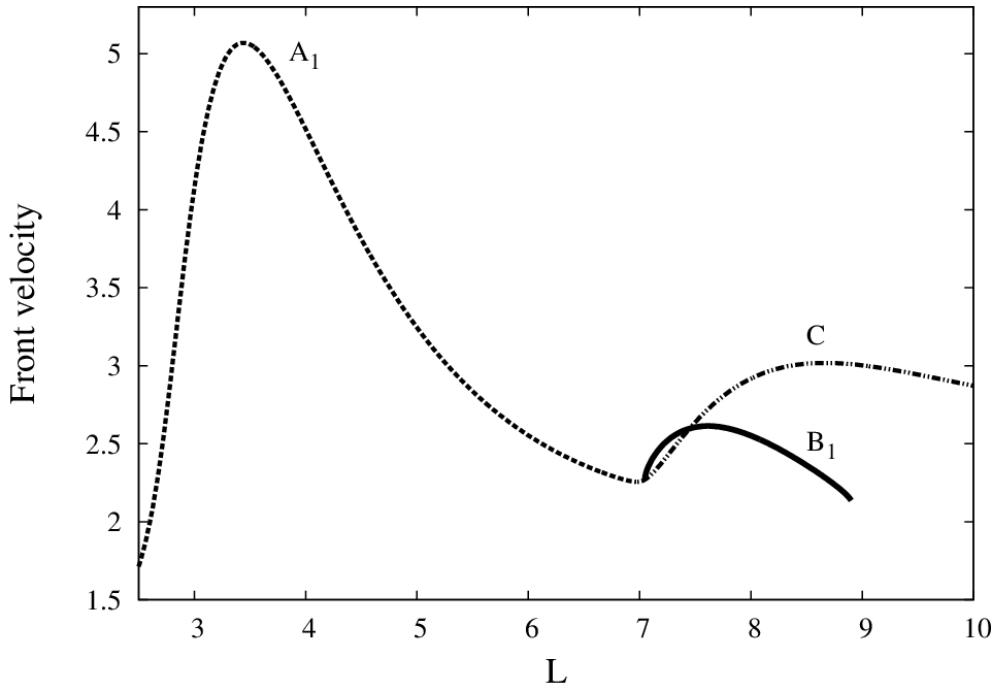

(a)

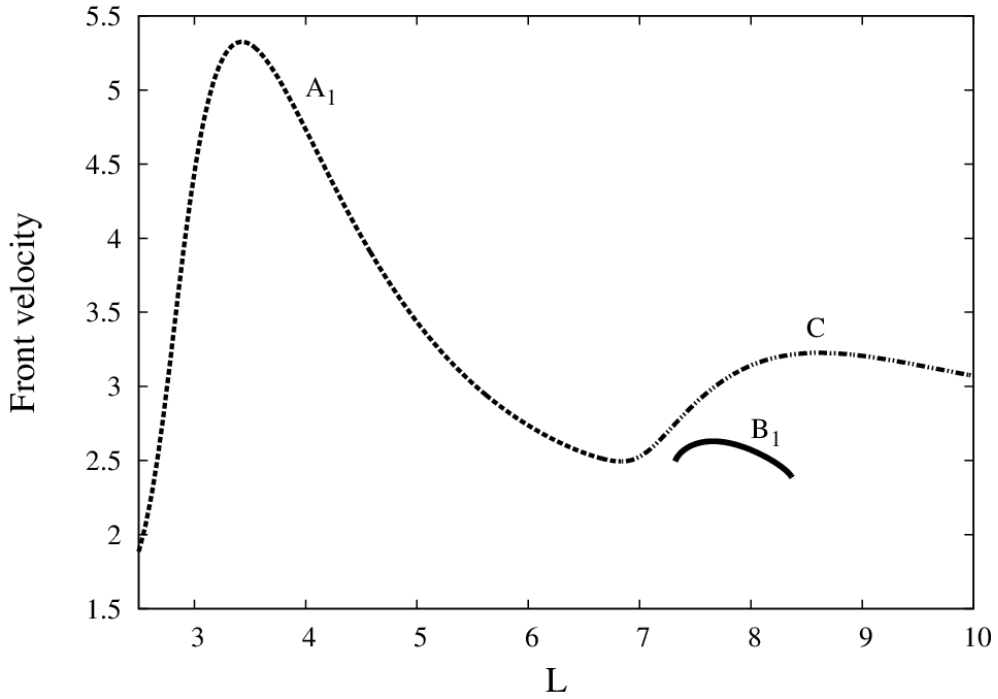

(b)

Figure 7.7: Front velocities relative to the flat front for different distances between plates (L). The figure only shows stable fronts. Broken line A_1 corresponds to nonaxisymmetric fronts, most of them having one inflection point. Solid line B_1 corresponds to nonaxisymmetric fronts with a relative maximum. Broken line C corresponds to other nonaxisymmetric fronts with three inflection points. The relative velocities (u) considered here are: (a) $u = 2.5$, and (b) $u = 2.7$.

display the results for $u = 2.7$. Branches A_1 and C meet each other at $x = 6.83$. The domain of branch B_1 decreases compared with the previous case with $u = 2.5$. If we display similar plots for different speeds, we will find that branch B_1 vanishes for $u > 2.82$. Thus, we will only find branches A_1 and C for these higher speeds.

As we increase the relative speed of the plates, the speed of the fronts increases, with the largest increase of speed taking place for solutions arising from nonaxisymmetric fronts at $u = 0$. Fronts that were originally symmetric at $u = 0$, achieve a lower increase of speed. This is shown in Fig. 7.8, where we display the largest possible front speed as we vary L, for different relative

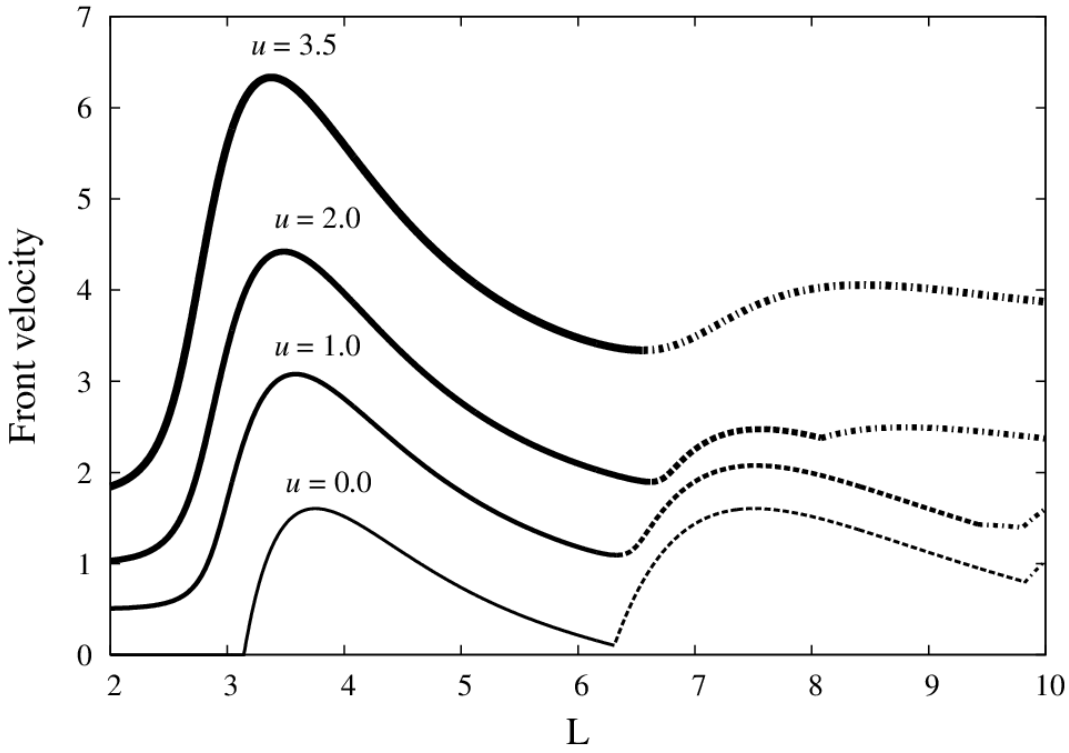

Figure 7.8: Largest front velocities as a function of the slab width L for different plate velocities u. All solid lines correspond to stable nonaxisymmetric fronts most of them having one inflection point (branch A_1). All dashed lines correspond to stable branches (B_1). These branches correspond to nonaxisymmetric fronts with a relative maximum except for $u = 0$ where they are axisymmetric. All two-dash lines correspond to other nonaxisymmetric fronts with three inflection points (branch C).

velocities u. Here, the solid lines correspond to nonaxisymmetric fronts (branch A_1) with different relative velocities u. The dashed lines (branch B_1) correspond to originally axisymmetric fronts without fluid flow, which turn into nonaxisymmetric fronts as Couette flow speed is increased. The two-dash lines correspond to nonaxisymmetric fronts with three inflection points (branch C) for different relative velocities u. Without fluid flow, flat front solutions which have zero velocity are the only solutions for $L < \pi$. The nonaxisymmetric solutions with three inflection points have the largest speed for $L > 9.82$. As Couette flow is applied, the flat front solutions become nonaxisymmetric, being part of branch A_1. As we continue increasing Couette flow speed, the fronts associated with branch C increase their speed faster than those of branch B_1. This results in the increment of the domain of branch C, while the domain of branch B_1 decreases. Eventually, branches A_1 and C will have the largest speed in their respective domains for $u > 2.57$. However, the speed of branch A_1 increases much faster than branch C. Therefore the nonaxisymmetric fronts with one inflection point show the largest increase in speed when the relative velocity u is increased.

7.4 Comparison with fronts developed under a Poiseuille flow

Without external flow, axisymmetric fronts exhibit the same velocities, but with an external flow they separate. Adding a supportive Poiseuille flow decreases the speed of stable concave upward axisymmetric fronts, increases slightly the speed of stable nonaxisymmetric fronts, but the highest increase of speed corresponds to concave downward axisymmetric fronts. Therefore, a supportive Poiseuille flow favors concave downward axisymmetric fronts, increasing their velocities much more than stable nonaxisymmetric fronts. On the contrary, an adverse flow decreases the maximum speed of stable nonaxisymmetric fronts and concave downward axisymmetric fronts, but increases the maximum speed of concave upward axisymmetric fronts, which exhibit a small region of stability. In contrast, applying a Couette flow will increase the maximum speed of stable nonaxisymmetric fronts with a higher side at the moving plate and decrease the maximum speed of the other stable nonaxisymmetric fronts. Therefore, the separation of nonaxisymmetric fronts with different speeds takes place on

Couette flows, but not in Poiseuille flows. In the case of the axisymmetric fronts without external fluid flow, they will lose their symmetry due to Couette flow, becoming nonaxisymmetric with a relative maximum or minimum. However, their velocities will not increase as fast as the nonaxisymmetric fronts with a higher side at the moving plate. We also find that nonaxisymmetric fronts remain stable for adverse Poiseuille flows, but they disappear for strong supportive Poiseuille flows. In contrast, strong Couette flows will increase the velocities of nonaxisymmetric fronts with a higher side at the moving plate. However, the nonaxisymmetric fronts with the higher side at the stationary plate will disappear.

We also observe that the stability of the fronts can be affected by an external flow. The effects of advection in fronts described by the KS equation can be experimentally achieved in reactions with fronts that exhibit diffusive instabilities [23]. Advection can be added for reactions taking place inside a thin tube by pushing the fluid (Poiseuille flow), or by generating a Couette flow using a moving wall confining a fluid layer. Experiments in different types of flow could test the results from our work, such as the separation of nonaxisymmetric fronts with different speeds, which could be observed on Couette flows, but not in Poiseuille flows.

7.5 Summary

We studied the effect of Couette flow over reaction fronts between two parallel plates separated by a small distance L. The reaction fronts are modeled using the KS equation, including the linear velocity profile produced by Couette flow. We determine the stability of the fronts by performing a linear stability analysis. Without fluid flow, the stability of the fronts depends on the width of the gap L between the plates. As we increase L, stable front profiles change first from flat to nonaxisymmetric, and then to completely axisymmetric. The nonaxisymmetric fronts exhibit an inflection point, while the axisymmetric fronts have a maximum (or minimum) at the middle of the gap between the plates. Applying a Couette flow will increase the speed of nonaxisymmetric fronts with a higher side at the moving plate, but decreases the maximum speed and the range of stability of the nonaxisymmetric fronts with a higher side at the stationary plate. These two

types of nonaxisymmetric fronts share a region of bistability. The presence of Couette flow will turn originally axisymmetric fronts (without external fluid flow) into nonaxisymmetric fronts with a relative maximum (or minimum). The nonaxisymmetric fronts with a relative maximum also share regions of bistability with the other nonaxisymmetric fronts with a relative minimum. However, adding a strong Couette flow will make these nonaxisymmetric fronts with a relative maximum (or minimum) disappear, and new stable nonaxisymmetric fronts with three inflection points will appear. Moreover, the nonaxisymmetric fronts with a higher side at the stationary plate will also disappear. Thus, a strong Couette flow will increase the stability and velocity of nonaxisymmetric fronts with one or three inflection points, having their higher side at the moving plate. It is worth mentioning that the branch containing the nonaxisymmetric fronts with three inflection points (branch C) would be completely unstable without moving fluid flow, thus Couette flow can reveal otherwise unstable solutions.

Chapter 8

Rayleigh-Taylor instabilities on steady Kuramoto-Sivashinsky fronts

Propagation of chemical fronts under the effects of convection due to a Rayleigh-Taylor type of instability has been studied in several systems such as iodate-arsenous acid mixtures [42,43], Belousov-Zhabotinsky reaction inside a vertical tube [44], iron(II)-nitric acid reaction [103], the chlorite-tetrathionate reaction [104,105], and the iodate-sulfate system [45]. The interaction of diffusive instabilities and fluid flow was modeled by coupling hydrodynamics to the corresponding reaction-diffusion equations [51,52]. In previous chapters we study the effects of fluid flow on fronts described by the KS equation. We first impose an external Poiseuille flow (see Chap. 6) and we later impose an external Couette flow on the fronts (see Chap. 7). In these studies we did not take into account density differences across the front. Here we analyze the behavior of steady structures appearing from the combined effects of the dynamics of the KS equation and the Rayleigh-Taylor instability. Depending on the size of the domain, complex fronts can appear such as steady curved fronts or chaotic fronts even without fluid flow [106]. Previous work by Elliot and Vasquez established the stability of flat fronts governed by the KS equation under density gradients [53]. However, this work did not analyze the stability of more complex fronts arising in the KS equation [91]. These fronts are not necessarily stable requiring new computational techniques to obtain them, and to analyze their stability under density gradients, which is what we present in this chapter.

We study the effects of the Rayleigh-Taylor instability on steady fronts described by the KS equation. We consider fronts propagating between two infinite vertical plates separated by a small gap, containing two fluids of different densities as shown in Fig. 8.1. In this geometry the fluid flow can be approximated by Darcy's Law in two dimensions. This domain is bounded by two vertical boundaries separated by a distance L, which corresponds to the

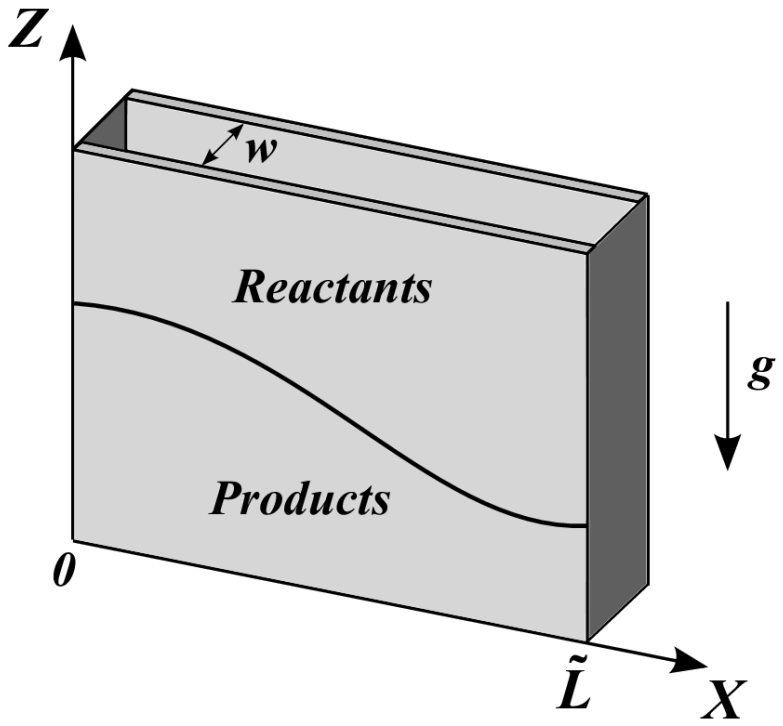

Figure 8.1: Sketch of the propagating front confined in a Hele-Shaw cell.

slab width. As this distance is increased, the KS equation allows for the propagation of different fronts of steady shapes and symmetries. We study the stability of this fronts that propagate with constant speed as convective fluid motion sets in. We first search for steady front solutions then we determine their stability using a linear stability analysis. We consider both cases, one where the denser fluid is placed on top of a less dense fluid and the opposite case. The slab width (L) is essential to study the fronts, since it determines the speed and symmetry of steady solutions of the KS equation. As L is increased, we find that the flat front solution loses stability, allowing for a steady curved front. This solution can be placed side by side, leading to solutions in larger domains consisting of a repeating cell. We obtain the conditions of stability for these cellular structures.

8.1 Equations of motion

We consider a two-dimensional slab confined by two infinite walls located at the coordinates $X=0$ and $X=\tilde{L}$ containing two fluids of different densities, one

above the other as shown in Fig. 8.1. These fluids are separated by a thin interface corresponding to the reaction front. The position of the front at time T is described by the front height $H(X,T)$. The time evolution of the front is provided by the KS equation [Eq. (5.1)] with the addition of the fluid flow

$$\frac{\partial H}{\partial T} = \nu \frac{\partial^2 H}{\partial X^2} + \frac{V_0}{2}\left(\frac{\partial H}{\partial X}\right)^2 - \kappa \frac{\partial^4 H}{\partial X^4} + V_Z\big|_{Z=H}. \tag{8.1}$$

Here, V_Z is the vertical component of the fluid velocity, to be evaluated at the front height H. We also use a reference frame moving at the speed of the flat front V_0. The coefficients ν and κ depend on the particular physical system under consideration. In the case of diffusive instabilities, the parameter ν depends on the ratio of diffusivities of a reactant and an autocatalytic substance. According to Malevanets *et al.* [29], this parameter can be approximated by $\nu = 1 - 7(\delta - 1)/3(\delta + 1)$ with δ being the ratio of their diffusivities. The flat front presents instabilities if $\nu < 0$, which in this approximation corresponds to $\delta > 2.5$.

We use Darcy's law to describe the motion of the fluid inside the slab. In a Hele-Shaw cell, the coefficient of permeability of a porous medium can be approximated by $w^2/12$, where w is the gap width between two vertical walls [107]. With this approximation Eq. (3.18) becomes

$$\vec{V} = -\frac{w^2}{12\mu}\left(\vec{\nabla}P + \rho g \hat{e}_Z\right). \tag{8.2}$$

Here, $\vec{V}$ is the fluid velocity, P is the pressure, g is the acceleration of gravity in the vertical direction, $\hat{e}_Z$ is a unit vector in the vertical direction pointing upward, and μ is the dynamic viscosity.

The fluid density changes abruptly across the interface, therefore we write the fluid density as

$$\rho = \rho_0 + \Delta\rho\Theta(Z - H), \tag{8.3}$$

where Θ is a step function, having a value of one if its argument is positive and zero otherwise. Here ρ_0 is the density of the fluid below the interface, $\Delta\rho$ is the density difference between the two fluids, being positive when the denser fluid is on top. We use the continuity equation, $\vec{\nabla}\cdot\vec{V}=0$, to write the components of the fluid velocity in terms of a stream function $\Psi(X,Z,T)$. As a result, $V_X=-\partial\Psi/\partial Z$ and $V_Z=\partial\Psi/\partial X$. Introducing these relations into Darcy's law, we obtain an equation for the stream function in terms of the front height H

$$\nabla^2\Psi=\frac{w^2 g}{12\mu}\Delta\rho\frac{\partial H}{\partial X}\delta(Z-H). \tag{8.4}$$

The Dirac δ function results from the derivative of the step function. In addition, we use a Taylor expansion for the vertical component of the fluid velocity

$$V_Z\big|_{Z=H}=V_Z\big|_{Z=H_0}+(H-H_0)\left.\frac{\partial V_Z}{\partial Z}\right|_{Z=H_0}. \tag{8.5}$$

The second term in the expansion will be neglected since we are considering only slow flows combined with the small deviations from flat fronts. Assuming that κ is non-zero, we introduce time and length scales defined by $L_x=\sqrt{(\kappa/|\nu|)}$, $L_z=|\nu|/V_0$, and $L_T=\kappa/\nu^2$ as in Sec. 5.1. Using lowercase letters for the corresponding variables in this system of dimensionless units, Eq. (8.1) becomes

$$\frac{\partial h}{\partial t}=\tilde{\nu}\frac{\partial^2 h}{\partial x^2}+\frac{1}{2}\left(\frac{\partial h}{\partial x}\right)^2-\left.\frac{\partial^4 h}{\partial x^4}+\frac{\partial\psi}{\partial x}\right|_{z=h_0} \tag{8.6}$$

and Eq. (8.4) becomes

$$\frac{\partial^2\psi}{\partial x^2}+\beta^2\frac{\partial^2\psi}{\partial z^2}=\beta\mathrm{Ra}\frac{\partial h}{\partial x}\delta(z-h_0). \tag{8.7}$$

Here we have defined the dimensionless numbers $\mathrm{Ra}=\left(w^2 g\Delta\rho/12\mu\right)L_x/\nu$, and $\beta=L_x/L_z$. The value of $\tilde{\nu}$ is either plus or minus one, depending on the original

sign of ν. As in reference [53], we solve Eq. (8.7) by introducing Fourier series on h and ψ

$$\psi = \sum_{n=1} \psi_n(z,t) \sin\left(\frac{n\pi x}{\mathrm{L}}\right) \tag{8.8}$$

and

$$h = \sum_{n=0} H_n(t) \cos\left(\frac{n\pi x}{\mathrm{L}}\right). \tag{8.9}$$

Here the x coordinate varies from 0 to L. These Fourier series satisfy the boundary conditions at the vertical walls [85], corresponding to zero horizontal fluid velocity ($v_x = 0$) and, zero first and third derivatives for the front height with respect to x. The Fourier coefficient $H_0(t)$ corresponds to the average front height h_0. Introducing the Fourier series into Eq. (8.7), we solve for each component of the stream function ψ_n in terms of H_n. Hence we obtain the Fourier components of the stream function [53]

$$\psi_n(z,t) = \begin{cases} (\mathrm{Ra} H_n / 2) e^{-n\pi(z-H_0)/(\beta \mathrm{L})} & \text{if } z > H_0, \\ (\mathrm{Ra} H_n / 2) e^{n\pi(z-H_0)/(\beta \mathrm{L})} & \text{if } z \le H_0. \end{cases} \tag{8.10}$$

Using Eq. (8.10), we replace Eq. (8.8) into Eq. (8.6), which leads to an equation that involves only the front height h, and its Fourier coefficients H_n

$$\frac{\partial h}{\partial t} = \tilde{\nu} \frac{\partial^2 h}{\partial x^2} + \frac{1}{2}\left(\frac{\partial h}{\partial x}\right)^2 - \frac{\partial^4 h}{\partial x^4} + \frac{\mathrm{Ra}}{2} \sum_n \left(\frac{n\pi}{\mathrm{L}}\right) H_n \cos\left(\frac{n\pi x}{\mathrm{L}}\right). \tag{8.11}$$

In our study we only consider the case $\tilde{\nu} = -1$, which allows for unstable flat fronts, and steady stable curved fronts.

8.2 Numerical methods

8.2.1 Stationary solutions

We seek solutions of the form $h(x,t) = h(x) - ct$, where c is the constant velocity of the front. With this substitution (and dropping the prime), Eq. (8.11) becomes

$$-c = -\frac{d^2h}{dx^2} - \frac{d^4h}{dx^4} + \frac{1}{2}\left(\frac{dh}{dx}\right)^2 + \frac{\mathrm{Ra}}{2}\sum_n \left(\frac{n\pi}{\mathrm{L}}\right) H_n \cos\left(\frac{n\pi x}{\mathrm{L}}\right). \qquad (8.12)$$

We chose a reference frame moving with the same constant front velocity c to make the front stationary, being $h(x)$ the spatial front profile in this reference frame and H_n the Fourier coefficients of h. The boundary conditions, zero first and third derivatives for the front height, allows for different solutions up to a constant. We solve Eq. (8.12) using a non-linear shooting method together with a recursive, self-consistent iteration. We transform Eq. (8.12) into a set of four first-order ordinary differential equations (ODEs) by defining each high-order derivative as a new variable. We chose $h = 0$ at $x = 0$, with the choice being arbitrary since adding any constant to a solution will still be a solution. We first find a solution of Eq. (8.12) for $\mathrm{Ra} = 0$. We have two free parameters to start the shooting method and satisfy the remaining boundary conditions at $x = \mathrm{L}$. One of them is the speed c and the other is the second derivative d^2h/dx^2 at the starting point $x = 0$. After giving guessing values to these parameters, we integrate the equations with a simple Euler method to reach $x = \mathrm{L}$. We adjust the parameters to obtain the correct boundary conditions at $x = \mathrm{L}$. Once we have the solution for $\mathrm{Ra} = 0$, we calculate the Fourier coefficients H_n for this solution. We keep these values constant to restart a shooting method with a small chosen value of Ra, which leads to a modified solution of h. We repeat this process until the solution remains unchanged. In this manner, we obtained a solution for nonzero Rayleigh number Ra. The calculations used a 25-term truncation for the Fourier coefficients, obtaining no significant difference in the front speed with fewer terms. We used 10^5 points with the Euler method in the interval $0 \le x \le \mathrm{L}$, a similar calculations using a fourth-order Runge-Kutta

method did not yield significant difference. The front profile is reconstructed from its Fourier coefficients using a spatial grid of 1000 points.

8.2.2 Linear stability analysis

We analyze the stability of the fronts using small perturbations to the stationary state solutions. We introduce in Eq. (8.11) the solution $h(x)$ with the addition of a perturbation $H'(x,t)$, keeping only linear terms the equation becomes

$$\frac{\partial H'}{\partial t} = -\frac{\partial^2 H'}{\partial x^2} - \frac{\partial^4 H'}{\partial x^4} + \left(\frac{\partial h}{\partial x}\right)\left(\frac{\partial H'}{\partial x}\right) + \frac{\mathrm{Ra}}{2}\sum_n \left(\frac{n\pi}{\mathrm{L}}\right) H'_n \cos\left(\frac{n\pi x}{\mathrm{L}}\right). \qquad (8.13)$$

We look for solutions of the form

$$H'(x,t) = e^{\sigma t}\tilde{H}(x), \qquad (8.14)$$

where σ is the growth rate of the perturbation. With this substitution, Eq. (8.13) becomes an eigenvalue equation, with σ the eigenvalue and $\tilde{H}$ the eigenfunction

$$\sigma\tilde{H} = -\frac{d^2\tilde{H}}{dx^2} - \frac{d^4\tilde{H}}{dx^4} + \left(\frac{dh}{dx}\right)\left(\frac{d\tilde{H}}{dx}\right) + \frac{\mathrm{Ra}}{2}\sum_n \left(\frac{n\pi}{\mathrm{L}}\right)\tilde{H}_n \cos\left(\frac{n\pi x}{\mathrm{L}}\right). \qquad (8.15)$$

This equation determines the stability of $h(x)$, since solutions with negative real part of σ will decay with time. Introducing the Fourier series for $h(x)$ and $\tilde{H}(x)$ and projecting over the corresponding cosine function (see appendix A.2), we obtain a linear set of eigenvalue equations on the coefficients $\tilde{H}_p$

$$\sigma\tilde{H}_p = \left(\frac{p\pi}{\mathrm{L}}\right)^2 \tilde{H}_p - \left(\frac{p\pi}{\mathrm{L}}\right)^4 \tilde{H}_p + \sum_m A_{pm}\tilde{H}_m + \frac{\mathrm{Ra}}{2}\left(\frac{p\pi}{\mathrm{L}}\right)\tilde{H}_p \quad \text{for} \quad p \geq 1\ , \qquad (8.16)$$

where

$$A_{pm} = \frac{m}{2}\left(\frac{\pi}{\mathrm{L}}\right)^2 \sum_n n h_n \left(\delta_{|n-m|,p} - \delta_{n+m,p}\right). \qquad (8.17)$$

The eigenvalues and eigenvectors are obtained numerically using the CG subroutine in the EISPACK package [108]. The calculations used 25-term truncation obtaining no significant difference with fewer terms. The front will be stable if all of the eigenvalues have negative real part. Thus, if the eigenvalue with the largest real part is negative, the front is stable.

8.2.3 Fronts evolving in time

In previous sections we obtained steady front solutions using a non-linear shooting. In addition, we determine the stability of these steady solutions. We now look for solutions that evolve with time. We focus on oscillatory and chaotic solutions. We obtain these solutions following the method used in Sec. 6.3.1. Introducing the Fourier series for $h(x,t)$ in Eq. (8.11) and projecting over the corresponding cosine function, we obtain the following set of ordinary differential equations:

$$\frac{dH_n}{dt} = (nq)^2 H_n - (nq)^4 H_n + \frac{q^2}{4}\sum_{\ell=1}\sum_{p=1} \ell p H_\ell H_p \left(\delta_{n,|\ell-p|} - \delta_{n,\ell+p}\right) + \mathrm{Ra}\left(\frac{nq}{2}\right) H_n \quad \text{for} \quad n \geq 1 \tag{8.18}$$

and

$$\frac{dH_0}{dt} = \frac{q^2}{4}\sum_{p=1} p^2 H_p^2. \tag{8.19}$$

Here the parameter q is defined by $q = \pi/\mathrm{L}$, where L is the slab width. We solve this set of equations numerically using an implicit Euler's method described in Sec. 6.3.1.

8.3 Results

8.3.1 Steady solutions

We obtain fronts of steady shape moving with constant velocity for different values of the slab width L. Previous works [42,43] showed that flat fronts

without convection become unstable for widths larger than a critical value that depends on the Rayleigh number Ra. In some cases, the fronts are symmetric with respect to a line parallel to the vertical z direction and passing through the center of the two-dimensional domain at $x = L/2$, we call this line the central axis. We first obtain stationary fronts when the denser fluid is on top ($Ra = 0.5$) for different slab widths. The front profile can be flat, axisymmetric, or nonaxisymmetric depending on the distance L between the vertical walls and the value of the parameter Ra. In Fig. 8.2, we show four different front profiles, with the front height function measured relative to the average front height.

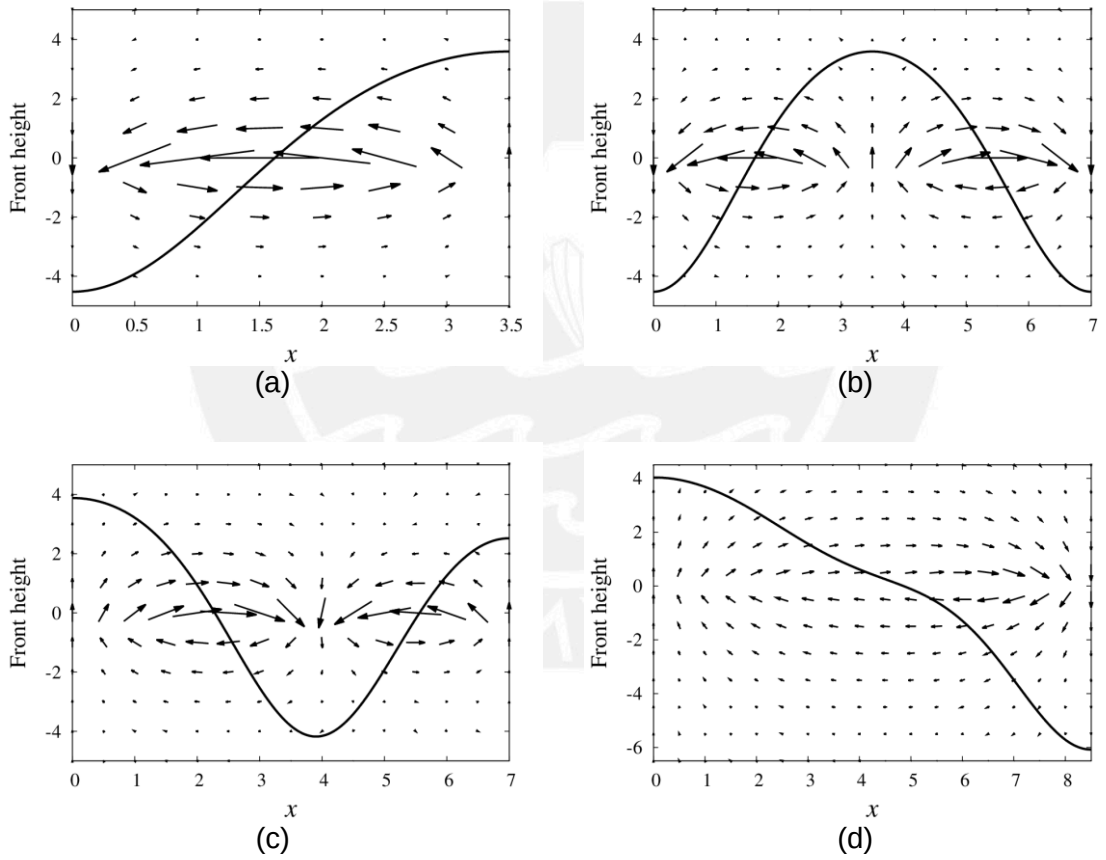

Figure 8.2: Fronts with corresponding fluid velocities inside a Hele-Shaw cell. The front height is measured from the average front height. The Rayleigh number is $Ra = 0.5$, having the denser fluid on top of the less dense fluid. (a) Nonaxisymmetric front with a single convective roll ($L = 3.5$). (b) Axisymmetric front having two convective rolls with fluid going up in the middle and falling near the walls ($L = 7.0$). (c) Nonaxisymmetric front having a minimum, fluid falls near the central axis ($L = 7.0$). (d) Nonaxisymmetric front showing a single convective roll rotating clockwise ($L = 8.5$).

Without fluid motion at $L = 3.5$, a nonaxisymmetric front develops due to the instability of the flat front for $L > \pi$ [see Eq. (4.32)]. This profile has a horizontal density gradient that leads to a single convective roll, which in turns modifies the front, resulting in the structure displayed in Fig. 8.2a. This front is nonaxisymmetric having one side higher than the other side near the wall, the fluid rises on the higher side falling on the opposite side. In Fig. 8.2b, we show a stable axisymmetric front with a single maximum in the center of the slab for $L = 7.0$. This stable axisymmetric front can exist even without fluid flow. When fluid motion is present, density gradients generate two convective rolls in which the fluid rises in the middle and falls near the walls enhancing the position of the front maximum. This maximum takes a value of 3.59 compare to 2.46 without fluid motion. In contrast, Fig. 8.2c shows an unstable nonaxisymmetric front with a minimum near the center of the slab for $L = 7.0$. The fluid falls near the central axis and rises near the walls. Figure 8.2d displays another unstable nonaxisymmetric front with three inflection points and a single convective roll, but without relative maximum or minimum ($L = 8.5$). The flat front is also a solution for these values of L. All these fronts have steady shape, each moving at different constant velocities. We will analyze the stability of these types of fronts in detail in Sec. 8.3.2.

In the case of having fronts separating the reactants with a denser fluid on top of a less dense fluid ($Ra > 0$), buoyancy forces provide an additional mechanism to destabilize the front. We obtain stationary fronts in a reference frame co-moving with the front for different values of the domain width L, while keeping the value of the Rayleigh number constant ($Ra = 0.5$). We show in Fig. 8.3, the velocities of these fronts relative to the velocity of the flat front as a function of L. The fronts shapes and velocities were obtained using Eq. (8.12), while their stabilities are determined from the growth rates using Eq. (8.16). We will compare this figure with the results of Chap. 5 (see Fig. 5.4 and Fig. 5.5) that provides the front velocities and corresponding conditions of stability without fluid flow ($Ra = 0$). We will focus on how these front velocities are affected by changing the Rayleigh number (Ra). In Fig. 8.3, the flat front has velocity equal to zero, being always a solution regardless of the value of L.

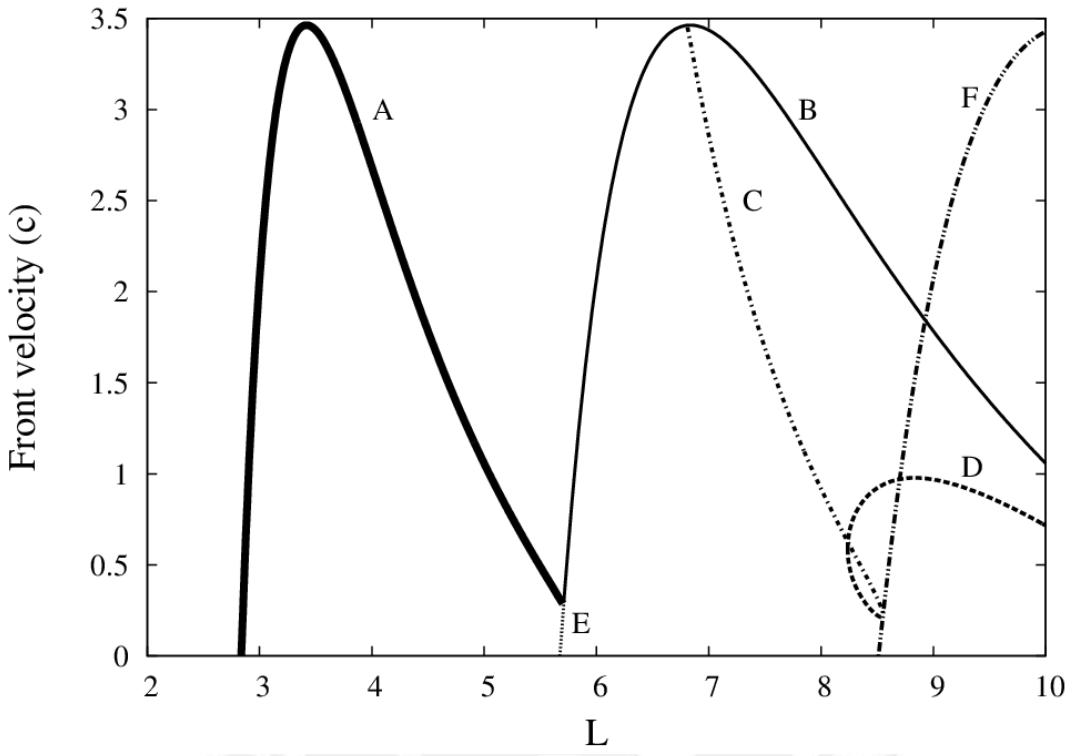

Figure 8.3: Front velocities relative to the flat front for different distances between the walls (L). The Rayleigh number is Ra = 0.5. The thick solid line (A) corresponds to stable nonaxisymmetric fronts. The solid line (B) corresponds to stable axisymmetric fronts. The dashed line (E) corresponds to unstable axisymmetric fronts. Broken lines (C, D, and F) correspond to unstable nonaxisymmetric fronts.

The flat front becomes unstable for $L > 2.83$, a value smaller than the critical width for instability without density differences ($L = \pi$) indicating the destabilizing effect of buoyancy. Branches A and B correspond to the velocity of nonaxisymmetric and axisymmetric solutions, respectively. These branches meet each other at $L = 5.71$. The solutions of these branches are stable, reaching both branches a maximum speed of 3.46 in contrast to the maximum speed of 1.60 obtained without density differences (see Fig. 5.4). The symmetry of Eq. (8.12) implies that the reflection of a nonaxisymmetric solution about the central axis is also a solution with the same velocity. In addition, the central axis splits axisymmetric solutions in branch B into two mirrored nonaxisymmetric solutions corresponding to branch A. For this reason, branches A and B have the same maximum speed. Branch B also contains two solutions, for each value of L, with the same velocity. These solutions are concave downward (having a

maximum) and concave upward (having a minimum), with the concave downward solutions stable. The solutions in branch E are also axisymmetric, but they are unstable. These solutions coexist with those of branch A in the interval $5.67 < L < 5.71$. Branches C, D, and F correspond to the velocities of other unstable nonaxisymmetric solutions. Branch C meets branch B near the top, but its velocity decreases as width L increases, until it finally meets branch F at $L = 8.55$. Branch F begins in $L = 8.51$, having higher velocities for larger values of L. It meets branch D in two points. One of these points is near the maximum speed of branch D, which has solutions with two different velocities for each value of L in the interval $8.24 < L \leq 8.54$.

We also study propagating fronts where the less dense fluid is on top of the denser fluid ($Ra < 0$). We show in Fig. 8.4, the velocities of stationary fronts relative to the velocity of the flat front for different values of the domain width L, while keeping the value of the Rayleigh number constant ($Ra = -0.5$). The transition from stable flat front solutions to stable nonaxisymmetric front solutions (branch A) occurs at $L = 3.74$, here buoyancy forces contribute to stabilize the flat front since the transition without fluid flow takes place at $L = \pi$ (see Fig. 5.4). The maximum speed of nonaxisymmetric solutions (branch A) and axisymmetric solutions (branch B) is the same, but it is almost ten times smaller than the previous case with $Ra = 0.5$ (see Fig. 8.3). These branches meet each other at $L = 7.51$. Branch B also contains two solutions with the same velocity, one being concave downward and the other concave upward. Nonaxisymmetric solutions described by branches C, D, and F, are unstable. Branch C meets branch B near its maximum, then its velocity decreases as width L increases until it meets branch F at $L = 11.25$. Branch D meets branch C at $L = 11.23$ and branch F at $L = 11.26$. Branch F increases its speed faster than D as L increases, but not as fast as in the case without density differences. As a result, when the less dense fluid is on top of a denser fluid, the speed of the stationary fronts decreases.

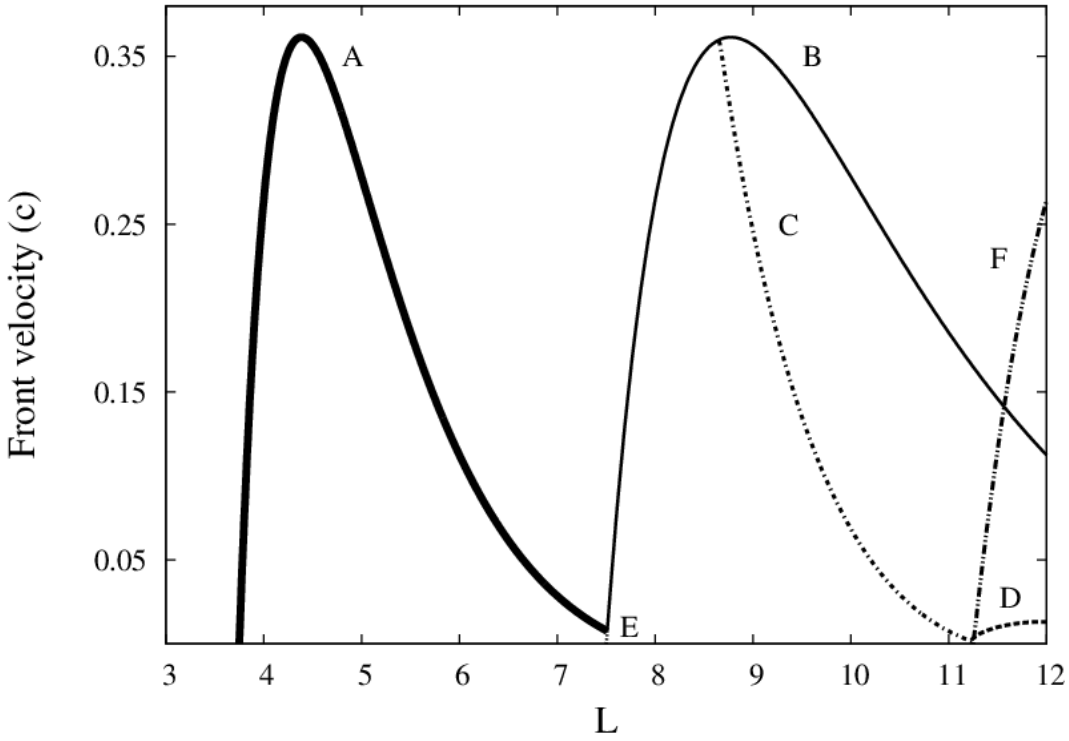

Figure 8.4: Front velocities for different distances between the walls (L). The Rayleigh number is $Ra = -0.5$. The thick solid line (A) corresponds to stable nonaxisymmetric fronts. The solid line (B) corresponds to stable axisymmetric fronts. The dashed line (E) corresponds to unstable axisymmetric fronts. Broken lines (C, D, and F) correspond to unstable nonaxisymmetric fronts.

8.3.2 Stability analysis

We determine the stability of the steady fronts by calculating the growth rate σ for small perturbations to the fronts using Eq. (8.16). The front is unstable when the largest real part of the growth rate $\mathrm{Re}(\sigma)$ is positive since the perturbations will grow exponentially. The results of the linear stability analysis of the stationary fronts whose velocities were shown in Fig. 8.3 are summarized in Fig. 8.5. These stationary fronts were obtained with $Ra = 0.5$ (a denser fluid on top). Flat front solutions (branch G) are unstable except for $L < 2.83$, where they are the only solutions, because their values of $\mathrm{Re}(\sigma)$ are negative. The nonaxisymmetric solutions associated with branch A are stable because all their values of $\mathrm{Re}(\sigma)$ are also negative. There are two axisymmetric solutions with the

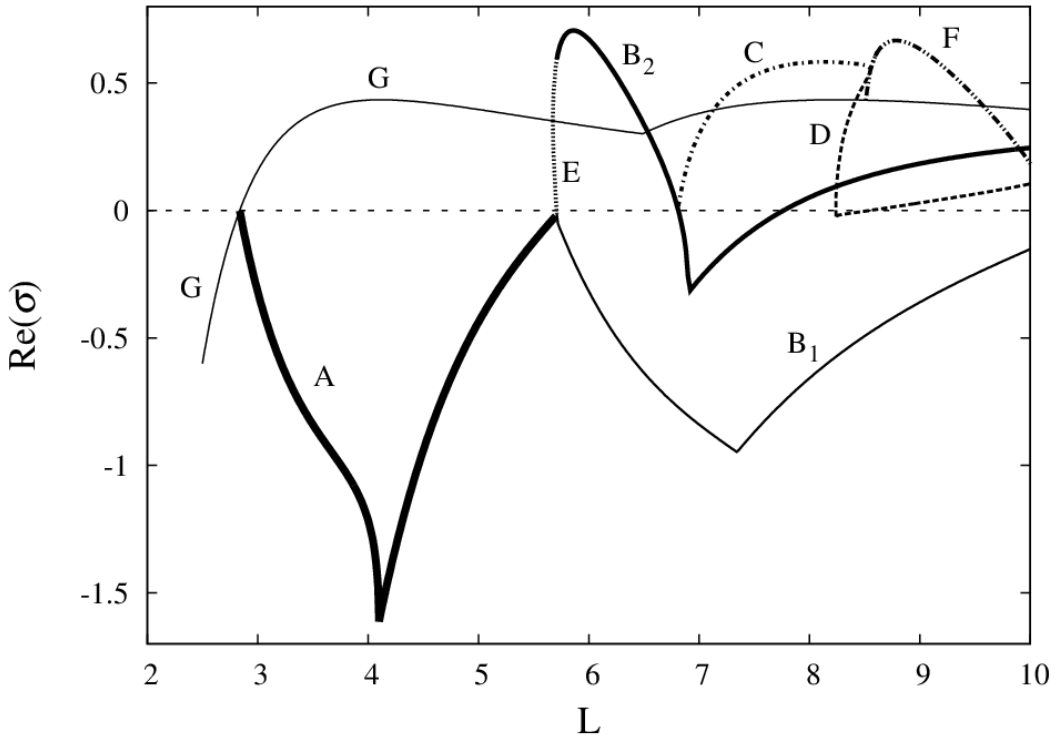

Figure 8.5: The largest real part of the eigenvalues σ for different distances L between walls. The Rayleigh number is $Ra = 0.5$. The front is unstable when the largest real part of the eigenvalues σ is positive. The thickest solid line (A) corresponds to nonaxisymmetric fronts. Solid line B_1 corresponds to concave downward axisymmetric fronts and solid line B_2 corresponds to concave upward axisymmetric fronts. Broken lines (C, D, and F) correspond to nonaxisymmetric fronts. The dashed line (E) corresponds to other axisymmetric fronts. Solid line G corresponds to flat fronts.

same propagation velocities for each value of L in the domain under consideration. These solutions can be concave downward or concave upward, and their real parts of their growths rates are represented by lines B_1 and B_2, respectively. Fig. 8.5 shows a region of bistability for these axisymmetric solutions in the interval $6.82 < L < 7.76$. This region is 20% shorter than the other obtained in Chap. 5 without density differences (see Fig. 5.5). Branch E corresponds to the region where these two concave downward and concave upward axisymmetric solutions are unstable. Branches C, D, and F are associated with distinct nonaxisymmetric solutions. All these solutions are unstable, except for branch D in the range $8.24 < L < 8.54$, where these values are negative. The corresponding fronts to branch D without convection were unstable (see Fig. 5.5); consequently, the denser fluid on top of a less dense

one results in stabilizing unstable nonaxisymmetric fronts in this narrow range. It also increased the front propagation speed. Moreover, increasing the magnitude of Ra beyond $Ra = 0.5$ increases the region of stability of branch D.

We also calculate the stability of the steady fronts with velocities shown in Fig. 8.4. These fronts were obtained with $Ra = -0.5$ (less dense fluid on top). We show the results of the largest real part of the growth rate $Re(\sigma)$ for front perturbations in Fig. 8.6. Flat front solutions associated with branch G are stable for $L < 3.74$. They are the only solutions in this range. Nonaxisymmetric fronts (branch A) also increase its range of stability in contrast to the case without density differences (see Fig. 5.5). However, its values of $Re(\sigma)$ have smaller magnitudes. The real parts of growth rates of concave downward and concave

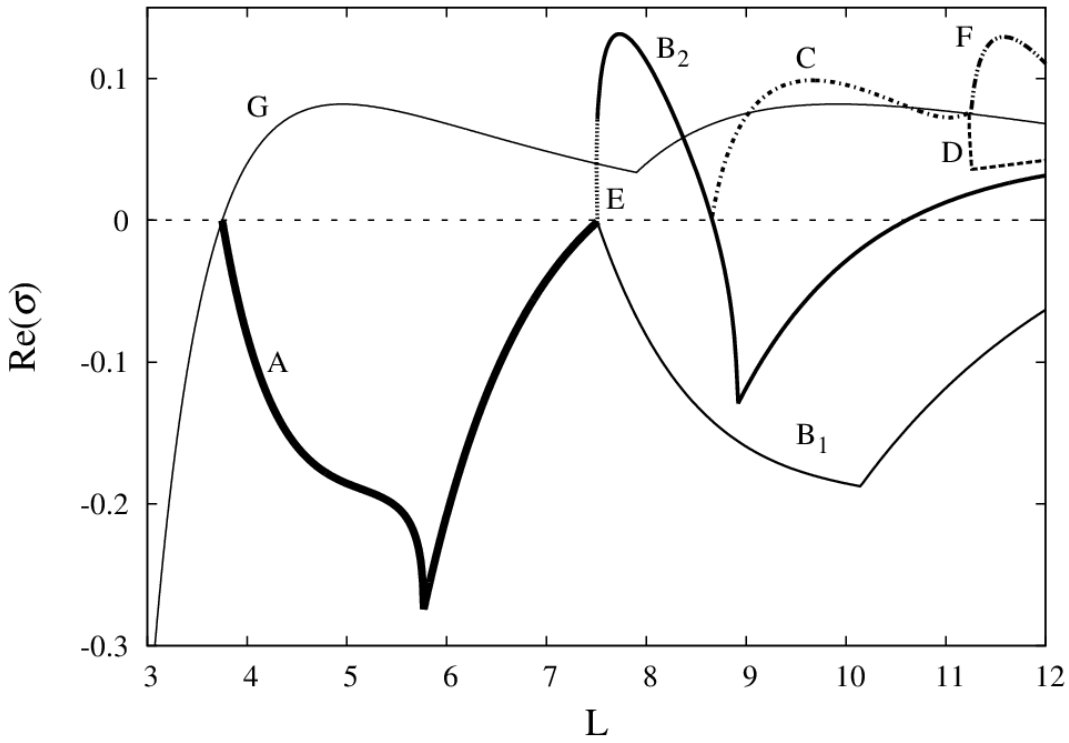

Figure 8.6: The largest real part of the eigenvalues σ for different distances L between walls. The Rayleigh number is $Ra = -0.5$. The front is unstable when the largest real part of the eigenvalues σ is positive. The thickest solid line (A) corresponds to nonaxisymmetric fronts. Solid line B_1 corresponds to concave downward axisymmetric fronts and solid line B_2 corresponds to concave upward axisymmetric fronts. Broken lines (C, D, and F) correspond to nonaxisymmetric fronts. The dashed line (E) corresponds to other axisymmetric fronts. Solid line G corresponds to flat fronts.

upward axisymmetric fronts are represented by lines B_1 and B_2. These axisymmetric solutions have the same propagation velocity. However, the concave downward solution is always stable in the domain ($L > 7.51$), whereas the concave upward fronts are stable in the interval $8.66 < L < 10.60$, becoming a region of bistability. The size of this region is almost two times greater than the one obtained with the denser fluid on top of the less dense fluid ($Ra = 0.5$). The nonaxisymmetric solutions associated with branches C, D, and F are unstable, but their maximum magnitudes of $\mathrm{Re}(\sigma)$ have also decreased. Consequently, having the less dense fluid on top of the denser fluid increases the region of bistability of axisymmetric fronts, but decreases the magnitude of the negative values of the growth rates.

The formation of different types of steady front depends on the values of the Rayleigh number and the domain length L. In Fig. 8.7, we display the corresponding values that lead to steady axisymmetric and nonaxisymmetric fronts. The nonaxisymmetric fronts correspond to solutions displayed as branch A in Fig. 8.3, they have a higher side near the wall with a single convective roll. There are two types of axisymmetric fronts associated with branch B, one is concave downward (branch B_1) and the other is concave upward (branch B_2). For large enough values of Ra and small values of L, we find stable flat fronts. Increasing L leads to the formation of nonaxisymmetric fronts (branch A), while increasing it further leads to axisymmetric fronts (branch B_1). However, for $Ra < -0.65$, this behavior is no longer observed, while increasing L allows the formation of nonaxisymmetric fronts, increasing L further leads to steady stable flat fronts instead of axisymmetric fronts. We also observe a region of bistability between concave upward and concave downward axisymmetric fronts, this region of bistability clearly increases when $Ra < -0.65$. Eventually, all curve fronts vanish at $Ra = -0.769$, having only stable flat fronts. We observe larger regions of stability for nonaxisymmetric and axisymmetric fronts when the less dense fluid is on top.

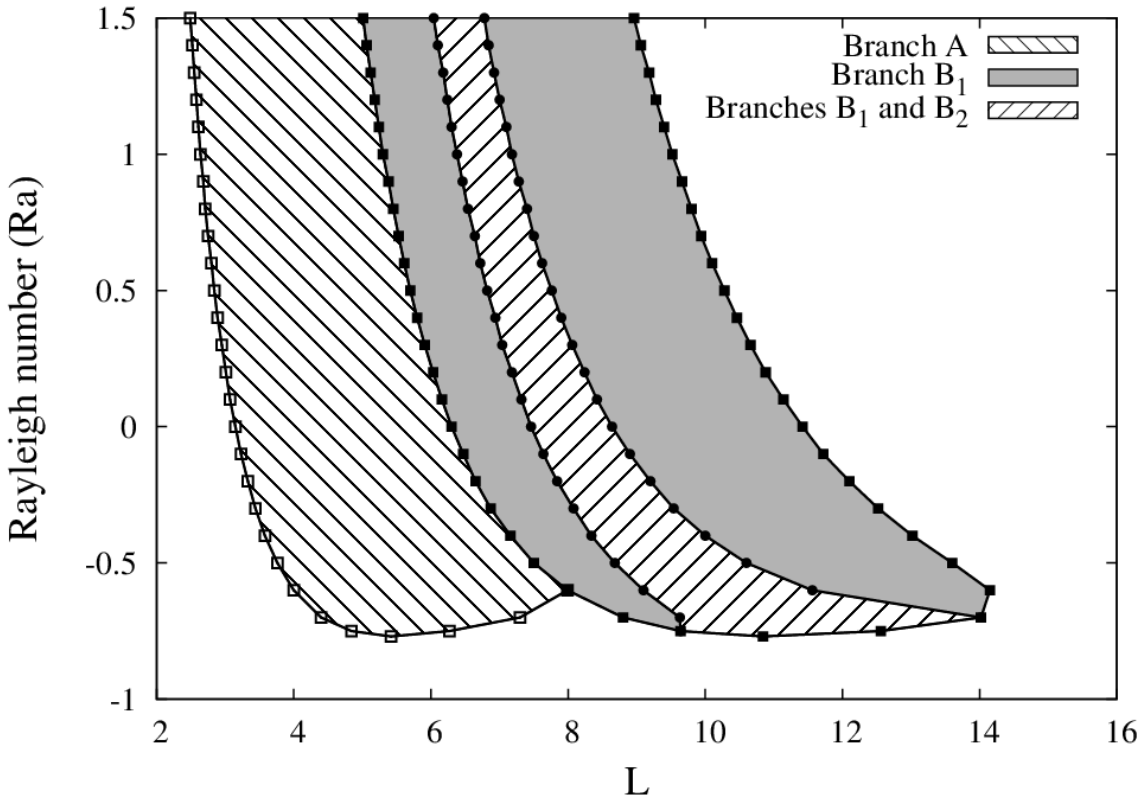

Figure 8.7: Regions of stability for nonaxisymmetric fronts (branch A) and axisymmetric fronts (branches B_1 and B_2), for different values of the Rayleigh number (Ra) and the domain length L. The region of stable axisymmetric fronts is bounded by open squares. The region bounded by dark squares corresponds to stable concave downward axisymmetric fronts (branch B_1), while the region bounded by dark circles corresponds to a bistability region between concave downward and concave upward axisymmetric fronts (B_2).

8.3.3 Cellular solutions

We calculate the stability of larger patterns constructed by placing side by side front solutions developed in smaller cells. This construction is similar to the one used in Sec. 5.3.3 to study fronts without convection. We want to study the effects of convective flow on extended patterns. In Fig. 8.8, we show the velocities corresponding to cellular patterns for different values of the Rayleigh number. Branches A, C and E correspond to nonaxisymmetric solutions, whereas branches B and D correspond to axisymmetric solutions. Solid lines correspond to stable fronts, while broken lines correspond to unstable fronts. Fig. 8.8a displays the velocities of cellular patterns when the denser fluid is on top with Ra = 0.5. Although all the branches have the same maximum speed,

this maximum speed is greater than the case without convection (see Fig. 5.7). We also observe that the location of the speed maximum for the smallest cell is $L_1 = 3.42$, which is smaller than the case without convection. The transition from flat front to a nonaxisymmetric stable solution appears for $\mathrm{L} > 2.83$. This value is smaller than the case without convection, indicating the destabilizing effect of the Rayleigh-Taylor (RT) instabilities on flat front solutions. There are two solutions related to branch B with the same velocity for each value of L. The region of stability of concave downward axisymmetric fronts is greater than the concave upward axisymmetric fronts. However, they share a region of bistability. The solid line in branch B means that at least one of these two solutions is stable. Thus, for $\mathrm{L} > 10.28$ the solutions are unstable and they are represented by a broken line. This value is also smaller than the case without convection. In the case of branch D, there are two axisymmetric solutions with the same velocity for each value of L in their respective domain. These solutions have a maximum or minimum in the central axis, but they share the same interval of stability, namely $13.65 < \mathrm{L} < 15.12$. The length of this interval is smaller compared with the case without convection. The nonaxisymmetric solutions associated with branch C, also have two solutions with the same velocity for each value of L in their respective domain. However, one of these solutions is the reflection of the other about the central axis. Therefore, these solutions have the same maximum value of the real part of their growth rates. Branches A and E, which are also related to nonaxisymmetric solutions have the same behavior. However, these branches A, C and E have different conditions of stability. The length of stability of these branches is reduced due to the positive density gradient. Thus, the RT instabilities increase the maximum speed of the fronts, but decrease the range of stability of the fronts due to the destabilizing effect of the positive density gradient on the fronts.

We study the formation of cellular structure with the less dense fluid on top of the denser fluid for $\mathrm{Ra} = -0.5$. We show the front velocities as a function of L in Fig. 8.8b. Although all the branches have the same maximum speed, this maximum speed is smaller than the previous case, where the denser fluid was on top. Each new cellular structure appears at a length that is an integer number of the smallest cell length. We also notice that these lengths take place

at larger values of L compared to the values for positive Rayleigh numbers, thus indicating the stabilizing effect of the density gradient (less dense fluid on top). Nonaxisymmetric solutions (branch A) are stable. Concave downward axisymmetric fronts represented by branch B, become stable for $L > 13.62$. They share a region of bistability with concave upward fronts, which have a small region of stability. Branch C corresponds to nonaxisymmetric solutions formed by three cells, they share a region of bistability with the axisymmetric fronts solutions of branch B. Branch D is associated with other axisymmetric solutions with the same velocity, having a central maximum (or minimum). The range of stability of these types of fronts is greater than the previous case ($Ra = 0.5$), but the absolute value of the real part of the growth rates decreases as L increases, indicating a slower decay for small perturbations.

To study the stabilizing effects of a density gradient with the less dense fluid on top, we reduce the value of the Rayleigh number to $Ra = -0.75$, obtaining the velocities of stationary fronts for different values of the domain width L (Fig. 8.8c). The maximum speed of the fronts is much smaller than the previous two cases. In contrast with those cases, where the flat front is always unstable after a critical value of the length L, here the flat front is unstable in separated intervals. For example, it becomes unstable at $L = 4.82$, but then is stable at $L = 6.28$, becoming unstable once again at $L = 9.64$. Increasing beyond a large value of L, the intervals of stability disappear, being the flat front unstable. Therefore increasing the magnitude of the Rayleigh number with the less dense fluid on top of the denser fluid increases the regions of stability of flat front solutions, also diminishing significantly the maximum speed of the stationary fronts. While in previous cases we have two different axisymmetric solutions sharing the same speed but with different ranges of stability, here we find that they also share the growth rates. This happens because with $Ra = -0.75$, one of the two fronts is the reflection of the other about the average front height, which is not the case for $Ra = -0.5$. Each of the structures from A to E, present a minimum for the real part of the growth rate, with this minimum being almost the same for structures containing different cells. This did not occur with the previous values of the Rayleigh number. The stabilizing effect of $Ra = -0.75$ led not only to more

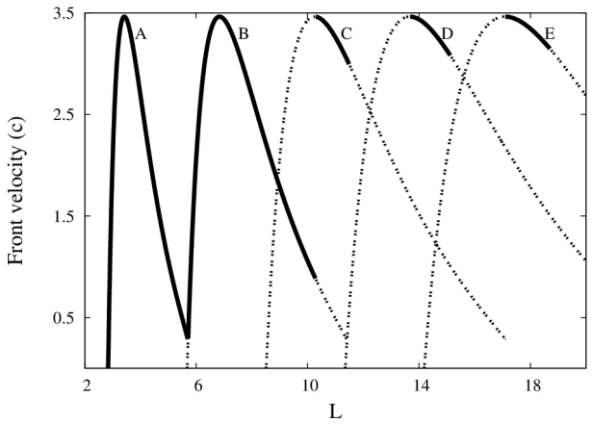

(a)

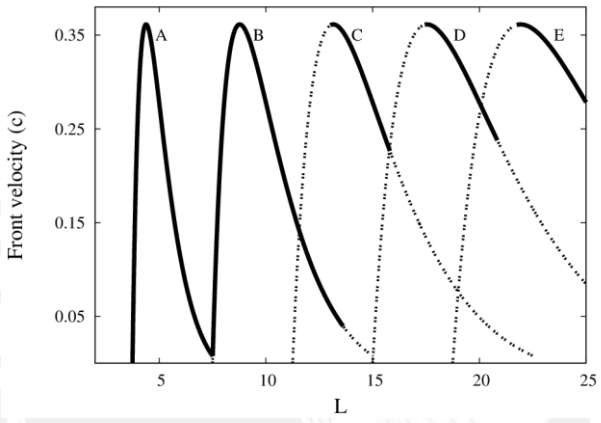

(b)

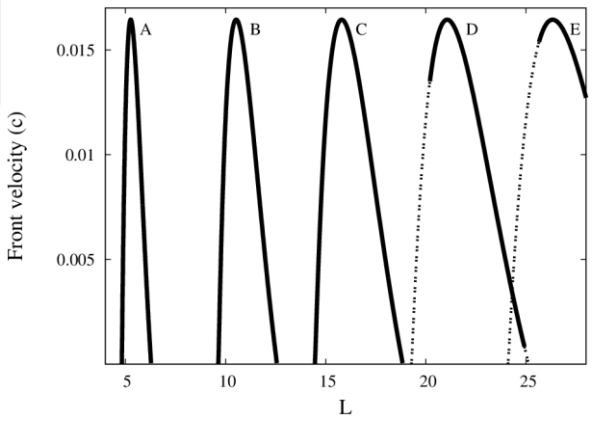

(c)

Figure 8.8: Front velocities for different distances between the walls (L). Solid lines correspond to stable fronts; broken lines correspond to unstable fronts. Lines A, C, and E correspond to distinct nonaxisymmetric fronts, whereas lines B and D correspond to distinct axisymmetric fronts. The respective Rayleigh numbers are (a) $\mathrm{Ra} = 0.5$, (b) $\mathrm{Ra} = -0.5$, and (c) $\mathrm{Ra} = -0.75$.

stable flat fronts, but also provided a stabilizing mechanism for extended patterns in larger domains. If we continue to increase the magnitude of the Rayleigh number beyond $\mathrm{Ra} = -0.769$, we find only the flat front as a solution, without cellular structures, which is consistent with the linear stability analysis of the flat fronts [53].

8.3.4 Period-doubling transition to chaos

We show in Fig. 8.9 the period-doubling bifurcations when the denser fluid is on top ($\mathrm{Ra} = 0.1$). The oscillation starts at $\mathrm{L} = 8.431$ whereas the oscillation without convection occurs at $\mathrm{L} = 8.653$ (see Fig. 6.12). This oscillation is represented in the graph by two points corresponding to the relative maximum and minimum values of the front velocity. These values decrease gradually with increasing L, until the oscillation splits again. As we continue increasing L, the bifurcations come faster and the system turns chaotic. The chaos remains until we reach $\mathrm{L} = 8.791$, where the system achieves a stable steady solution. We observe a slight increase in the chaotic region compared with the case without convective fluid flow (see Fig. 6.11). We show in Fig. 8.10 the period-doubling bifurcations when the less dense fluid is on top ($\mathrm{Ra} = -0.1$). The oscillatory behavior starts at $\mathrm{L} = 8.903$ and the system achieves a stable steady solution at $\mathrm{L} = 9.295$. The region of chaos is slightly smaller than the one obtained without convection (see Fig. 6.11). However, a positive Rayleigh number decreases the length of the interval where we can find solutions that evolve in time (i.e. oscillatory and chaotic solutions) without convection, while a negative Rayleigh number increases the length of this interval. Therefore, the Rayleigh-Taylor instability (denser fluid on top) increases the chaotic region, but decreases the whole range of the non-steady solutions. For greater values of L, we also find solutions that evolve in time. The results are summarized in Table 8.1. In this table we show the intervals of the oscillatory solutions with positive and negative values of the Rayleigh number, and their respective regions of chaos. For $12.827 < \mathrm{L} < 13.372$, we obtained oscillatory solutions without convection. A positive Rayleigh number shifts the beginning of the interval to lower values of L, while a negative Rayleigh number shifts the beginning of the interval to

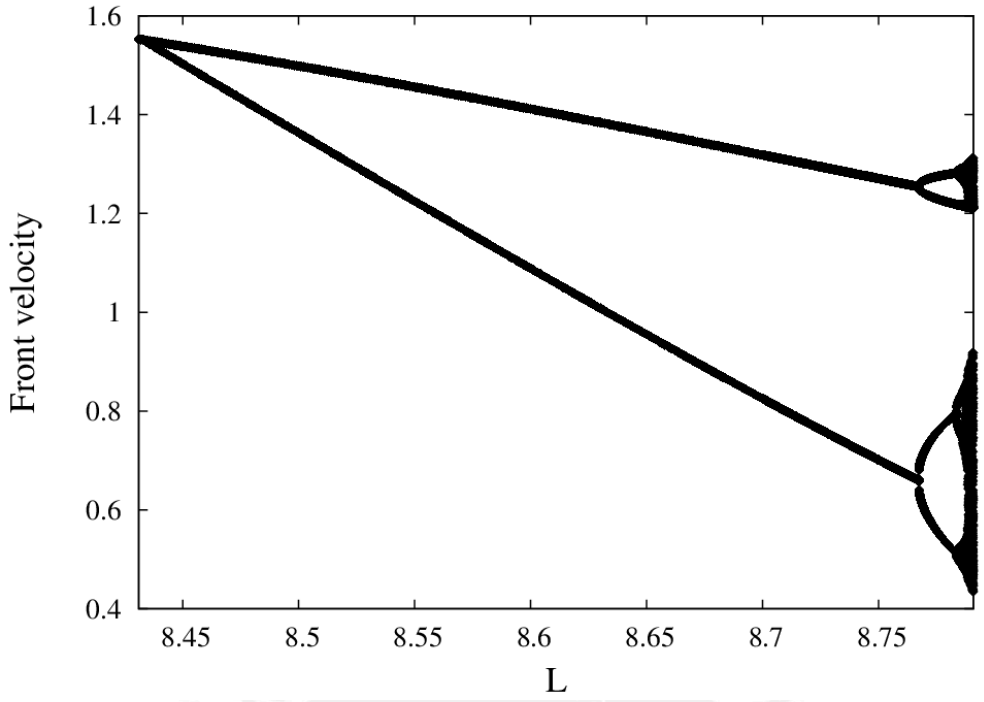

Figure 8.9: Bifurcation diagram when the denser fluid is on top ($\mathrm{Ra} = 0.1$). Here we show the relative maximum and minimum of the time evolution of the front velocity. The period-doubling bifurcations increase as we increase the distance L between plates.

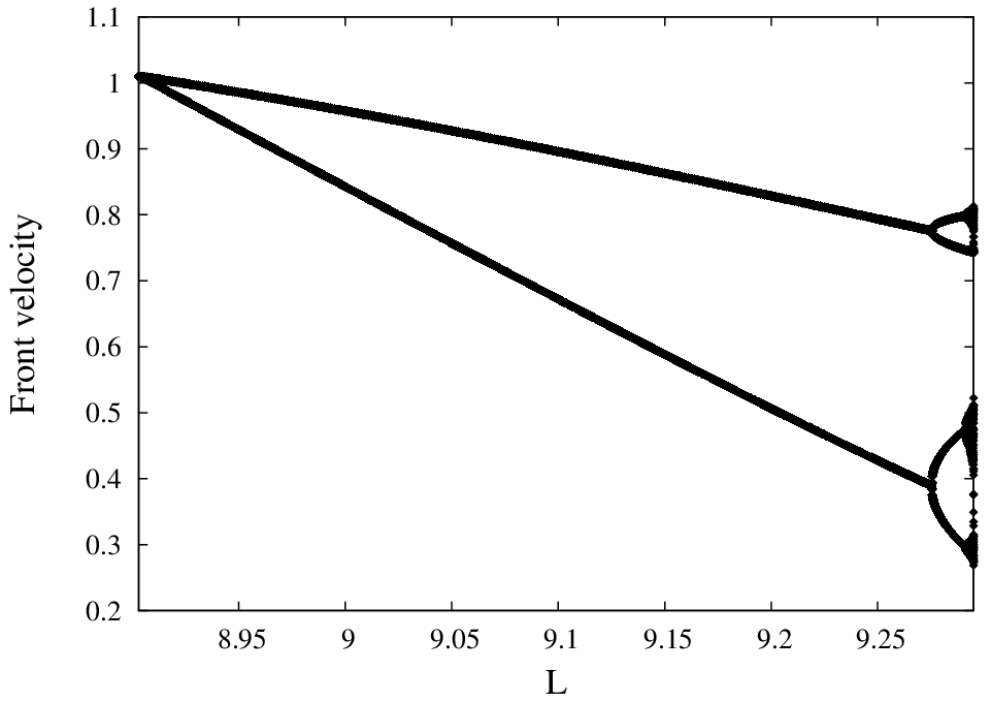

Figure 8.10: Bifurcation diagram when the less dense fluid is on top ($\mathrm{Ra} = -0.1$). Here we show the relative maximum and minimum of the time evolution of the front velocity. The period-doubling bifurcations increase as we increase the distance L between plates.

Description of the solutions	Negative Ra ($Ra = -0.1$)	Without convective flow ($Ra = 0.0$)	Positive Ra ($Ra = 0.1$)
Oscillatory	$13.205 < L < 13.788$	$12.827 < L < 13.372$	$12.50 < L < 13.015$
Oscillatory	$16.061 < L < 16.614$	$15.777 < L < 16.265$	$15.515 < L < 15.956$
Oscillatory	$17.378 < L < 18.648$	$16.878 < L < 18.140$	$16.444 < L < 17.619$
Chaotic	$18.648 < L < 19.122$	$18.140 < L < 18.384$	$17.619 < L < 17.893$
Oscillatory	$19.122 < L < 19.193$	$18.384 < L < 19.317$	$17.893 < L < 19.264$
Chaotic	$19.193 < L < 20.528$	$19.317 < L < 19.801$	$19.264 < L < 19.696$
Oscillatory	$20.528 < L < 21.907$	$19.801 < L < 20.424$	$19.696 < L < 19.907$
Chaotic	$21.907 < L < 22$	$20.424 < L < 20.570$	$19.907 < L < 20.254$
Oscillatory		$20.570 < L < 21.289$	$20.254 < L < 20.708$
Chaotic		$21.289 < L < 22$	$20.708 < L < 21.73$
Oscillatory			$21.73 < L < 22$

Table 8.1: Window range of the oscillatory and chaotic solutions for greater values of the distance L between plates ($12 < L < 22$)

greater values of L. However, a positive Rayleigh number decreases the length of the interval of the oscillatory solutions, while a negative Rayleigh number increases the window range of the oscillatory solutions. A similar result occurs to the oscillatory region without convection located at $15.777 < L < 16.265$. For greater values of L, we observe a wide region of spatio-temporal behavior. In addition, the Rayleigh-Taylor instability revealed a new region of oscillatory behavior. Therefore the Rayleigh-Taylor instability shifts the beginning of the window range of the non-steady solutions to lower values of L, while a negative Rayleigh number (less dense fluid on top) shifts them to greater values of L.

8.4 Summary

We studied thin reaction fronts moving across density gradients within a two-dimensional slab using the KS equation with the addition of fluid flow. Without fluid flow, we observe transitions as we increase the slab width L: from flat to nonaxisymmetric fronts, and from nonaxisymmetric to axisymmetric fronts. Including density gradients, flat fronts can remain convectionless in small domains, while the originally curved fronts will generate convective fluid motion due to their horizontal density gradient. We find similar transitions between fronts as we vary the slab width L for $Ra = 0.5$, however the transitions to new solutions take place at different values of L. In the case of $Ra = -0.5$, the transitions occur at larger values, indicating the stabilizing effect of the negative density gradient. However, for $Ra = -0.75$, we found that the flat front is stable in separated intervals. That is, it is stable for $L < 4.82$ and it is stable once again in the interval $6.28 < L < 9.64$, and so on. Therefore the stabilizing effect of the negative density gradient for flat front solutions increases as the Rayleigh number becomes more negative. In addition, we found for $Ra = -0.75$ extended patterns for larger values of the slab width L.

The transition from nonaxisymmetric to axisymmetric front profiles depends on the slab width L and the dimensionless Rayleigh number Ra. We also find stable axisymmetric fronts that have a minimum (concave downward fronts) sharing a small region of bistability with concave upward fronts. This region of bistability increases when the less dense fluid is on top, but the front propagation velocity decreases.

We also show that fluid motion contributes to define the front shape. In the case of axisymmetric front profiles, for larger values of Ra, the maximum front height increases with respect to the front height without convection since fluid will tend to rise through the middle of the slab. On the contrary, for negative values of Ra the maximum front height decreases since the fluid motion is opposite, with falling fluid near the axis. We also analyzed the stability of fronts in extended domains arising from placing together solutions in smaller domains, or cells. We find that negative Rayleigh numbers can increase the domain of stability of these structures. However, there is a lower limit for the Rayleigh

number ($\mathrm{Ra} = -0.769$) below which these cellular structures no longer appear, where the only solutions correspond to stable flat fronts. In addition, we study the effects of convective fluid flow on oscillatory and chaotic solutions. We find that the Rayleigh-Taylor instability (positive Rayleigh number) shifts the beginning of the window range of the solutions that evolve in time to lower values of L, while a negative Rayleigh number (less dense fluid on top) shifts them to greater values of L.

Chapter 9

Conclusions

A fluid flow in which a chemical reaction takes place can be found in a diversity of fields such as combustion, catalysis, and chemical vapor deposition process used in many thin film applications [109]. In this work, we have studied the effects of different types of fluid motion on steady reaction fronts described by the Kuramoto-Sivashinsky (KS) equation. These fronts described by the KS equation can result in steady curved fronts as they propagate in two-dimensional domains. Transitions between these structures take place as the width of the domain is modified. We have focused especially in the analysis of the stability of complex fronts arising in the KS equation. We have identified branches of unstable fronts that can turn into stable branches in the presence of fluid motion.

We first studied the effects of an external Poiseuille flow on reaction fronts; we later contrasted our results with the application of an external Couette flow. Finally, we studied a reaction front separating fluids of different densities which may result in Rayleigh-Taylor instabilities as a less dense fluid is placed under a denser fluid. We also considered fronts in extended domains generated from solutions in smaller domains or cells. The main findings may be listed as follows:

1. Without external fluid flow, the reaction fronts described by the KS equation exhibit transitions from a nonaxisymmetric to an axisymmetric profile. This transition can be observed by changing the slab width. Adding a Poiseuille flow will change the shape and speed of the fronts and make these transitions occur at different widths. (Chapter 6).

2. Strong supportive Poiseuille flows will make nonaxisymmetric fronts disappear. In addition, stable steady fronts propagating in the presence of an adverse Poiseuille flow will be axisymmetric for slow fluid flows, but for higher speeds the adverse flow can lead to stable nonaxisymmetric fronts (Sec. 6.2).

3. In the case of Couette flow, the maximum speed of stable nonaxisymmetric fronts with a higher side at the moving plate is favor by the increment of the relative velocity between the plates. While the other stable nonaxisymmetric fronts tend to decrease their maximum speed until they eventually disappear. Thus, we can observe the separation of these branches related to nonaxisymmetric fronts when a Couette flow is applied (Chapter 7).

4. We can affect the symmetry and speed of the originally axisymmetric fronts (without external fluid flow) by applying a Couette flow. These fronts become nonaxisymmetric with a relative maximum or minimum (Sec. 7.1).

5. Convective fluid motion takes place changing the shape and speed of the fronts. In the case of curved fronts, convection always exists due to a horizontal density gradient, even if the less dense fluid is on top. For positive values of the Rayleigh number, the maximum front height increases, whereas for negative values this maximum height decreases (Sec. 8.3.1).

6. A favorable density gradient can provide stability to an extended pattern. These fronts in extended domains are generated from solutions in smaller domains or cells (Sec. 8.3.3).

7. The Rayleigh-Taylor instability (where the less dense fluid is below a denser fluid) decreases the window range of the non-steady solutions compared with the case without convective fluid flow. In the opposite case (where the less dense fluid is on top), the length of this interval increases (Sec. 8.3.4).

The experimental observation of the effects of the Poiseuille flow on reaction fronts will require fronts that are potentially unstable in systems such as reaction-diffusion fronts [24] or flame instabilities [110]. In the case of advection

due to Couette flow, experiments with fronts having diffusive instabilities can show these new structures. We can generate this flow using a moving wall confining a fluid layer. We also study thin reaction fronts moving across density gradients within a two-dimensional slab. As in the previous cases, we have presented a theory based on the KS equation, which can be applied to different physical situations. Its simplicity allowed us to track and analyze some complex fronts. We found stable convective fronts with extended structures under favorable density gradients, they may also be found in similar systems (either experimentally or theoretically), such as reaction-diffusion-convection systems with diffusive instabilities.

Appendix A

A.1 Derivation of the Kuramoto-Sivashinsky equation

We present a derivation of the Kuramoto-Sivashinsky equation based on the work of Malevanets *et al.* [29] for the case of small-amplitude perturbations. A general reaction-diffusion equation in one dimension is given by

$$\frac{\partial \mathbf{z}}{\partial t} = \boldsymbol{F}(\mathbf{z}) + \boldsymbol{D}\nabla^2 \mathbf{z}, \tag{A.1}$$

where $\mathbf{z}$ is a vector of concentration of the components of the system, $\boldsymbol{F}(\mathbf{z})$ is a vector-valued function describing chemical reactions and $\boldsymbol{D}$ is the diffusion matrix which is assumed diagonal. We also assume that in one dimension Eq. (A.1) has a stable solution with a propagating front profile $\mathbf{z} = \mathbf{z}_0(x - ct)$, where c is the velocity of the front. Working in a reference frame co-moving with the front Eq. (A.1) becomes

$$\frac{\partial \mathbf{z}}{\partial t} = \boldsymbol{F}(\mathbf{z}) + \boldsymbol{D}\nabla^2 \mathbf{z} + c\frac{\partial \mathbf{z}}{\partial \xi}. \tag{A.2}$$

Here $\xi = x - ct$ and the corresponding stable solution in one dimension is given by $\mathbf{z} = \mathbf{z}_0(\xi)$. Now we are wondering how would be the stable front solution in two dimensions. For small perturbations in the second dimension (y-axis), we can approximate the front solution as $\mathbf{z} \approx \mathbf{z}_0(\xi + \phi_0(y))$, where the function $\phi_0(y)$ shows a small spatial variation in y-axis. In general, we can write the two dimensional solution as $\mathbf{z}(x, y, t) = \mathbf{z}_0(\xi + \phi_0(y, t)) + \Delta\mathbf{z}$. Replacing this solution in Eq. (A.2) and expanding $\boldsymbol{F}(\mathbf{z})$ in a Taylor series near $\mathbf{z}_0$, neglecting terms of second order and higher, we obtain

$$\frac{\partial \mathbf{z}_0}{\partial t} + \frac{\partial \Delta\mathbf{z}}{\partial t} = \boldsymbol{F}(\mathbf{z}_0) + \boldsymbol{J}_F \Delta\mathbf{z} + \boldsymbol{D}\nabla^2 \mathbf{z}_0 + \boldsymbol{D}\nabla^2 \Delta\mathbf{z} + c\frac{\partial \mathbf{z}_0}{\partial \xi} + c\frac{\partial \Delta\mathbf{z}}{\partial \xi}. \tag{A.3}$$

Here $\boldsymbol{J}_F$ is the Jacobian of the vector function $\boldsymbol{F}(\mathbf{z})$. In addition, we define

$$\Delta \mathbf{z} = \sum_{i>0} \phi_i(y,t)\,\mathbf{u}_i(\xi) = \sum_{i>0} \phi_i \left|\mathbf{u}_i\right\rangle, \tag{A.4}$$

where the base chosen $\left|\mathbf{u}_i\right\rangle$ corresponds to the operator

$$\hat{\boldsymbol{L}} = \hat{\boldsymbol{J}}_{\boldsymbol{F}} + \boldsymbol{D}\frac{\partial^2}{\partial \hat{\xi}^2} + c\frac{\partial}{\partial \hat{\xi}}. \tag{A.5}$$

Consequently, $\hat{\boldsymbol{L}}\left|\mathbf{u}_i\right\rangle = \lambda_i \left|\mathbf{u}_i\right\rangle$. Using the notation $\left\langle \xi \,|\, \mathbf{u}_i \right\rangle = \mathbf{u}_i(\xi)$ and replacing the following identities:

$$\begin{aligned}
&\frac{\partial \mathbf{z}_0}{\partial t} = \frac{\partial \mathbf{z}_0}{\partial \hat{\xi}}\frac{\partial \phi_0}{\partial t} \\
&\frac{\partial \Delta \mathbf{z}}{\partial t} = \sum_{i>0} \frac{\partial \phi_i}{\partial t}\left|\mathbf{u}_i\right\rangle \\
&c\frac{\partial \Delta \mathbf{z}}{\partial \hat{\xi}} = c\sum_{i>0} \phi_i \frac{\partial}{\partial \hat{\xi}}\left|\mathbf{u}_i\right\rangle \\
&\boldsymbol{D}\nabla^2 \mathbf{z}_0 = \boldsymbol{D}\frac{\partial^2 \mathbf{z}_0}{\partial \hat{\xi}^2} + \boldsymbol{D}\frac{\partial^2 \mathbf{z}_0}{\partial \hat{\xi}^2}\left(\frac{\partial \phi_0}{\partial y}\right)^2 + \boldsymbol{D}\frac{\partial \mathbf{z}_0}{\partial \hat{\xi}}\frac{\partial^2 \phi_0}{\partial y^2} \\
&\boldsymbol{D}\nabla^2 \Delta \mathbf{z} = \boldsymbol{D}\sum_{i>0} \nabla^2\left(\left|\mathbf{u}_i\right\rangle \phi_i\right) = \boldsymbol{D}\sum_{i>0} \phi_i \frac{\partial^2}{\partial \hat{\xi}^2}\left|\mathbf{u}_i\right\rangle + \boldsymbol{D}\sum_{i>0}\left|\mathbf{u}_i\right\rangle \frac{\partial^2 \phi_i}{\partial y^2}
\end{aligned} \tag{A.6}$$

in Eq. (A.3), we obtain

$$\begin{aligned}
\frac{\partial \mathbf{z}_0}{\partial \hat{\xi}}\frac{\partial \phi_0}{\partial t} + \sum_{i>0} \frac{\partial \phi_i}{\partial t}\left|\mathbf{u}_i\right\rangle &= \hat{\boldsymbol{F}}(\mathbf{z}_0) + \sum_{i>0} \phi_i \hat{\boldsymbol{J}}_{\boldsymbol{F}}\left|\mathbf{u}_i\right\rangle + \boldsymbol{D}\frac{\partial^2 \mathbf{z}_0}{\partial \hat{\xi}^2} \\
&+ \boldsymbol{D}\frac{\partial^2 \mathbf{z}_0}{\partial \hat{\xi}^2}\left(\frac{\partial \phi_0}{\partial y}\right)^2 + \boldsymbol{D}\frac{\partial \mathbf{z}_0}{\partial \hat{\xi}}\frac{\partial^2 \phi_0}{\partial y^2} + \boldsymbol{D}\sum_{i>0} \phi_i \frac{\partial^2}{\partial \hat{\xi}^2}\left|\mathbf{u}_i\right\rangle \\
&+ \boldsymbol{D}\sum_{i>0}\left|\mathbf{u}_i\right\rangle \frac{\partial^2 \phi_i}{\partial y^2} + c\frac{\partial \mathbf{z}_0}{\partial \hat{\xi}} + c\sum_{i>0} \phi_i \frac{\partial}{\partial \hat{\xi}}\left|\mathbf{u}_i\right\rangle
\end{aligned} \tag{A.7}$$

On the other hand, we know that $\mathbf{z}_0(\xi)$ is solution of Eq. (A.2). With this substitution in Eq. (A.2) we obtain

$$0 = \hat{\boldsymbol{F}}(\mathbf{z}_0) + \boldsymbol{D}\frac{\partial^2 \mathbf{z}_0}{\partial \hat{\xi}^2} + c\frac{\partial \mathbf{z}_0}{\partial \hat{\xi}}. \tag{A.8}$$

Taking the derivative of Eq. (A.8) with respect to $\hat{\xi}$ we obtain

$$0 = \hat{\boldsymbol{J}}_{\boldsymbol{F}} \frac{\partial \mathbf{z}_0}{\partial \hat{\xi}} + \boldsymbol{D} \frac{\partial^3 \mathbf{z}_0}{\partial \hat{\xi}^3} + c \frac{\partial^2 \mathbf{z}_0}{\partial \hat{\xi}^2} = \hat{L} \left| \mathbf{u}_0 \right\rangle. \tag{A.9}$$

Where $\left| \mathbf{u}_0 \right\rangle = \partial \mathbf{z}_0 / \partial \hat{\xi}$ is the eigenvector whose eigenvalue is zero. Consequently, we obtain the following identity

$$\hat{\boldsymbol{F}}(\mathbf{z}_0) + \boldsymbol{D} \frac{\partial}{\partial \hat{\xi}} \left| \mathbf{u}_0 \right\rangle + c \left| \mathbf{u}_0 \right\rangle = 0. \tag{A.10}$$

The left term of Eq. (A.7) can be express using the Einstein summation convention as follows

$$\frac{\partial \mathbf{z}_0}{\partial \hat{\xi}} \frac{\partial \phi_0}{\partial t} + \sum_{i>0} \frac{\partial \phi_i}{\partial t} \left| \mathbf{u}_i \right\rangle = \left| \mathbf{u}_0 \right\rangle \frac{\partial \phi_0}{\partial t} + \sum_{i>0} \frac{\partial \phi_i}{\partial t} \left| \mathbf{u}_i \right\rangle = \frac{\partial \phi_i}{\partial t} \left| \mathbf{u}_i \right\rangle. \tag{A.11}$$

Replacing Eq. (A.10) and Eq. (A.11) in Eq. (A.7) we obtain

$$\frac{\partial \phi_i}{\partial t} \left| \mathbf{u}_i \right\rangle = \lambda_i \phi_i \left| \mathbf{u}_i \right\rangle + \left(\frac{\partial \phi_0}{\partial y} \right)^2 \boldsymbol{D} \frac{\partial}{\partial \hat{\xi}} \left| \mathbf{u}_0 \right\rangle + \frac{\partial^2 \phi_i}{\partial y^2} \boldsymbol{D} \left| \mathbf{u}_i \right\rangle. \tag{A.12}$$

Multiplying by $\left\langle \mathbf{u}_i \right|$, we have

$$\frac{\partial \phi_i}{\partial t} = \lambda_i \phi_i + \left\langle \mathbf{u}_i \right| \boldsymbol{D} \frac{\partial}{\partial \hat{\xi}} \left| \mathbf{u}_0 \right\rangle \left(\frac{\partial \phi_0}{\partial y} \right)^2 + \left\langle \mathbf{u}_i \right| \boldsymbol{D} \left| \mathbf{u}_j \right\rangle \frac{\partial^2 \phi_j}{\partial y^2}. \tag{A.13}$$

We assume that near the instability $\mathrm{Re}(\lambda_i) < 0$. We also assume that ϕ_i are small compare with ϕ_0, and for a large time we assume that $\partial \phi_i / \partial t \to 0$ for $i > 0$. With these assumptions we can carry out the elimination of the slave modes [111]. We obtain the following approximation from Eq. (A.13)

$$\phi_i \approx - \frac{\left\langle \mathbf{u}_i \right| \boldsymbol{D} \frac{\partial}{\partial \hat{\xi}} \left| \mathbf{u}_0 \right\rangle \left(\frac{\partial \phi_0}{\partial y} \right)^2 + \left\langle \mathbf{u}_i \right| \boldsymbol{D} \left| \mathbf{u}_0 \right\rangle \frac{\partial^2 \phi_0}{\partial y^2}}{\lambda_i}, \text{ for } i > 0. \tag{A.14}$$

But in the numerator of Eq. (A.14), the first term is smaller compared with the second term; therefore this equation can be reduced to

$$\phi_i \approx -\frac{\langle \mathbf{u}_i | \boldsymbol{D} | \mathbf{u}_0 \rangle \frac{\partial^2 \phi_0}{\partial y^2}}{\lambda_i}, \text{ for } i > 0. \tag{A.15}$$

We also obtain an equation for ϕ_0 from Eq. (A.13)

$$\frac{\partial \phi_0}{\partial t} = \langle \mathbf{u}_0 | \boldsymbol{D} \frac{\partial}{\partial \xi} | \mathbf{u}_0 \rangle \left(\frac{\partial \phi_0}{\partial y} \right)^2 + \langle \mathbf{u}_0 | \boldsymbol{D} | \mathbf{u}_j \rangle \frac{\partial^2 \phi_j}{\partial y^2}. \tag{A.16}$$

The last term in Eq. (A.16) can be expressed as follows

$$\langle \mathbf{u}_0 | \boldsymbol{D} | \mathbf{u}_j \rangle \frac{\partial^2 \phi_j}{\partial y^2} = \langle \mathbf{u}_0 | \boldsymbol{D} | \mathbf{u}_0 \rangle \frac{\partial^2 \phi_0}{\partial y^2} - \sum_{j>0} \frac{\langle \mathbf{u}_0 | \boldsymbol{D} | \mathbf{u}_j \rangle \langle \mathbf{u}_j | \boldsymbol{D} | \mathbf{u}_0 \rangle}{\lambda_j} \frac{\partial^4 \phi_0}{\partial y^4}. \tag{A.17}$$

With this substitution Eq. (A.16) becomes

$$\frac{\partial \phi_0}{\partial t} = \langle \mathbf{u}_0 | \boldsymbol{D} \frac{\partial}{\partial \hat{\xi}} | \mathbf{u}_0 \rangle \left(\frac{\partial \phi_0}{\partial y} \right)^2 + \nu \frac{\partial^2 \phi_0}{\partial y^2} - \kappa \frac{\partial^4 \phi_0}{\partial y^4}. \tag{A.18}$$

Where

$$\nu = \langle \mathbf{u}_0 | \boldsymbol{D} | \mathbf{u}_0 \rangle \tag{A.19}$$

and

$$\kappa = \sum_{j>0} \frac{\langle \mathbf{u}_0 | \boldsymbol{D} | \mathbf{u}_j \rangle \langle \mathbf{u}_j | \boldsymbol{D} | \mathbf{u}_0 \rangle}{\lambda_j}. \tag{A.20}$$

Now we are going to find the coefficient of the term $(\partial \phi_0 / \partial y)^2$ in Eq. (A.18). The null eigenvectors $\langle \mathbf{u}_0 |$ and $| \mathbf{u}_0 \rangle$ satisfy [112]:

$$\hat{\boldsymbol{J}}_{\boldsymbol{F}} | \mathbf{u}_0 \rangle + \frac{\partial^2}{\partial \hat{\xi}^2} \boldsymbol{D} | \mathbf{u}_0 \rangle + c \frac{\partial}{\partial \hat{\xi}} | \mathbf{u}_0 \rangle = 0 \tag{A.21}$$

and

$$\langle \mathbf{u}_0 | \hat{\boldsymbol{J}}_{\boldsymbol{F}} + \frac{\partial^2}{\partial \hat{\xi}^2} \langle \mathbf{u}_0 | \boldsymbol{D} - c \frac{\partial}{\partial \hat{\xi}} \langle \mathbf{u}_0 | = 0. \tag{A.22}$$

Multiplying Eq. (A.21) from the left with $\langle \mathbf{u}_0 |$ and Eq. (A.22) from the right with $|\mathbf{u}_0\rangle$, and subtracting the resulting equations, we obtain

$$\left(\frac{\partial^2}{\partial \hat{\xi}^2}\langle \mathbf{u}_0|\boldsymbol{D}|\mathbf{u}_0\rangle - \langle \mathbf{u}_0|\boldsymbol{D}\frac{\partial^2}{\partial \hat{\xi}^2}|\mathbf{u}_0\rangle\right) - c\left(\frac{\partial}{\partial \hat{\xi}}\langle \mathbf{u}_0|\mathbf{u}_0\rangle + \langle \mathbf{u}_0|\frac{\partial}{\partial \hat{\xi}}|\mathbf{u}_0\rangle\right) = 0. \quad \text{(A.23)}$$

The above equation can be written as

$$\frac{\partial}{\partial \hat{\xi}}\left\{\left(\frac{\partial}{\partial \hat{\xi}}\langle \mathbf{u}_0|\boldsymbol{D}|\mathbf{u}_0\rangle - \langle \mathbf{u}_0|\boldsymbol{D}\frac{\partial}{\partial \hat{\xi}}|\mathbf{u}_0\rangle\right) - c\langle \mathbf{u}_0|\mathbf{u}_0\rangle\right\} = 0. \quad \text{(A.24)}$$

Integrating Eq. (A.24) two times, we obtain

$$c = \int_{-\infty}^{\infty}\left(\frac{\partial}{\partial \hat{\xi}}\langle \mathbf{u}_0|\boldsymbol{D}|\mathbf{u}_0\rangle - \langle \mathbf{u}_0|\boldsymbol{D}\frac{\partial}{\partial \hat{\xi}}|\mathbf{u}_0\rangle\right)d\hat{\xi}. \quad \text{(A.25)}$$

Using the fact that

$$\frac{\partial}{\partial \hat{\xi}}\langle \mathbf{u}_0|\boldsymbol{D}|\mathbf{u}_0\rangle = \left(\frac{\partial}{\partial \hat{\xi}}\langle \mathbf{u}_0|\right)\boldsymbol{D}|\mathbf{u}_0\rangle + \langle \mathbf{u}_0|\boldsymbol{D}\frac{\partial}{\partial \hat{\xi}}|\mathbf{u}_0\rangle, \quad \text{(A.26)}$$

and using partial integration, Eq. (A.25) becomes

$$c = -2\int_{-\infty}^{\infty}\left(\langle \mathbf{u}_0|\boldsymbol{D}\frac{\partial}{\partial \hat{\xi}}|\mathbf{u}_0\rangle u_0\right)d\hat{\xi} = -2\langle \mathbf{u}_0|\boldsymbol{D}\frac{\partial}{\partial \hat{\xi}}|\mathbf{u}_0\rangle. \quad \text{(A.27)}$$

Thus

$$\langle \mathbf{u}_0|\boldsymbol{D}\frac{\partial}{\partial \hat{\xi}}|\mathbf{u}_0\rangle = -\frac{c}{2}. \quad \text{(A.28)}$$

With this substitution Eq. (A.18) becomes

$$\frac{\partial \phi_0}{\partial t} = -\frac{c}{2}\left(\frac{\partial \phi_0}{\partial y}\right)^2 + \nu\frac{\partial^2 \phi_0}{\partial y^2} - \kappa\frac{\partial^4 \phi_0}{\partial y^4}, \quad \text{(A.29)}$$

which is the KS equation.

A.2 Linear stability analysis and the eigenvalue equation

In the following we will present the derivation of the linear set of eigenvalue equations used to determine the stability of the fronts. We obtained Eq. (5.10) that involves only the front height h, and its Fourier coefficients H_n

$$\frac{\partial h}{\partial t} = -\frac{\partial^2 h}{\partial x^2} + \frac{1}{2}\left(\frac{\partial h}{\partial x}\right)^2 - \frac{\partial^4 h}{\partial x^4} + \frac{\mathrm{Ra}}{2}\sum_n \left(\frac{n\pi}{\mathrm{L}}\right) H_n \cos\left(\frac{n\pi x}{\mathrm{L}}\right). \tag{A.30}$$

We introduce in this equation the solution $h(x)$ with the addition of a perturbation $H'(x,t)$, and the equation becomes

$$\frac{\partial H'}{\partial t} = -\frac{\partial^2 H'}{\partial x^2} - \frac{\partial^4 H'}{\partial x^4} + \left(\frac{\partial h}{\partial x}\right)\left(\frac{\partial H'}{\partial x}\right) + \frac{1}{2}\left(\frac{\partial H'}{\partial x}\right)^2 + \frac{\mathrm{Ra}}{2}\sum_n \left(\frac{n\pi}{\mathrm{L}}\right) H'_n \cos\left(\frac{n\pi x}{\mathrm{L}}\right). \tag{A.31}$$

Keeping only linear terms the equation becomes

$$\frac{\partial H'}{\partial t} = -\frac{\partial^2 H'}{\partial x^2} - \frac{\partial^4 H'}{\partial x^4} + \left(\frac{\partial h}{\partial x}\right)\left(\frac{\partial H'}{\partial x}\right) + \frac{\mathrm{Ra}}{2}\sum_n \left(\frac{n\pi}{\mathrm{L}}\right) H'_n \cos\left(\frac{n\pi x}{\mathrm{L}}\right). \tag{A.32}$$

We consider solutions of the form

$$H'(x,t) = e^{\sigma t}\tilde{H}(x), \tag{A.33}$$

where σ is the growth rate of the perturbation. With this substitution, Eq. (A.32) becomes an eigenvalue equation, with σ the eigenvalue and $\tilde{H}$ the eigenfunction

$$\sigma\tilde{H} = -\frac{\partial^2 \tilde{H}}{\partial x^2} - \frac{\partial^4 \tilde{H}}{\partial x^4} + \left(\frac{\partial h}{\partial x}\right)\left(\frac{\partial \tilde{H}}{\partial x}\right) + \frac{\mathrm{Ra}}{2}\sum_n \left(\frac{n\pi}{\mathrm{L}}\right) \tilde{H}_n \cos\left(\frac{n\pi x}{\mathrm{L}}\right). \tag{A.34}$$

We introduce the Fourier series on $h(x)$ and $\tilde{H}(x)$:

$$h = \sum_n h_n \cos(nqx) \tag{A.35}$$

and

$$\tilde{H} = \sum_m \tilde{H}_m \cos(mqx) \tag{A.36}$$

where $q = \pi / L$. With this substitution Eq. (A.34) becomes

$$\begin{aligned} \sigma \sum_m \tilde{H}_m \cos(mqx) = & \sum_m (mq)^2 \tilde{H}_m \cos(mqx) - \sum_m (mq)^4 \tilde{H}_m \cos(mqx) \\ & + \sum_n \sum_m (nq)(mq) h_n \tilde{H}_m \sin(nqx) \sin(mqx) \\ & + \frac{\mathrm{Ra}}{2} \sum_m (mq) \tilde{H}_m \cos(mqx), \end{aligned} \tag{A.37}$$

and projecting over the corresponding cosine function, we have

$$\begin{aligned} \sigma \sum_m \tilde{H}_m \int_0^L \cos(mqx) \cos(pqx)\, dx = & \\ & \sum_m (mq)^2 \tilde{H}_m \int_0^L \cos(mqx) \cos(pqx)\, dx \\ & - \sum_m (mq)^4 \tilde{H}_m \int_0^L \cos(mqx) \cos(pqx)\, dx \\ & + \sum_n \sum_m (nq)(mq) h_n \tilde{H}_m \int_0^L \sin(nqx) \sin(mqx) \cos(pqx)\, dx. \end{aligned} \tag{A.38}$$

Using the following product to sum formula

$$\sin(nqx) \sin(mqx) = \frac{1}{2} \{ \cos[(n-m)qx] - \cos[(n+m)qx] \}, \tag{A.39}$$

and taking into account that the integrals are nonzero only when $m = p$, we obtain

$$\sigma \tilde{H}_p = (pq)^2 \tilde{H}_p - (pq)^4 \tilde{H}_p + \frac{q^2}{2} \sum_m \sum_n (n)(m) h_n \tilde{H}_m \left(\delta_{|n-m|,p} - \delta_{n+m,p} \right) \text{ for } p \geq 1 \tag{A.40}$$

This linear set of eigenvalue equations on the coefficients $\tilde{H}_p$ can be written in compact form as

$$\sigma \tilde{H}_p = (pq)^2 \tilde{H}_p - (pq)^4 \tilde{H}_p + \sum_m A_{pm} \tilde{H}_m \quad \text{for} \quad p \geq 1, \tag{A.41}$$

where

$$A_{pm} = \sum_n \frac{q^2}{2}(n)(m) B_n \left(\delta_{|n-m|,p} - \delta_{n+m,p} \right). \qquad \text{(A.42)}$$

References

[1] R. J. Field and M. Burger, Eds., *Oscillations and Traveling Waves in Chemical Systems*. New York: Wiley, 1985.

[2] I. R. Epstein and K. Showalter, "Nonlinear Chemical Dynamics: Oscillations, Patterns, and Chaos," *J. Phys. Chem.*, vol. 100, pp. 13132-13147, 1996.

[3] A. T. Winfree, "Spiral Waves of Chemical Activity," *Science*, vol. 175, pp. 634-636, 1972.

[4] B. P. Belousov, "A periodic reaction and its mechanism," in *Oscillations and Travelling Waves in Chemical Systems*, R. J. Field and M. Burger, Eds. New York: Wiley, 1985, pp. 605-614.

[5] P. De Kepper, I. R. Epstein, K. Kustin, and M. Orbán, "Batch oscillations and spatial wave patterns in chlorite oscillating systems," *J. Phys. Chem.*, vol. 86, pp. 170-171, 1982.

[6] A. Hanna, A. Saul, and K. Showalter, "Detailed Studies of Propagating Fronts in the Iodate Oxidation of Arsenous Acid ," *J. Am. Chem. Soc.*, vol. 104, pp. 3838-3844, 1982.

[7] Jakob Löber and Harald Engel, "Controlling the Position of Traveling Waves in Reaction-Diffusion Systems," *Phys. Rev. Lett.*, vol. 112, no. 14, p. 148305, 2014.

[8] J. P. Keener and J. J. Tyson, "Spiral waves in the Belousov-Zhabotinskii reaction," *Physical D*, vol. 21, pp. 307-324, 1986.

[9] P Dähmlow, V. K. Vanag, and S. C. Müller, "Effect of solvents on the pattern formation in a Belousov-Zhabotinsky reaction embedded into a microemulsion," *Phys. Rev. E*, vol. 89, no. 1, p. 010902, 2014.

[10] M. A. Budroni, F. Wodlei, and M. Rustici, "Butterfly effect in a chemical

oscillator," *European Journal of Physics*, vol. 35, no. 4, p. 045005, 2014.

[11] I. Lengyel and I. R. Epstein, "Modeling of Turing Structures in the Chlorite—Iodide—Malonic Acid—Starch Reaction System," *Science*, vol. 251, no. 49994, pp. 650-652, 1991.

[12] V. Castets, E. Dulos, J. Boissonade, and P. De Kepper, "Experimental evidence of a sustained standing Turing-type nonequilibrium chemical pattern," *Phys. Rev. Lett.*, vol. 64, p. 2953, 1990.

[13] C. E. Dateo, M. Orbán, P. De Kepper, and I. R. Epstein, "Bistability and Oscillations in the Autocatalytic Chlorite-Iodide Reaction in a Stirred-Flow Reactor," *J. Am. Chem. Soc.*, vol. 104, pp. 504-509, 1982.

[14] D. M. Weitz and I. R. Epstein, "Spatial waves in the reaction of chlorite with iodide," *J. Phys. Chem.*, vol. 88, pp. 5300–5304, 1984.

[15] Peter Ortoleva and John Ross, "Theory of propagation of discontinuities in kinetic systems with multiple time scales: Fronts, front multiplicity, and pulses," *J. Chem. Phys.*, vol. 63, p. 3398, 1975.

[16] V. Méndez and J. E. Llebot, "Hyperbolic reaction-diffusion equations for a forest fire model," *Phys. Rev. E*, vol. 56, pp. 6557-6563, 1997.

[17] M. N. Kuperman and H. S. Wio H. S., "Front propagation in epidemiological models with spatial dependence," *Physica A*, vol. 272, p. 206, 1999.

[18] L. Balázs, "Corrosion front roughening in two-dimensional pitting of aluminum thin layers," *Phys. Rev. E*, vol. 54, pp. 1183-1189, 1996.

[19] A. Saul and K. Showalter, "Propagating Reaction-Diffusion Fronts," in *Oscillations and Traveling Waves in Chemical Systems*, R. J. Field and M. Burger, Eds. New York: Wiley-Interscience, 1985, ch. XI, pp. 419-439.

[20] R. A. Fisher, "The wave of advance of advantageous genes," *Ann.*

Eugenics, vol. 7, pp. 353–369, 1937.

[21] A. N. Kolmogorov, I. G. Petrovsky, and N. S. Piskounov, "Study of the diffusion equation with growth of the quantity of matter and its application to a biology problem," *Bulletin de l'université d'état à Moscou*, vol. 1, pp. 1-25, 1937.

[22] S. K. Scott and K. Showalter, "Simple and complex propagating reaction-diffusion fronts," *J. Phys. Chem.*, vol. 96, pp. 8702-8711, 1992.

[23] D. Horváth, V. Petrov, S. K. Scott, and K. Showalter, "Instabilities in Propagating Reaction-Diffusion Fronts," *J. Chem. Phys.*, vol. 98, pp. 6332-6343, 1993.

[24] D. Horváth and K. Showalter, "Instabilities in Propagating Reaction-Diffusion Fronts of the Iodate-Arsenous Acid Reaction," *J. Chem. Phys.*, vol. 102, pp. 2471-2478, 1995.

[25] J. J. Tyson and J. P. Keener, "Singular Perturbation Theory of Spiral Waves in Excitable Media," *Physica D* , vol. 32, pp. 327-361, 1988.

[26] Y. Kuramoto and T. Tsuzuki, "Persistent Propagation of Concentration Waves in Dissipative Media Far from Thermal Equilibrium," *Prog. Theor. Phys.*, vol. 55, pp. 356-369, 1976.

[27] G. I. Sivashinsky, "Diffusional-thermal theory of cellular flames," *Combust. Sci. Technol.*, vol. 15, pp. 137-146, 1977.

[28] P. Foerster, S. C. Muller, and B. and Hess, "Curvature and Propagation Velocity of Chemical Waves," *Science*, vol. 241, no. 4866, pp. 685-687 , 1988.

[29] A. Malevanets, A. Careta, and R. Kapral, "Biscale chaos in propagating fronts," *Phys. Rev. E*, vol. 52, pp. 4724–4735, 1995.

[30] Y. Kuramoto, *Chemical Oscillations, Waves, and Turbulence*. Berlin:

Springer, 1984.

[31] K. Kassler, A. K. Hobbs, and P. Metzener, "Dynamical patterns in directional solidification," *Physica D*, vol. 93, pp. 23-51, 1996.

[32] B. I. Shraiman, "Order, Disorder, and Phase Turbulence," *Phys. Rev. Lett.*, vol. 57, pp. 325-328, 1986.

[33] G. I. Sivashinsky and D. M. Michelson, "On Irregular Wavy Flow of a Liquid Film Down a Vertical Plane," *Prog. Theor. Phys.*, vol. 63, pp. 2112-2114, 1980.

[34] T. Shlang and G. I. Sivashinsky, "Irregular flow of a liquid film down a vertical column," *J. Phys. France*, vol. 43, pp. 459 - 466, 1982.

[35] I. G. Kevrekidis, B. Nicolaenko, and C. Scovel, "Back in the saddle again: a computer assisted study of the Kuramoto–Sivashinsky equation," *SIAM J. Appl. Maths.*, vol. 50, pp. 760–790, 1990.

[36] C. R. Nugent, W. M. Quarles, and T. H. Solomon, "Experimental Studies of Pattern Formation in a Reaction-Advection-Diffusion System," *Phys. Rev. Lett.*, vol. 93, p. 218301, 2004.

[37] M. S. Paoletti and T. H. Solomon, "Front propagation and mode-locking in an advection-reaction-diffusion system," *Phys. Rev. E*, vol. 72, p. 046204, 2005.

[38] J. A. Pojman, I. R. Epstein, T. J. McManus, and K. Showalter, "Convective Effects on Chemical Waves. 2. Simple Convection in the Iodate-Arsenous Acid System," *J. Phys. Chem.*, vol. 95, pp. 1299-1306, 1991.

[39] H. J. Kull, "Theory of the Rayleigh-Taylor instability," *Phys. Rep.*, vol. 206, pp. 197–325, 1991.

[40] B. F. Edwards, J. W. Wilder, and K. Showalter, "Onset of convection for autocatalytic reaction fronts: Laterally unbounded system," *Phys. Rev. A*,

vol. 43, pp. 749-760, 1991.

[41] Jie Huang, Desiderio A. Vasquez, and Boyd F. Edwards, "Onset of convection for autocatalytic reaction fronts in a vertical slab," *Phys. Rev. E*, vol. 48, no. 6, pp. 4378-4386, 1993.

[42] D. A. Vasquez, J. W. Wilder, and B. F. Edwards, "Convective instability of autocatalytic reaction fronts in vertical cylinders," *Phys. Fluids A*, vol. 4, pp. 2410-2414, 1992.

[43] D. A. Vasquez, J. W. Wilder, and B. F. Edwards, "Hydrodynamic instability of chemical waves," *J. Chem. Phys.*, vol. 98, pp. 2138-2143, 1993.

[44] A. Komlósi, I. P. Nagy, G. Bazsa, and J. A. Pojman, "Convective Chemical Fronts in the 1,4-Cyclohexanedione-Bromate-Sulfuric Acid-Ferroin System," *J. Phys. Chem. A*, vol. 102, pp. 9136-9141, 1998.

[45] A. Keresztessy, I. P. Nagy, G. Bazsa, and J. A. Pojman, "Traveling Waves in the Iodate-Sulfite and Bromate-Sulfite Systems," *J. Phys. Chem.*, vol. 99, pp. 5379-5384, 1995.

[46] J. Masere, D. A. Vasquez, B. F. Edwards, J. W. Wilder, and K. Showalter, "Nonaxisymmetric and Axisymmetric Convection in Propagating Reaction-Diffusion Fronts," *J. Phys. Chem.*, vol. 98, pp. 6505-6508, 1994.

[47] R. S. Spangler and B. F. Edwards, "Poiseuille Advection of Chemical Reaction Fronts: Eikonal Approximation," *J. Chem. Phys.*, vol. 118, pp. 5911-5915, 2003.

[48] B. F. Edwards, "Poiseuille Advection of Chemical Reaction Fronts," *Phys. Rev. Lett.*, vol. 89, p. 104501, 2002.

[49] M. Leconte, J. Martin, N. Rakotomalala, and D. Salin, "Pattern of Reaction Diffusion Fronts in Laminar Flows," *Phys. Rev. Lett.*, vol. 90, p. 128302, 2003.

[50] J. Martin, N. Rakotomalala, D. Salin, and M. Böckmann, "Buoyancy-driven instability of an autocatalytic reaction front in a Hele-Shaw cell," *Phys. Rev. E*, vol. 65, p. 051605, 2002.

[51] J. D'Hernoncourt, J. H. Merkin, and A. De Wit, "Interaction between buoyancy and diffusion-driven instabilities of propagating autocatalytic reaction fronts. I. Linear stability analysis," *J. Chem. Phys.*, vol. 130, p. 114502, 2009.

[52] J. D'Hernoncourt, J. H. Merkin, and A. De Wit, "Interaction between buoyancy and diffusion-driven instabilities of propagating autocatalytic reaction fronts. II. Nonlinear simulations," *J. Chem. Phys.*, vol. 130, p. 114503, 2009.

[53] D. Elliott and D. A. Vasquez, "Convection in stable and unstable fronts," *Phys. Rev. E*, vol. 85, p. 016207, 2012.

[54] S. K. Scott, *Oscillations, Waves, and Chaos in Chemical Kinetics*. New York: Oxford University Press, Incorporated, 1994.

[55] B. R. Johnson and S. K. Scott, "New approaches to chemical patterns," *Chem. Soc. Rev.*, vol. 25, pp. 265-273, 1996.

[56] D. A. Vasquez, J. Meyer, and H. Suedhoff, "Chemical pattern formation induced by a shear flow in a two-layer model," *Phys. Rev. E*, vol. 78, p. 036109, 2008.

[57] A. B. Rovinsky and M. Menzinger, "Chemical instability induced by a differential flow," *Phys. Rev. Lett.*, vol. 69, p. 1193, 1992.

[58] M. Böckmann and S. C. Müller, "Growth Rates of the Buoyancy-Driven Instability of an Autocatalytic Reaction Front in a Narrow Cell," *Phys. Rev. Lett.*, vol. 85, pp. 2506-2509, 2000.

[59] L. Stucchi and D. A. Vasquez, "Pattern formation induced by a differential shear flow," *Phys. Rev. E* , vol. 87, no. 2, 2013.

[60] S. H. Park, S. Parus, R. Kopelman, and H. Taitelbaum, "Gel-free experiments of reaction-diffusion front kinetics," *Phys. Rev. E 64*, vol. 64, p. 055102(R), S. H. Park, S. Parus, R. Kopelman, and H. Taitelbaum 2001.

[61] Edward Ott, *Chaos in Dynamical Systems*, 2nd ed. New York, USA: Cambridge University Press, 2002.

[62] S. H. Strogatz, *Nonlinear Dynamics and Chaos*. Cambridge: Westview Press, 1994.

[63] Michael Cross and Henry Greenside, *Pattern Formation and Dynamics in Nonequilibrium Systems*. New York, USA: Cambridge University Press, 2009.

[64] George B. Arfken and Hans J. Weber, *Mathematical Methods for Physicists*, 6th ed. San Diego, USA: Elsevier Academic Press, 2005.

[65] E. Bodenschatz, W. Pesch, and G. Ahlers, "Recent Developments in Rayleigh-Bénard Convection," *Ann. Rev. Fluid Mech.*, vol. 32, pp. 709-778, 2000.

[66] C. D. Andereck, S. S. Liu, and H. L. Swinney, "Flow regimes in a circular Couette system with independently rotating cylinders," *J. Fluid Mech.*, vol. 164, pp. 155-183, 1986.

[67] Philip S. Marcus, "Simulation of Taylor-Couette flow. Part 1. Numerical methods and comparison with experiment," *Journal of Fluid Mechanics*, vol. 146, pp. 45-64 , 1984.

[68] L. D. Landau and E. M. Lifshitz, *Course of Theoretical Physics: Fluid Mechanics*, Pergamon, Ed. New York, 1987.

[69] J. Huang and B. F. Edwards, "Pattern formation and evolution near autocatalytic reaction fronts in a narrow vertical slab," *Phys. Rev. E*, vol. 54, pp. 2620-2627, 1996.

[70] M. Fermigier, L. Limat, J. E. Wesfreid, P. Boudinet, and C. Quilliet, "Two-dimensional patterns in Rayleigh-Taylor instability of a thin layer," *J. Fluid Mech.*, vol. 236, pp. 349-383, 1992.

[71] S. Chandrasekhar, *Hydrodynamic and Hydromagnetic Stability*.: Dover Publications, Inc. , 1981.

[72] Hans Dierckx, Olivier Bernus, and Henri Verschelde, "Accurate Eikonal-Curvature Relation for Wave Fronts in Locally Anisotropic Reaction-Diffusion Systems," *Phys. Rev. Lett.*, vol. 107, p. 108101, 2011.

[73] G. I. Sivashinsky, "Nonlinear analysis of hydrodynamic instability in laminar flames—I. Derivation of basic equations," *Acta Astronaut.*, vol. 4, pp. 1177–1206, 1977.

[74] E. L. Cussler, *Diffusion Mass Transfer in Fluid Systems*, 3rd ed. Cambridge: Cambridge Univ. Press, 1984.

[75] J Crank, *The mathematics of diffusion*, 2nd ed. New York: Clarendon press Oxford, 1975.

[76] H. Mehrer, *Diffusion in solids: fundamentals, methods, materials, diffusion-controlled processes*, 2nd ed.: Springer, 2007.

[77] W. van Saarloos, "Front propagation into unstable states," *Phys. Report*, vol. 386, pp. 29–222, 2003.

[78] J. Ross, S. C. Müller, and C. Vidal, "Chemical waves," *Science*, vol. 240, p. 460, 1988.

[79] D. Horváth et al., "Convective dynamics of traveling autocatalytic fronts in a modulated gravity field," *Phys. Chem. Chem. Phys.*, vol. 16, pp. 26279-26287, 2014.

[80] P. Gray and S. K. Scott, "Sustained Oscillations and Other Exotic Patterns of Behavior in Isothermal Reactions," *J. Phys. Chem.*, vol. 89, pp. 22-32,

1985.

[81] K. Showalter, "Chemical waves," in *Kinetics of Nonhomogenenous Processes: A Practical Introduction for Chemists, Biologists, Physicists and Materials Scientists*, Gordon R. Freeman, Ed. New York: John Wiley and Sons, 1987, pp. 769–821.

[82] G. Schmitz, "Kinetics and mechanism of the iodate–iodide reaction and other related reactions," *Phys. Chem. Chem. Phys.*, vol. 1, pp. 1909-1914, 1999.

[83] P. De Kepper, I. R. Epstein, and K. Kustin, "Bistability in the Oxidation of Arsenite by Iodate in a Stirred Flow Reactor," *J. A. Chem. Soc.*, vol. 103, pp. 6121-6127, 1981.

[84] J. Maselko and K. Showalter, "Chemical waves on spherical surfaces," *Nature*, vol. 339, pp. 609-611, 1989.

[85] S. B. Margolis and G. I. Sivashinsky, "Flame Propagation in Vertical Channels: Bifurcation to Bimodal Cellular Flames," *SIAM J. Appl. Math.*, vol. 44, pp. 344–368, 1984.

[86] D. T. Papageorgiou and Y. S. Smyrlis, "The route to chaos for the Kuramoto-Sivashinsky equation," *Theoretical and Computational Fluid Dynamics*, vol. 3, pp. 15-42, 1991.

[87] G. I. Sivashinsky, "Instabilities, Pattern Formation, and Turbulence in Flames," *Annu. Rev. Fluid Mech.*, vol. 15, pp. 179-199, 1983.

[88] J. M. Hyman and B. Nicolaenko, "The Kuramoto-Sivashinsky equation: A bridge between PDE's and dynamical systems," *Phys. D*, vol. 18, pp. 113-126, 1986.

[89] W. Press, B. Flannery, S. Teukolsky, and W. Vetterling, *Numerical Recipes*. Cambridge: Cambridge University Press, 1986.

[90] K. F. Riley, M. P. Hobson, and S. J. Bence, *Mathematical Methods for Physics and Engineering*, Thrid ed. Cambridge: Cambridge University Press, 2006.

[91] J. N. Elgin and X. Wu, "Stability of cellular states of the Kuramoto-Sivashinsky equation," *SIAM J. Appl. Math.*, vol. 56, pp. 1621-1638, 1996.

[92] P. Cvitanović, R. Davidchack, and E. Siminos, "On the state space geometry of the Kuramoto-Sivashinsky flow in a periodic domain," *SIAM J. Appl. Dyn. Syst.*, vol. 9, pp. 1-33, 2010.

[93] P. Brunet, "Stabilized Kuramoto-Sivashinsky equation: A useful model for secondary instabilities and related dynamics of experimental one-dimensional cellular flows," *Phys. Rev. E*, vol. 76, p. 017204, 2007.

[94] J. W. Wilder, D. A. Vasquez, and B. F. Edwards, "Modification of the eikonal relation for chemical waves to include fiuid fiow," *Phys. Rev. E*, vol. 47, pp. 3761-3764, 1993.

[95] L. Gyorgyi and R. J. Field, "Simple models of deterministic chaos in the Belousov-Zhabotinsky reaction," *J. Phys. Chem.*, vol. 95, pp. 6594–6602, 1991.

[96] K. Bar-Eli and M. Broens, "Period lengthening near the end of oscillations in chemical systems," *J. Phys. Chem.*, vol. 94, pp. 7170–7177, 1990.

[97] O. Miholics, T. Rica, D. Horváth, and Á. Tóth, "Oscillatory and stationary convective patterns in a reaction driven gravity current," *J. Chem. Phys.*, vol. 135, p. 204501, 2011.

[98] I. Nagypál and I. R. Epstein, "Fluctuatlons and Stirring Rate Effects In the Chlorlte-Thiosulfate Reaction," *J. Phys. Chem.*, vol. 90, pp. 6285-6292 , 1986.

[99] Erwin Kreyszig, *advanced engineering mathematics*, 9th ed. Singapure: John Wiley & Sons, Inc., 2006.

[100] J. Elezgaray and A. Arneodo, "Modeling reaction-diffusion pattern formation in the Couette flow reactor," *J. Chem. Phys.* , vol. 95, p. 323, 1991.

[101] F. Daviaud, J. Hegseth, and P Bergé, "Subcritical transition to turbulence in plane Couette flow," *Phys. Rev. Lett.*, vol. 69, pp. 2511-2514, 1992.

[102] Th. Buzug, J. von Stamm, and G. Pfister, "Characterization of period-doubling scenarios in Taylor-Couette flow," *Phys. Rev. E*, vol. 47, pp. 1054-1065, 1993.

[103] J. A. Pojman, I. P. Nagy, and I. R. Epstein, "Convective effects on chemical waves. 3. Multicomponent convection in the iron(II)-nitric acid system," *J. Phys. Chem.*, vol. 95, pp. 1306-1311, 1991.

[104] T., Jr. Bánsági, D. Horváth, and A. Tóth, "Convective instability of an acidity front in Hele-Shaw cells," *Phys. Rev. E 68, 026303 (2003).*, vol. 68, p. 026303, 2003.

[105] D. A. Vasquez and A. De Wit, "Dispersion relations for the convective instability of an acidity front in Hele-Shaw cells," *J. Chem. Phys.*, vol. 121, p. 935, 2004.

[106] Y. S. Smyrlis and D. T. Papageorgiou, "Predicting chaos for infinite dimensional dynamical systems: the Kuramoto-Sivashinsky equation, a case study," *Proc. Nat. Acad. Sci. USA*, vol. 88, pp. 11129-11132, 1991.

[107] P. G. Saffman and G. I. Taylor, "The Penetration of a Fluid into a Porous Medium or Hele-Shaw Cell Containing a More Viscous Liquid," *Proc. R. Soc. London, Ser. A*, vol. 245, pp. 312-329, 1958.

[108] B. T. Smith et al., *Matrix Eigensystem Routines: EISPACK Guide*, 2nd ed. Berlin: Springer-Verlag, 1976.

[109] Jan-Otto Carlsson and Peter M. Martin, "Chemical Vapor Deposition," in *Handbook of Deposition Technologies for Films and Coatings*, Peter M.

Martin, Ed. Oxford , UK: Elsevier Inc., 2010, ch. 7, pp. 314-363.

[110] C. Clanet and G. Searby, "First Experimental Study of the Darrieus-Landau Instability," *Phys. Rev. Lett.*, vol. 80, p. 3867, 1998.

[111] P. Manneville, *Dissipative structures and weak turbulence*. Boston: Academic Press, 1990.

[112] Y. Kuramoto, "Instability and Turbulence of Wavefronts in Reaction-Diffusion Systems ," *Prog. Theor. Phys.*, vol. 63, pp. 1885-1903, 1980.